Institut für Technische Chemie II der Technischen Universität München

# New heterogeneous catalysts for hydroamination reactions

Jochen Penzien

Vollständiger Abdruck der von der Fakultät für Chemie der Technischen Universität München zur Erlangung des akademischen Grades eines

**Doktors der Naturwissenschaften**

genehmigten Dissertation.

Vorsitzender: Univ. – Prof. (Komm.) Dr. Walther Nitsch, em.

Prüfer der Dissertation:

1. Univ. – Prof. Dr. Johannes A. Lercher
2. Univ. – Prof. Dr. Klaus Köhler

Die Dissertation wurde am 25.04. 2002 bei der Technischen Universität München eingereicht und durch die Fakultät für Chemie am 16.05.2002 angenommen.

For Käthe and Klaus
For Andrea

Acknowledgements

Firstly I would like express my gratitude to Prof. Johannes A. Lercher for giving me the possibility to perform my PhD in his laboratory and for many animated and fruitful scientific discussions. His supervision and his critical comments were a source of motivation and inspiration.

I would also like to thank my mentor Dr. Thomas E. Müller, not only for taking care of this work, but especially for creating an atmosphere of personal respect and friendliness in any discussions we had. His high interest in my work resulted in numerous scientific discussions and helpful suggestions.

I am grateful to Dr. Andreas Jentys for introducing me in EXAFS spectroscopy and for the DFT calculations. Thanks also to Dr. Rudy Parton, Dr. Heike Schaffrath and Dr. Robert Pestman of DSM for their fellowship and their motivating interest in my work. DSM is also thanked for the financial contribution to this project. Xaver Hecht, Martin Neukamm and Andreas Marx are thanked for the experimental support.

All members of the TCII group are thanked for the fellowship, for helping me in scientific problems and to feel comfortable during this time. I would like to give special thanks to Jan-Olaf Barth, Linda Callanan, Maria Brandmair and Alexander Hartung often proving the positive sides of laboratory life.

I would like to thank my parents and my sister for giving me the support and encouragement which brought me so far.

Last but not least I would like to thank Andrea.

# I General introduction

New C – N bond forming processes are of fundamental importance in both synthetic organic and industrial chemistry due to the importance of amines and their derivatives in almost all areas of chemistry. Commercially useful products are amines, amides, ammonium and alkylammonium salts, ureas, carbamates, isocyanates and amino acids [1]. In principle one of the most efficient ways for the synthesis of amines would be the direct addition of an amine functionality to a CC multiple bond [2], [3]. The main advantages in industrial applications are (i) the direct formation of the product from mostly readily available and cheap starting materials and (ii) the atom efficiency of the reaction, i.e., each atom of the starting material is present in the product. Hence, there is currently considerable interest in effective catalysts to accomplish such organic transformations. So far, effective catalysts, which allow to perform a variety of hydroamination reactions are not developed. Specific aminations of olefins were performed using homogeneous catalysts. The increasing number of studies concerning suitable heterogeneous catalyst systems clearly shows the industrial importance of such transformations [4], [5], [6], [7], [8], [9].

Regarding the thermodynamics, the addition of amines to alkenes is approximately thermoneutral, whereas the corresponding addition to alkynes is slightly exothermic [10], [11]. The addition of ammonia to acetylene, i.e., is approximately 70 kJ/mol more exothermic than the addition to ethylene [12]. So far, the thermodynamic parameters of amine addition to olefins and to alkynes have not been measured directly.

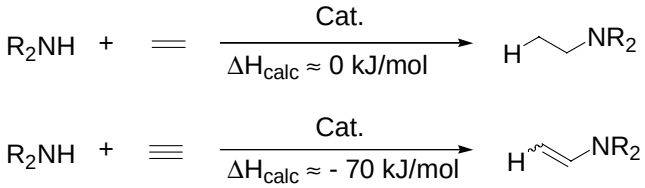


Even though the hydroamination of alkynes is energetically more favorable, a high activation barrier exists [13]. Furthermore, the negative entropy balance of the reaction limits the use of high temperatures.

Approaches that have been employed for developing hydroamination catalysts involve either the activation of the amine or the unsaturated carbon-carbon functional group. One type of catalysts is based on alkali metals [14] or the early transition metals [12], [15], [16], [17], [18], [19]. Disadvantages are that former require harsh reaction conditions and the formation

of by-products is frequently observed, whereas latter catalysts are often very sensitive to water and oxygen. For both it has been established that the reaction proceeds *via* the formation of an amide species. A general trend was observed within the second transition metal series of elements. The formation of amide species is much more exothermic and has a lower activation barrier for the early transition metals. Here, the attractive interaction between the ammonia lone-pair and the empty 4d orbital on the metal prevails. Half empty 4d orbitals, which are characteristic for the elements in the middle of the periodic table, are not suitable as effective lone-pair acceptors [20]. Late transition metals are also efficient hydroamination catalysts, however, function according to a different mechanism. Examples are the cyclization of aminoalkynes with $Zn(CF_3SO_3)_2$ [3], the addition of anilines to terminal alkynes with $[Ru_3(CO)_{12}]$ [21] and the amination of vinylpyridines [22]. In principle, all late transition metals can be employed with Re(I) [23], Ru(0) [24], Rh(I) [25], Ir(I) [26], Cu(I) [3], Pd(II) [3], [27] or Zn(II) [3] being the most suitable. Two different reaction sequences are proposed for hydroamination reactions catalyzed by late transition metal compounds: (i) oxidative addition of the amine to the metal center, followed by insertion of the CC unsaturated moiety into the metal-nitrogen bond and (ii) a nucleophilic attack of the amine on a coordinated CC double or triple bond. However, at present experimental evidence is not sufficient to distinguish unambiguously between the two reaction pathways. Also, different metals may catalyze diverse reaction pathways.

With respect to the oxidative addition route the key step appears to be the activation of the amine by oxidative addition to the metal center. This step requires two electrons of the metal and is established for electron rich metal centers. Typical redox pairs for this reaction are $Rh^{+}/Rh^{3+}$, $Ni^{0}/Ni^{2+}$ and $Pd^{0}/Pd^{2+}$. A catalytic cycle for olefin hydroamination can be realized, if the oxidative addition step can be coupled to an alkene/alkyne insertion process, followed by reductive elimination of the product. This mechanism is supported by stoichiometric experiments showing that, e.g., insertion of norbornene into a Rh–N bond is possible [28]. A mechanism also involving oxidative addition was found for the rhodium catalyzed reaction of styrene with secondary amines [29].

In nucleophilic addition, the activation of the alkene/alkyne is generally accomplished by its coordination to a late transition metal, which renders the π-system more susceptible to attack by exogenous amine nucleophiles. This gives an intermediate 2-aminoalkyl/alkenyl complex. Protonation of the carbon attached to the metal gives the hydroamination product. This mechanism is supported by the observation that metal centers such as $Zn^{2+}$ and $Ag^{+}$ were good catalysts for the cyclization of 6AHI. For these metals, an oxidative addition of the

amine seems unlikely, whereas the reaction sequence based on a nucleophilic attack does not require a change in the oxidation state of the metal center. For palladium based hydroamination catalysts activation of the alkene/alkyne functionality is known [131]. This is supported by a DFT study on olefin *vs*. nitrogen bonding to bidentate Pd (II) catalysts. Alkyl-substituted amines of the general equation $CH_2=CH(CH_2)_nNH_2$ ($n \geq 0$) preferentially bind *via* the unsaturated CC bond to the metal center [30]. Additionally, it was found that olefins coordinated to Pd (II) complexes are highly activated towards nucleophilic addition [141].

Initially, the attention was mainly focused on the development of catalyst systems for intramolecular hydroamination reactions, as these were considered to be ideal model reactions for further developments. More recently, an increasing number of studies concerning intermolecular hydroamination were published. Most of the studies are based on the addition of anilines or substituted anilines to aliphatic or aromatic alkynes [13], [15], [16], [31], [32]. This is probably related to lower Lewis basicity of the aniline nitrogen compared to aliphatic amine nitrogen atoms. The lower Lewis basicity is a consequence of the mesomeric interaction between the amine lone – pair and the phenyl group. In consequence, the coordination strength of the amine to metal cations is reduced. This conclusion is supported by theoretical calculations showing that the stabilization energy for nitrogen coordination on palladium (II) and nickel (II) decreases from methylamine to vinylamine ($CH_2=CHNH_2$) [30]. In case of aniline the lower Lewis basicity leads to a shift in the equilibrium between amine and alkyne coordination towards the latter. In consequence, the unsaturated carbon carbon bond is activated more readily. Intermolecular hydroamination reactions involving alkenes (vinylarenes, derivatives of acrylic acid and cyclohexadiene) are rare. However, in the last two years there were several reports on hydroamination of such olefins with aniline catalyzed by late transition metals [29], [31], [33], [34], [35]. In case of acrylic acid derivatives it was also possible to perform hydroamination with cyclic amines [33]. Except of aniline derivatives, morpholine was used successfully in hydroamination reactions catalyzed by rhodium complexes [13]. Intermolecular hydroamination reactions between primary amines and terminal alkynes are only reported for organoactinide complexes as catalysts [10].

So far, only one process, the synthesis of t-butylamine from ammonia and isobutene, has been commercialized [7]. Since 1986, BASF AG have operated an industrial scale process for the production of *t*-butylamine [36]. The reaction is performed at approximately 270°C and 280 bar, i.e., at supercritical conditions, using a fixed bed catalyst [37]. The maximum conversion of *ca*. 24 % at this temperature makes recyclization of 2-methylpropene and ammonia necessary, which is a costly factor in the commercial operation. This process utilizes

solid acids and especially zeolites in the protonic form as catalysts. These are able to protonate the iso-butene to the corresponding tert-butyl carbenium ion [38], [39]. The latter then reacts with ammonia. The drawback of solid acid catalysts is that their use is restricted to those alkenes which form relatively stable alkoxy groups. Therefore, a new type of catalyst was required which was able to activate the alkene in a different manner.

Thus, we explored the use of late transition metal based heterogeneous catalysts in hydroamination reactions. Zeolites were chosen as support because (i) of their Brønsted acidic properties and (ii) ion exchange leads to a strong localization of the metal cations. The possibility to catalyze hydroamination with such catalysts will be demonstrated for $Zn^{2+}$ ion exchanged zeolites. These materials were fully characterized to understand the relation between the environment of zinc and the catalytic activity of the material (Chapter II). For developing the catalyst system we decided to focus on the intramolecular catalytic cyclization of molecules containing an amine and alkyne/alkene group (Chapter III). The advantage is that, in case of cyclization reactions, more favorable reaction entropy leads to higher rates of reaction. In specific, the cyclization of 6-aminohex-1-yne (6AHI) and 3-aminopropyl-vinylether (3APE) has been studied. To prove that the heterogeneous catalyst system developed is also suitable for intermolecular reactions the hydroamination between aniline and phenylacetylene was examined. The mechanism of hydroamination with late transition metals was studied in detail using a variety of *in situ* techniques, such as *in situ* – EXAFS, NMR and IR spectroscopy (Chapter IV). The comparison of our heterogeneous catalysts with the corresponding homogeneous catalysts enabled us to conclude on co–catalysis between the Lewis acidic metal centers and Brønsted acidic groups (Chapter V).

# II Nature of $Zn^{2+}$ species in $Zn^{2+}$ ion exchanged zeolite BEA


## Abstract

Bifunctional, Lewis and Brønsted acidic molecular sieves were prepared by stepwise zinc ion exchange of zeolite BEA. The relation between the location of the $Zn^{2+}$ cations in the zeolite structure and the Lewis acidity of the metal cations has been explored. IR spectroscopy of adsorbed pyridine and acetonitrile, temperature programmed desorption of ammonia and iso-propylamine and in-situ X-ray absorption spectroscopy were used for a detailed characterization of the material. At low zinc concentrations the cations were preferentially incorporated in the vicinity of two framework aluminum atoms ($< 0.15$ Zn/Al). With increasing loading ($0.15 \leq$ Zn/Al $\leq 0.26$) an additional cation site is created at nearby framework aluminum pairs, in which two zinc cations are bridged by an oxygen atom. At higher zinc loadings ($0.26 <$ Zn/Al $< 0.77$) nano-sized ZnO like species were formed in addition to the other two $Zn^{2+}$ species.


*Keywords*: BEA zeolite, Zinc ion exchange, EXAFS, TPD of iso-propylamine, acetonitrile-$d_3$

## 1. Introduction

Zeolites are widely used as catalysts in organic syntheses [40] and petrochemical processes [41]. Typically, zeolites are employed in the protonic form as solid acid catalysts. Especially, zeolite BEA is frequently utilized in organic syntheses because of its open pore structure. Examples for potential applications of zeolite BEA related to petroleum refining include hydrocarbon transformation reactions from alkylation, over alkylation to catalytic cracking [42], [43]. In petrochemical applications zeolite BEA is used for aromatics alkylation such as alkylation of benzene with ethylene or propylene [43] and the Meerwein-Pondorff-Verley reaction [44], [45], [46].

A number of new catalytic routes utilizing metal-loaded zeolites were also described. Examples are Heck reactions [47], propane aromatization [48], dehydrogenation of small paraffins [49], hydroamination [50], aromatization of *in situ* generated ethylene [51] and hydration of acetylene [52], [53], where zinc cations are the catalytically active species. A detailed understanding of the nature and the location of specific sites is required for an in depth understanding of the observed catalytic reactivity and selectivity [54]. Therefore, the

characterization of transition metal cations located at different ion exchange positions in the zeolite gains increasing attention [68].

The structure of zeolite BEA was first described by Treacy and Newsam [55] and Higgins et. al. [56]. The main channel system of zeolite BEA consists of 12 membered rings of oxygen atoms. Two straight channels are present in the [100] and [010] directions and a third sinusoidal 12 ring channel is located parallel to the [001] direction. These large pore channels intersect leading to an open structure. The secondary building units of this channel system consists of 6, 5, 4 membered ring cages, each of them facing with at least one side to a 12 membered ring channel. The connections between the building units lead to the presence of 6, 5 and 4 membered ring channels in zeolite BEA. Similar building units and channel systems are also present in many other zeolite structures, although an especially high catalytic activity was frequently observed for zeolite BEA [57].

Zeolite BEA is known have a substantial concentration of lattice defects and, thus, is expected to show pronounced variations in the nature and reactivity of cation exchange positions [56]. Aluminum atoms located at some positions of the BEA framework appear to be prone to dehydroxylation or give rise to hydroxyl groups involved in hydrogen bonding networks [58], [59], [60]. Given the potential complexity of the ion exchange sites the corresponding cations may display markedly different catalytic behavior.

For the characterization of these Brønsted and/or Lewis acid sites a number of different spectroscopic methods are described [61], typically by adsorption of basic molecules, such as ammonia, pyridine, alkylamines and acetonitrile [62], [63], [64]. The resulting interaction between the probe molecule and the acidic site can be followed by IR or NMR spectroscopy, calorimetry or thermal desorption. However, only the combination of physicochemical techniques and probe molecules deliver meaningful descriptions of the acidic sites [62], [65]. In this study, we report on the successful combination of the application of different probe molecules, combined with structural information obtained from EXAFS and theoretical calculations. A complete functional description of the cation species in zinc exchanged zeolite BEA has been developed by these means.

## 2. Results

### *2.1 Acid site concentration*

Adsorption of ammonia from the gas phase, followed by TPD was used to quantify the sum of Brønsted and Lewis acid sites [62]. In contrast, TPD after liquid phase ion exchange of $NH_4^+$ cations helped to determine the maximum concentration of Brønsted acid sites [66]. Fig. 1 compiles the TPD of ammonia from H-BEA zeolite using these two methods.

Ammonia TPD from the liquid exchanged BEA zeolite occurred over a wide temperature range with a maximum rate of desorption at 320°C. This is in good agreement with the maxima reported by Timken (300°C) [67] and Miyamoto (290°C) [65].

For better quantification, the adsorption and TPD of ammonia adsorbed from the gas phase was also followed with a microbalance. In this case, the ammonia desorption maximum was observed at 240°C. In contrast to the $NH_4^+$ exchanged sample, a pronounced shoulder with a maximum around 500°C was observed. The total acid site concentration was 0.46 mmol/g. The contributions of the specific sites were quantified by deconvolution of the TPD curve (using Gaussian curves). The concentration of ammonia desorbing from Brønsted acid sites at 320°C (see Fig. 1, β-site) was 0.14 mmol/g. This Brønsted acid site concentration is in good agreement with data reported for a similar BEA zeolite (0.13 mmol/g for a sample with Si/Al = 12.7 ) [68]. The concentration of Brønsted acid sites present in the liquid phase $NH_4^+$ exchanged sample was, however, 0.8 mmol/g. This is in agreement with results reported

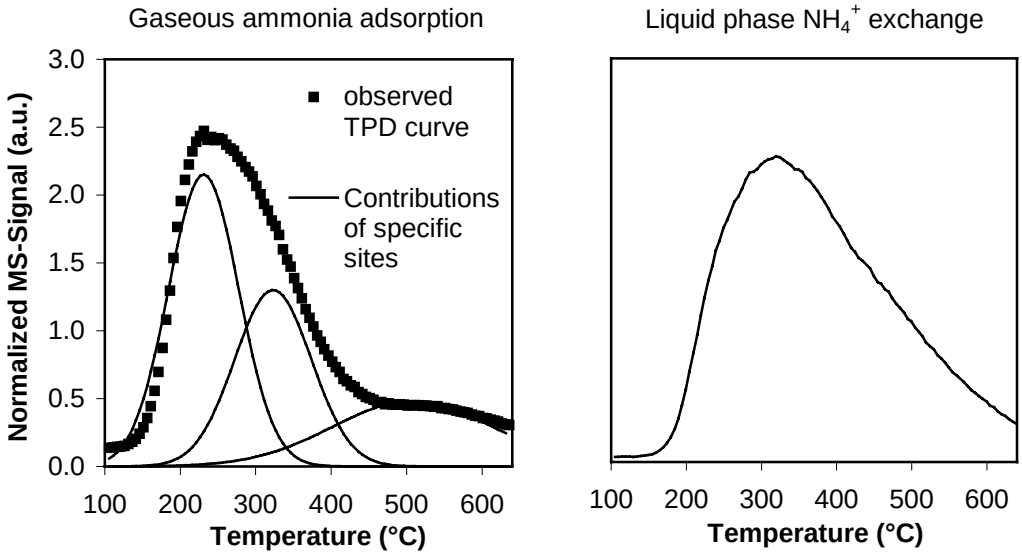


**Fig. 1** Comparison of temperature programmed desorption of ammonia from $NH_4$-BEA prepared by gaseous ammonia adsorption (left) and liquid $NH_4^+$ exchange (right).

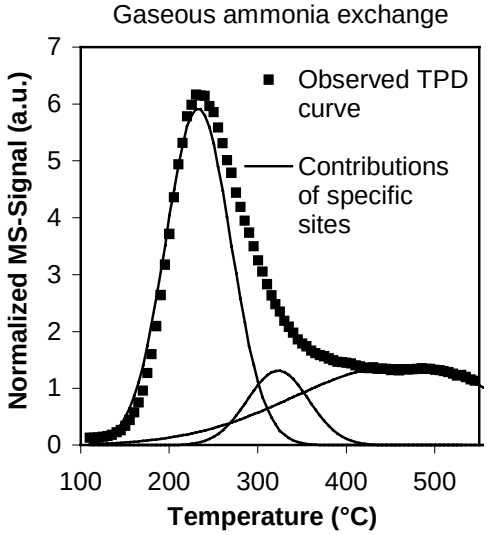


**Fig. 2** Temperature programmed desorption of gaseous adsorbed ammonia from Zn/H-BEA (0.53 Zn/Al).

from Timken et. al., reporting a similar uptake of $NH_4^+$ by zeolite BEA upon liquid ammonia exchange [67]. The increase in Brønsted acid site concentration is attributed to the conversion of $Al^{3+}$ Lewis acid sites to tetrahedral framework aluminum sites.

For characterizing the concentration of acid sites in Zn/H-BEA (0.02 – 0.77 Zn/Al) TPD after adsorption of gaseous $NH_3$ was performed. Deconvolution of the TPD traces revealed desorption peaks similar to H-BEA with maxima at 233, 320 and 452°C denoted α-, β-, γ-site (see Fig. 2 for Zn/H-BEA 0.53 Zn/Al). These desorption maxima were confirmed by separate TPD experiments after outgassing at several elevated temperatures. In Fig. 3, the contribution the individual desorption states (obtained by deconvolution) is given as a function of the zinc loading. The α-peak at 233°C increased linearly with the zinc content of the zeolite. The value of 0.22 mmol/g observed for H-BEA is tentatively attributed due to ammonia adsorbed on weak Lewis acid sites (w-LAS), which are speculated to be hydroxyl nests generated by dealumination.

For Zn/H-BEA, a desorption maximum was observed at 322°C at all zinc loadings (β-site). The same maximum was observed for H-BEA and is, thus, attributed to desorption from Brønsted acid sites. Incorporation of zinc caused a decrease in its concentration from 0.11 to 0.07 mmol/g. This value remained approximately constant upon further increase of the zinc loading. The desorption peak at 452°C (γ-site) increased continuously with the zinc concentration and is attributed to desorption of ammonia from $Zn^{2+}$ cations.

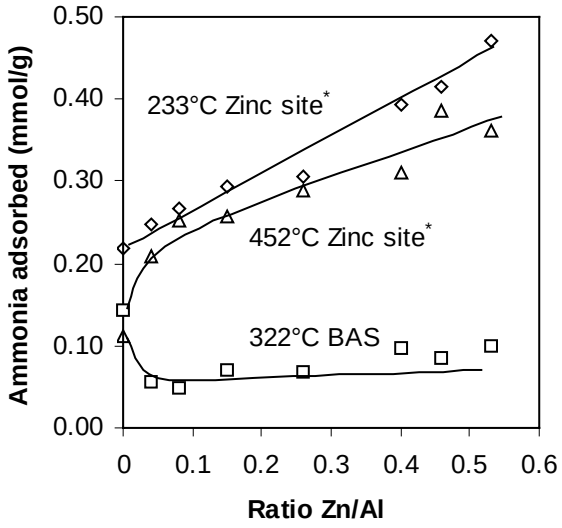


**Fig. 3** Concentration of specific sites in Zn/H-BEA determined by deconvolution of the ammonia TPD curves (*see text).

*2.2 TPD of acetonitrile*

In contrast to ammonia, acetonitrile binds preferentially to zinc cations, while the interaction with Brønsted acid sites is weak [69]. Thus, the TPD of acetonitrile primarily reflects the changes in the nature and concentration of Lewis acid sites related to zinc incorporation. As an example, the TPD curves of acetonitrile for H-BEA and Zn/H-BEA (0.53 Zn/Al) are shown in Fig. 4 for different adsorption temperatures.

The rate of desorption of $CH_3CN$ from the parent H-BEA showed one peak at 156°C. It is attributed to desorption from $Al^{3+}$ Lewis acid sites, formed during the activation procedure.

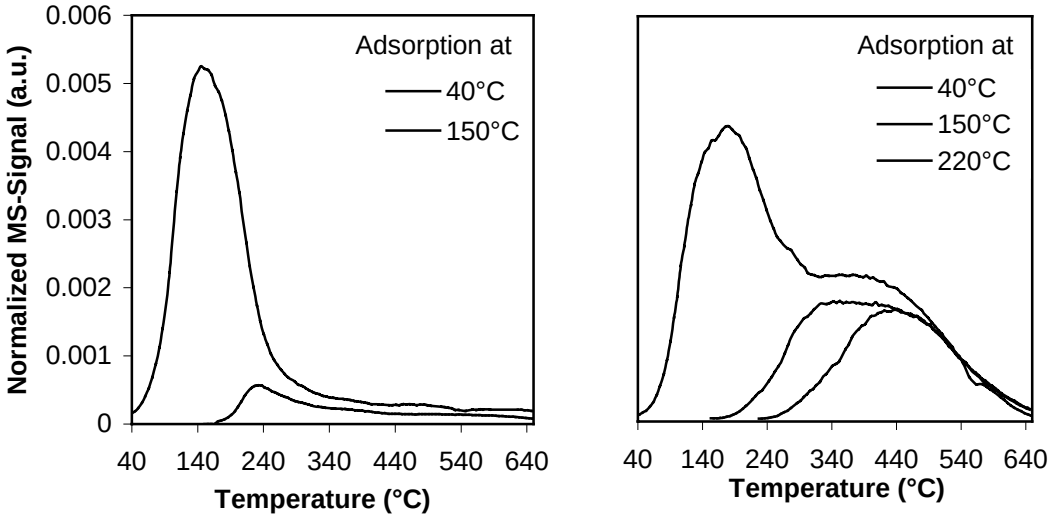


**Fig. 4** Temperature programmed desorption of acetonitrile (adsorbed at the temperatures stated) from H-BEA (left) and Zn/H-BEA (0.53 Zn/Al, right).

The exchange with $Zn^{2+}$ led to major changes in the TPD. At low zinc loading (0.08 Zn/Al), the TPD curve had a maximum of desorption at 156°C with a shoulder ranging from 240 - 600°C (Fig. 5.1). A similar position and width of the maximum was observed as for the H-BEA zeolite, however the intensity decreased slightly. Therefore, we conclude that the desorption maximum at 156°C is based on desorption from $Al^{3+}$ Lewis acid sites as concluded for H-BEA, however the concentration of this sites decreased upon zinc exchange. The shoulder ranging from 240 – 600°C is attributed to desorption of acetonitrile from $Zn^{2+}$ cations.

For Zn/H-BEA (0.53 Zn/Al), the TPD curve had a maximum of desorption at 176°C with a shoulder ranging from 240 – 600°C (Fig 5.2). Note that in this case the maximum (176°C) was observed at a slightly higher temperature as observed for H-BEA (156°C), while, in comparison, the intensity decreased and the peak width increased. This indicates that for Zn/H-BEA (0.53 Zn/Al) this desorption state is formed by zinc incorporation and is not based $Al^{3+}$ Lewis acid sites. Consequently, it is attributed to desorption from zinc Lewis acid sites (zinc site A). Similar to Zn/H-BEA (0.08 Zn/Al) the shoulder ranging from 240 – 600°C is attributed to acetonitrile adsorbed on $Zn^{2+}$ cations.

In summary, from the curves obtained for TPD of acetonitrile we conclude that at low zinc loading two desorption states are present (156°C and 240 - 600°C) which are based on desorption of $CH_3CN$ from $Al^{3+}$ and $Zn^{2+}$ Lewis acid sites, respectively. Increase of the zinc

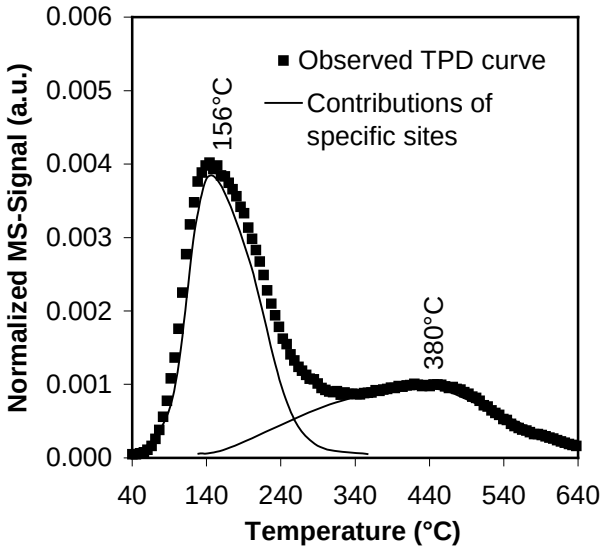


**Fig 5.1** Temperature programmed desorption of acetonitrile from Zn/H-BEA (0.08 Zn/Al).

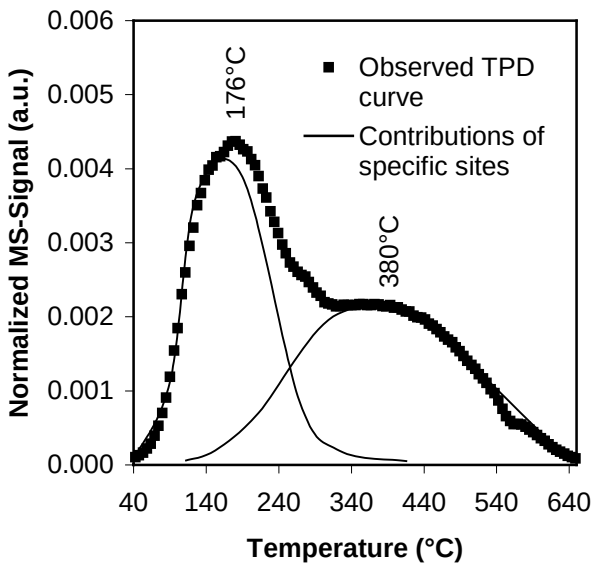


**Fig. 5.2** Temperature programmed desorption of acetonitrile from Zn/H-BEA (0.53 Zn/Al).

loading up to 0.53 Zn/Al led to the formation of a new desorption state showing acetonitrile desorption at 176°C, while the $Al^{3+}$ Lewis acid site based desorption state disappeared. The shoulder ranging from 240 – 600°C is attributed to acetonitrile adsorbed on $Zn^{2+}$ cations. Its width indicates that the zinc ions are located at different sites in the zeolite.

In order to determine the number of desorption states and the temperatures of maximum desorption TPD experiments were performed employing different adsorption temperatures (Fig. 4). By subtracting the TPD curve obtained at higher adsorption temperatures from the TPD curve obtained at lower temperatures, two maxima at 359°C and 456°C (zinc site B and C) were revealed.

**Table 2** Absolute and relative concentration of zinc sites in Zn/H-BEA (0.53 Zn/Al) as determined by adsorption of $CH_3CN$ (* see text).

| | Desorption temperature (°C) | Amount of $CH_3CN$ adsorbed on $Zn^{2+}$ (mmol/g) |
|---|---|---|
| Zinc site A | 176 | not determined |
| Zinc site B | 359 | 0.132 (20 %*) |
| Zinc site C | 456 | 0.330 (50 %*) |

To confirm the concentration of acetonitrile molecules adsorbed on these zinc sites, microbalance experiments were performed. At an equilibration temperature of 220°C, adsorption occurs only on zinc site C (see Fig. 4). In this case, the absolute amount of $CH_3CN$ adsorbed on the sample was 0.330 mmol/g and the ratio of adsorbed $CH_3CN$ molecules to $Zn^{2+}$ cations was 0.5. This indicates that 50 % of the zinc cations interact with acetonitrile.

At an equilibration temperature of 150°C, $CH_3CN$ adsorbs only on zinc sites B and C (359°C and 456°C, respectively). The ratio of adsorbed $CH_3CN$ to $Zn^{2+}$ cations was 0.7. Note that at this temperature, adsorption on zinc sites A sites (176°C) is negligible (stated as not determined in Table 2). The absolute concentration of $CH_3CN$ adsorbed on the sample was 0.462 mmol/g. With the known concentration of site C, the concentration of $Zn^{2+}$ site B in Zn/H-BEA (0.53 Zn/Al) is 0.132 mmol/g. This corresponds to 20 % of the total zinc content.

### *2.3 TPD of iso-propylamine from zinc exchanged BEA zeolites*

TPD of reactive probe molecules, such as iso-propylamine, allows distinguishing between physisorbed and chemisorbed molecules. Iso-propylamine, in particular, has been described as a probe molecule that specifically interacts with Brønsted acid sites [62]. These catalyze Hoffmann elimination of chemisorbed amine molecules (Equ. 1). In this case, ammonia and propene desorb simultaneously upon decomposition. However, amines will also adsorb on Lewis acidic zinc cations. Reverse hydroamination is possible on $Zn^{2+}$ sites [70],

[71], [72] leading to ammonia and propene (Equ. 2). Note that in the latter case ammonia desorbs first from the $Zn^{2+}$ sites followed by propene.

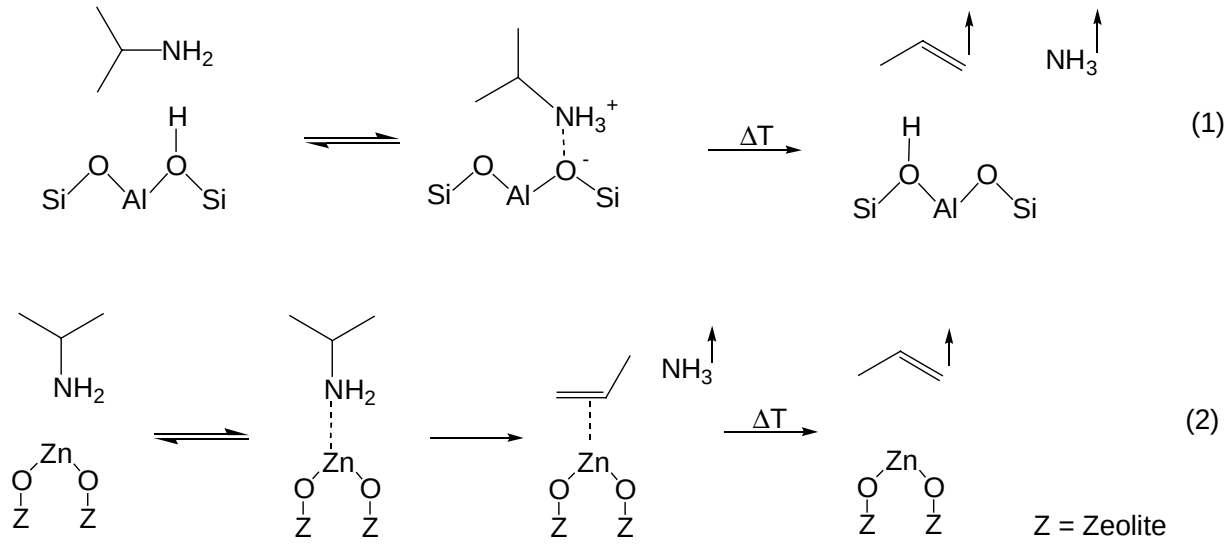


The TPD of iso-propylamine was measured for all Zn/H-BEA zeolite samples. The equilibration with iso-propylamine was carried out at 40°C. At temperatures below 260°C, all samples exhibited a broad desorption peak of iso-propylamine, which is attributed to desorbing physisorbed molecules. Reaction products, i.e., ammonia and propene, were observed between 240°C and 640°C. For H-BEA, propene started to desorb at 290°C and the rate of propene desorption reached a maximum at 347°C. At temperatures above 420°C propene was not observed. Similarly to propene, ammonia started to desorb from H-BEA at 290°C. However, the maximum of ammonia desorption was found at 365°C and the intensity was lower compared to propene desorption. Additionally, desorption of ammonia exhibited a broad desorption shoulder up to 620°C. TPD of ammonia from the parent H-BEA has shown that ammonia desorbs from Lewis acid sites in this temperature range. Thus, the desorption of ammonia above 420°C is tentatively attributed to readsorption of ammonia on these Lewis acid sites and subsequent release at the higher temperature.

Overall TPD of iso-propylamine from Zn/H-BEA showed desorption peaks of propene at 347, 394 and 476°C (Fig. 6). Comparison with the parent H-BEA shows that propene desorption at 347°C is related to Hoffmann elimination on remaining Brønsted acid sites. This desorption state is found in all zinc exchanged samples. The desorption states for propene at 394 and 476°C are attributed to two different sites present in zinc exchanged BEA zeolite.

For H-BEA desorption of ammonia and propene occurred in parallel at lower temperatures. In case of Zn/H-BEA, ammonia and propene do not desorb in parallel. As an example for Zn/H-BEA (0.77 Zn/Al) propene started to desorb at 270°C while ammonia

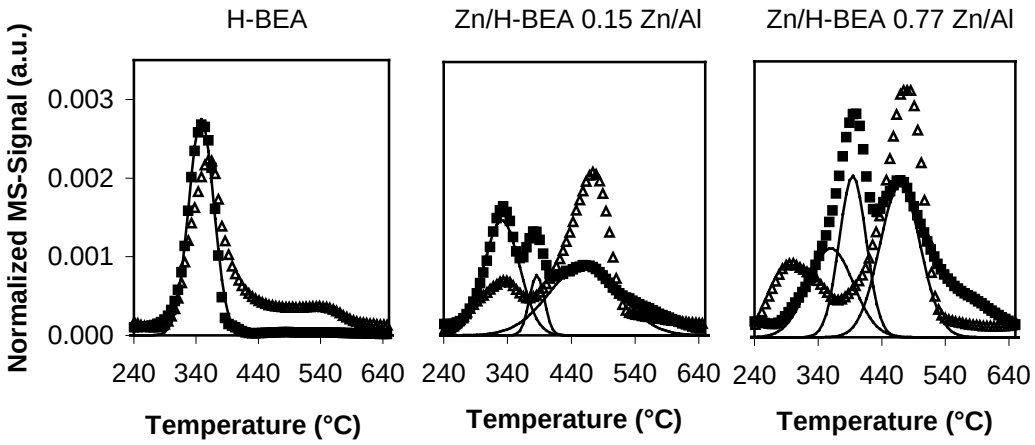


**Fig. 6** Deconvolution of TPD curves of propene. Shown are (i) the concentration of propene desorbing from the surface (squares), (ii) the concentration of ammonia desorbing from the surface (triangle) and (iii) the contribution of single sites to the TPD curves (lines).

started to desorb already at 240°. With increasing $Zn^{2+}$ concentration a broad maximum of ammonia desorption occurs at around 260°C. From this observations it is concluded, that for the desorption state assigned to Brønsted acid sites ammonia and propene desorption occurs in parallel. For the desorption state exhibiting propene desorption at 394°C, the corresponding ammonia desorption is shifted to around 260°C. Thus, these sites effectively catalyze the reverse hydroamination reaction. A second ammonia desorption maximum appeared with increasing intensity at 480°C. This peak occurred in parallel to the desorption peak of propene at 476°C, but exhibited a significantly higher intensity. This can be explained by parallel desorption of ammonia and propene from the second site caused by the higher temperature. The higher intensity of the ammonia peak is caused by additional desorption of ammonia from $Al^{3+}$ Lewis acid sites. These are covered by readsorption of ammonia evolved in a surface reaction at lower temperatures.

The TPD curves of propene were deconvoluted using three Gaussian curves (Fig. 6). The desorption maxima were fixed to 374°C (characteristic for Brønsted acid sites), 394°C and 476°C (characteristic for zinc Lewis acid sites) and the TPD traces were fitted by varying height and width of the Gaussian curves. The deconvolution of the ammonia traces lead not to a clear trend, probably because pronounced readsorption of ammonia changed the relative intensities of the peaks. Therefore, the following discussion is focused on propene evolution. The thermal desorption rates were normalized to the concentration of Brønsted acid sites in the samples, as measured by IR spectroscopy of adsorbed acetonitrile-$d_3$, assuming that iso-propylamine and acetonitrile-$d_3$ adsorb on the same Brønsted acid sites. The integrated areas of the three peaks as a function of the zinc loading are given in Fig. 7.

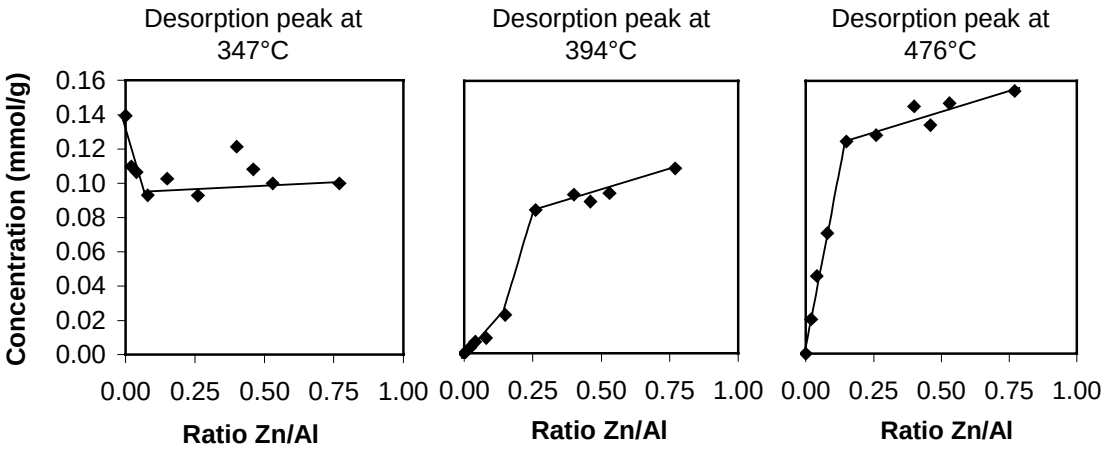


**Fig. 7** Quantification of different sites in Zn/H-BEA zeolites determined from propene desorption observed in iso-propylamine TPD. The desorption peak at 347°C is attributed to Brønsted sites, the peaks at 394 and 476°C to zinc sites.

The desorption peak attributed to reaction on Brønsted acid sites (347°C) decreased in intensity from 0-0.08 Zn/Al and remained constant upon further zinc incorporation. The two desorption peaks at 394°C and 476°C, both assigned to Lewis acid sites, complement each other. The intensity of the desorption peak at 476°C increased fast in the range 0-0.15 Zn/Al, whereas only a small increase in the concentration of the peak at 394°C was observed. Upon increasing the $Zn^{2+}$ concentration to 0.26 Zn/Al, the intensity of the desorption peak at 476°C increased slightly, whereas a sudden rise in the intensity of the peak at 394°C was observed. At even higher zinc loadings, the intensity of both peaks increased gradually. This indicates that the peaks at 476°C and 394°C correspond to two individual zinc sites. A third zinc site must be present at zinc loadings above 0.26 Zn/Al. This site was, however, not observed in iso-propylamine TPD and it is concluded that it does not catalyze the decomposition of iso-propylamine.

From the quantitative analysis of the TPD maxima at 394°C and 476°C, the calculated zinc concentrations can be compared with the values obtained from AAS. Up to a zinc loading of 0.26 Zn/Al the calculated zinc concentrations were constantly for around 24 % lower than the values determined by AAS (table 3). This indicates that a systematic difference between the two methods exists. However, the trend in zinc concentration is similar for both methods. By further increase of the zinc loading the difference between the calculated (TPD) and the measured (AAS) zinc concentration increased, indicating that an increasing concentration of zinc cations is present in a state not detected by iso-propylamine TPD.

Note that these observations are in good agreement with the results from acetonitrile TPD, which showed for Zn/H-BEA (0.53 Zn/Al, 0.66 mmol Zn/g) that three zinc species are present showing acetonitrile desorption at 176, 359 and 456°C (zinc site A, B and C). By

temperature programmed desorption of iso-propylamine two zinc species were identified showing propene desorption at 394 and 476°C. It is most likely that desorption states exhibiting desorption of nitrogen containing probe molecules in the same range of temperature are identical as comparable Lewis acidities and basicities are present. From this it is concluded that the zinc sites B and C identified by TPD of acetonitrile are identical to the desorption states showing propene desorption at 394 and 476°C.

*2.4 IR spectroscopy of Zn/H-BEA*

IR spectra in the region of the OH stretching vibration of BEA zeolites with various zinc loadings are compared in Fig. 8. The most prominent band at 3745 $cm^{-1}$ is attributed to terminal silanol groups of the zeolite. The band at 3612 $cm^{-1}$ is attributed to the OH groups associated with isolated (unperturbed) Brønsted acid sites. A broad absorption band ranging from 3750-3200 $cm^{-1}$ with maximum intensity at around 3600 $cm^{-1}$ was present in all spectra (perturbed Brønsted sites). In accordance with the literature this is explained by the interaction of the Brønsted acid sites with framework oxygens [59], [78], or by the presence of hydrogen bonded silanol groups at defect sites [73]. Additionally, two bands with low intensity were noted. A high frequency band at 3780 $cm^{-1}$, assigned to hydroxyl groups on extra framework aluminum oxide, was only observed in the spectra of the parent H-BEA zeolite. Apparently, these hydroxyl groups had been removed upon zinc exchange [59], [68]. A band at 3660 $cm^{-1}$ is assigned to OH groups coordinated to aluminum or mixed oxide clusters in the zeolite

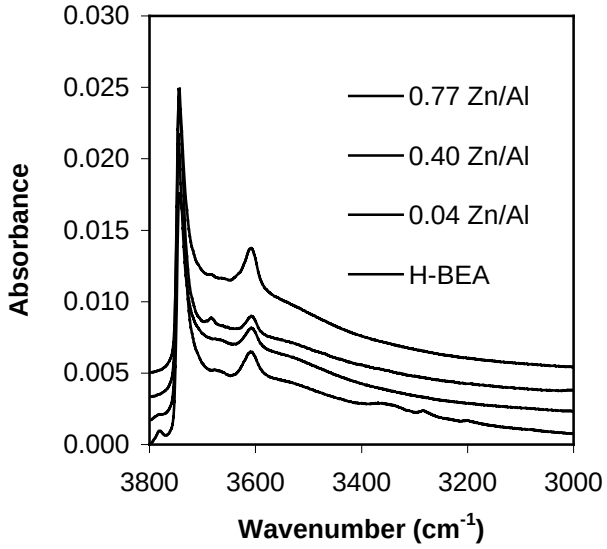


**Fig. 8** FTIR spectra of zinc exchanged BEA zeolites with various zinc loadings. The spectra were recorded after activation at 450°C.

pores. This band was observed in the parent H-BEA zeolite and in two higher exchanged zeolites (0.40 and 0.46 Zn/Al).

Deuteration with $D_2O$ was used to determine, which sites are sufficiently accessible. Deuteration of H-BEA and Zn/H-BEA (0.15 Zn/Al) zeolites led to a shift of all OH bands (3750 - 3050 $cm^{-1}$) to lower wavenumbers (2800 - 2400 $cm^{-1}$). The bands generated between 2800 and 2400 $cm^{-1}$ precisely mirrored the bands between 3750 and 3050 $cm^{-1}$ indicating that all OH groups in zeolite BEA were converted to OD bands and are, hence, accessible.

Zinc exchange did not influence the terminal silanol groups (3745 $cm^{-1}$) of zeolite BEA. The concentration of unperturbed Brønsted acid sites (3612 $cm^{-1}$) decreased slightly with the zinc content (0 – 0.15 Zn/Al), whereas at higher loading their concentration increased. However, these changes in concentration were insignificant indicating that these Brønsted acid sites are not affected by zinc ion-exchange. The concentration of the perturbed Brønsted sites (3750-3200 $cm^{-1}$) was not quantified, as the hydrogen bonding interaction changes the molar extinction coefficient of the OH stretch vibration in dependence of the intensity of the interaction.

### *2.5 IR spectroscopy of adsorbed acetonitrile-$d_3$*

Following the suggestions of ref. [68], [74] the IR spectra of adsorbed acetonitrile-$d_3$ were used to assess the relative concentration of Lewis and Brønsted acid sites. For Zn/H-BEA (0.08 Zn/Al), the influence of adsorbed acetonitrile-$d_3$ on the OH stretching vibrations is shown in Fig. 9. While the band at 3740 $cm^{-1}$ regained its original intensity during outgassing, the band at 3612 $cm^{-1}$ did not. Clearly, the acetonitrile molecules interact weakly with the silanol groups, while interacting stronger with the unperturbed Brønsted acid sites. In contrast, the integral intensity of the broad absorption band did not change significantly. Thus, interactions between acetonitrile-$d_3$ and perturbed Brønsted acid sites were not detected. This is explained by the weak basicity of the nitrile nitrogen, which is apparently insufficient to break the existing hydrogen bonds [75].

Gaseous acetonitrile-$d_3$ has a strong stretching vibration band $\nu_{st}(C\equiv N)$ at 2594 $cm^{-1}$, which shifted significantly upon adsorption on zeolite BEA. On the parent H-BEA zeolite a structured absorption band in the range 2220 – 2360 $cm^{-1}$ was observed, which had contributions of four bands at 2323, 2298, 2273 and 2250 $cm^{-1}$. These are attributed to interaction of the nitrile group with $Al^{3+}$ Lewis acid sites (Al LAS), Brønsted acid sites (BAS), silanol groups and to the asymmetric stretch vibration of physisorbed $CD_3CN$, respectively [68], [76]. With the exchange of $Zn^{2+}$ an additional band appeared at 2314 $cm^{-1}$,

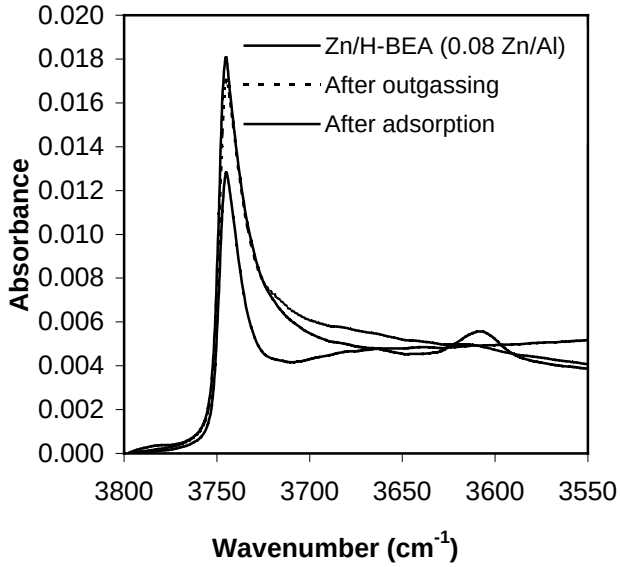


**Fig. 9** IR-spectra of Zn/H-BEA (0.08 Zn/Al) after activation, after adsorption of acetonitrile-$d_3$ (at 35°C and 0.1 mbar) and after outgassing at 35°C for 1 h

which increased in intensity with the $Zn^{2+}$ loading (Fig. 10). In parallel, the signal at 2323 $cm^{-1}$ due to interaction with $Al^{3+}$ Lewis acid sites decreased. The contributions of the different bands (2323, 2314 and 2298 $cm^{-1}$) were determined by deconvolution. In Fig. 11 the approach is illustrated by the spectrum of acetonitrile-$d_3$ for Zn/H-BEA with Zn/Al = 0.08.

By using different outgassing temperatures the desorption states observed in TPD of acetonitrile were confirmed. In case of the parent H-BEA zeolite after outgassing at 156°C a single absorption band at 2323 $cm^{-1}$ was observed indicating adsorption on $Al^{3+}$ Lewis acid sites. This clearly indicates that in TPD of acetonitrile the desorption state showing maximum acetonitrile desorption at 156°C is based on $Al^{3+}$ Lewis acid sites. TPD of acetonitrile from

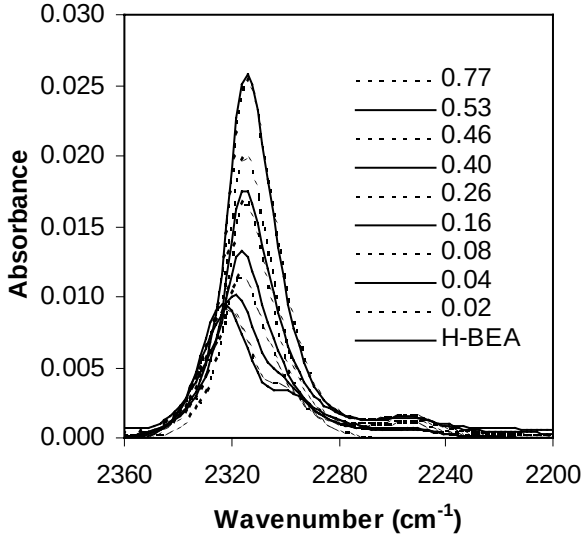


**Fig. 10** IR spectra of acetonitrile-$d_3$ adsorbed on zinc exchanged BEA zeolites.

Zn/H-BEA (0.53 Zn/Al) showed a desorption maximum at 176°C. This was assigned to a desorption state based on zinc Lewis acid sites. To confirm this assignment acetonitrile-$d_3$ was adsorbed on Zn/H-BEA (0.53 Zn/Al) at 35°C, outgassed and heated up to 176°C. IR spectra were taken in regularly intervals. At 35°C absorption bands were found at 2314 and 2298 $cm^{-1}$, indicating the presence of zinc and Brønsted acid sites in this material. With increasing temperature the contribution based on interaction of acetonitrile-$d_3$ with Brønsted acid sites decreased. At the final temperature only the peak at 2314 $cm^{-1}$ was present indicating adsorption on zinc Lewis acid sites. This proves that in TPD of acetonitrile the desorption state showing maximum $CH_3CN$ desorption at 176°C is based on zinc Lewis acid sites.

The concentrations of $Al^{3+}$ Lewis and Brønsted acid sites were then evaluated using the extinction coefficients $\varepsilon_{Al\ LAS} = 3.62 \pm 0.16$ cm/µmol and $\varepsilon_{BAS} = 2.05 \pm 0.10$ cm/µmol [77]. The concentration in accessible $Zn^{2+}$ based Lewis acid sites is given as integral intensity, as the corresponding extinction was not available. In Fig. 12, the results from the deconvolution are summarized. The fraction of acetonitrile-$d_3$ molecules adsorbing on silanol groups was negligible and independent from the zinc loading. The concentration of Brønsted acid sites decreased from 0.14 (H-BEA) to 0.11 mmol/g (Zn/H-BEA 0.04 Zn/Al) and remained constant upon further zinc incorporation. The concentration of $Al^{3+}$ Lewis acid sites decreased linearly from 0.27 (H-BEA) to 0 mmol/g (Zn/H-BEA 0.26 Zn/Al). The trend in the intensity of the band characteristic for $Zn^{2+}$ based Lewis acid sites can be divided in three sections of linear

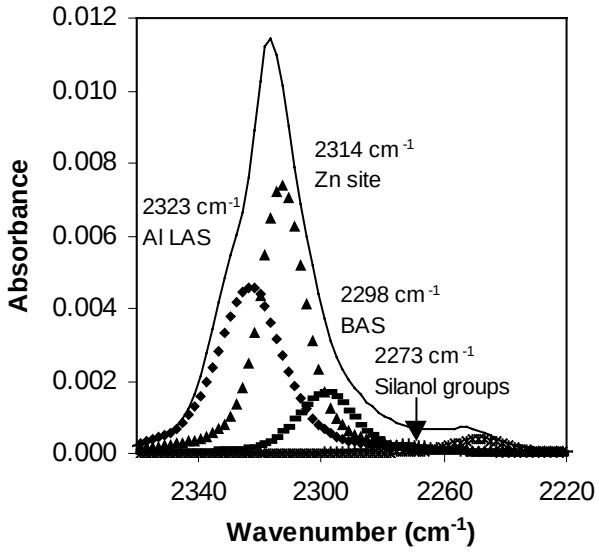


**Fig. 11** Deconvolution of the IR band due to acetonitrile-$d_3$ adsorbed on zinc exchanged BEA zeolite (0.08 Zn/Al).

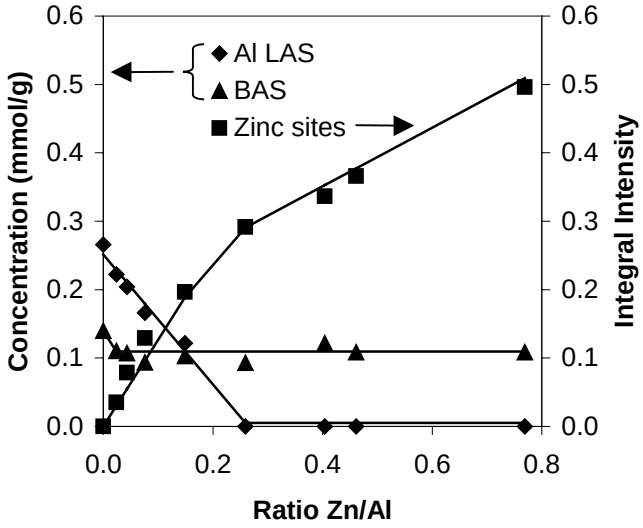


**Fig. 12** Results from deconvolution of the CN stretch vibration area. Shown is the dependence between the concentration of Brønsted, Lewis and zinc sites and the zinc loading (determined by AAS).

increase differing in slope (Fig. 12). A steep increase in the intensity occurred from 0 to 0.15 Zn/Al, while from 0.15 to 0.26 Zn/Al and from 0.26 to 0.77 Zn/Al the increase related to the amount of $Zn^{2+}$ in the zeolite was lower.

For the parent H-BEA it is known that pairs of Brønsted acid sites in vicinity are unstable upon temperature treatment and easily dehydroxylate by formation of one $Al^{3+}$ Lewis site[58,68]. Assuming that, (i) divalent zinc cations are exchanged preferentially for two neighboring Brønsted sites and (ii) that these Brønsted acid sites are dehydroxylated forming one $Al^{3+}$ Lewis acid site, if not stabilized by $Zn^{2+}$. The total concentration of acid sites $c_{AS}^{tot}$ can be calculated according to Equ. 3

$$c_{AS}^{tot} = c_{BAS} + 2c_{Al\,LAS} + 2c_{Zn\,site} \qquad (3)$$

The concentration of Brønsted and aluminum Lewis acid sites was derived from the IR-spectra of adsorbed acetonitrile, whereas the total zinc concentration was taken from AAS measurements. When applying this formula, the total concentration of acid sites was approximately constant in the range 0 – 0.26 Zn/Al (Table 3). It was shown before that the concentration of unperturbed Brønsted acid sites $c_{BAS}$ remained constant over the whole range of zinc exchange. Therefore, the sum of the concentration of $Al^{3+}$ Lewis acid sites and the zinc sites observed by IR spectroscopy is concluded to be constant. Furthermore, in the range 0 – 0.26 Zn/Al, the concentration of zinc cations in the material should be inversely proportional to the decrease of $Al^{3+}$ Lewis acid sites (Equ. 4).

$$c_{Zn} = c_{Al\,LAS}(H-BEA) - c_{Al\,LAS}(Zn/H-BEA) \quad (4)$$

The concentration of zinc calculated from this equation is in excellent agreement with the zinc concentration determined by AAS (Table 3). Thus, with low zinc concentrations the zinc cations bind exclusively to pairs of Brønsted acid sites (< 0.26 Zn/Al). At a zinc content of 0.26 Zn/Al, each pair of Brønsted acid sites is stabilized by one zinc cation. At a higher zinc loading, additional pairs of Brønsted acid sites are not accessible and another mechanism of zinc incorporation must exist.

These conclusions are supported by $^{27}$Al NMR spectroscopy. A hydrated sample of the parent H-BEA zeolite contained some octahedral aluminum. After zinc exchange nearly all octahedral aluminum was absent, while the concentration of tetrahedral aluminum increased. These results confirm that pairs of Brønsted acid sites are dehydroxylated to aluminum Lewis acid sites, if not stabilized by a coordinated zinc cation.

**Table 3** Quantitative IR, TPD and chemical analysis of zinc exchanged zeolites (in mmol/g).

| | AAS | | | IR $CD_3CN$ | | | TPD of iso-propylamine | | IR Pyridine |
|---|---|---|---|---|---|---|---|---|---|
| | Zn | Al | Zn/Al | Al-Lewis sites[a] | Total Acid sites[b] | Zn on close aluminum pairs[c] | Zn on close aluminum pairs[d] | Zn on nearby aluminum pairs[d] | Lewis acid sites[e] |
| H-BEA | - | 1.36 | 0.00 | 0.266 | 0.671 | - | - | - | 0.147 |
| Zn/H-BEA | 0.03 | 1.37 | 0.02 | 0.222 | 0.615 | 0.04 | 0.020 | 0.003 | - |
| Zn/H-BEA | 0.06 | 1.27 | 0.04 | 0.204 | 0.635 | 0.06 | 0.046 | 0.007 | 0.116 |
| Zn/H-BEA | 0.11 | 1.47 | 0.08 | 0.166 | 0.645 | 0.10 | 0.071 | 0.009 | 0.142 |
| Zn/H-BEA | 0.20 | 1.37 | 0.15 | 0.122 | 0.707 | 0.14 | 0.124 | 0.023 | 0.133 |
| Zn/H-BEA | 0.31 | 1.18 | 0.26 | 0.000 | 0.713 | 0.27 | 0.128 | 0.084 | 0.148 |
| Zn/H-BEA | 0.49 | 1.21 | 0.40 | 0.000 | - | - | 0.145 | 0.093 | - |
| Zn/H-BEA | 0.54 | 1.18 | 0.46 | 0.000 | - | - | 0.134 | 0.089 | 0.196 |
| Zn/H-BEA | 0.66 | 1.24 | 0.53 | 0.000 | - | - | 0.147 | 0.094 | 0.269 |
| Zn/H-BEA | 0.86 | 1.12 | 0.77 | 0.000 | - | - | 0.154 | 0.109 | 0.260 |

[a] Determined from the integral intensity at 2323 $cm^{-1}$
[b] Calculated from equation (3)
[c] Calculated from equation (4)
[d] Desorbing propene in mmol/g
[e] Determined from the integral intensity at 1456 $cm^{-1}$, after outgassing at 450°C for 1 h

### *2.6 IR spectroscopy of adsorbed pyridine*

Adsorption of pyridine on zeolites leads to the formation of bands in the region 1560-1440 $cm^{-1}$ due to ring vibrations of adsorbed pyridine. Pyridine adsorbed on Brønsted acid sites shows a characteristic band at 1546 $cm^{-1}$, whereas the interaction with Lewis acid sites leads to bands between 1442 and 1456 $cm^{-1}$ [78]. Upon zinc exchange the shape and position

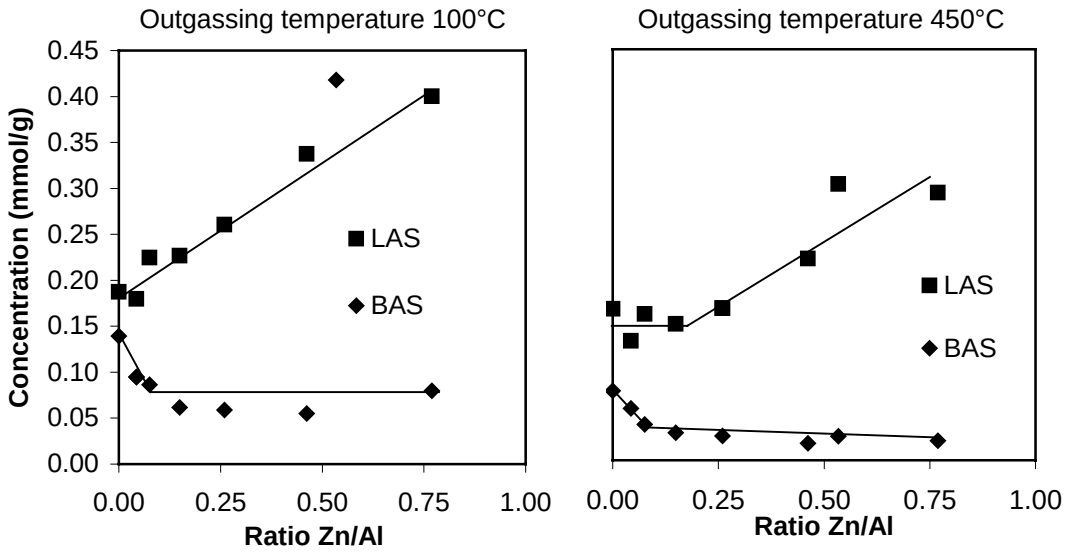


**Fig. 13** Concentration of Lewis and Brønsted acid sites of Zn/H-BEA as function of the zinc loading derived from IR-spectra of adsorbed pyridine.

of the band at 1456 $cm^{-1}$ remained unchanged, although the intensity varied with the zinc content. Thus, it was not possible to distinguish between $Al^{3+}$ and $Zn^{2+}$ Lewis acid sites from the spectra obtained.

After adsorption of pyridine on Zn/H-BEA and outgassing at 100°C, the experiments were completed by increasing the outgassing temperature to 450°C. In Fig. 13, the integral intensities of the signals at 1546 $cm^{-1}$ and 1456 $cm^{-1}$ were used for calculation of the concentration of Brønsted and Lewis acid sites ($\varepsilon_{BAS}$ = 1.3 cm/µmol and $\varepsilon_{LAS}$ = 1.5 cm/µmol, respectively) [78]. The Brønsted acid site concentration of the parent H-BEA (0.14 mmol/g, determined by adsorption of ammonia) is reflected in the integral intensity of the band at 1546 $cm^{-1}$. The trend in Brønsted sites was quite similar at 100 and 450°C. The concentration of adsorbed pyridine decreased with the zinc loading in the range from 0-0.08 Zn/Al and stayed constant with further zinc incorporation up to 0.77 Zn/Al. The major difference was the lower number of pyridine molecules adsorbed on Brønsted acid sites at 450°C in comparison to 100°C, while the number of pyridine molecules adsorbed on Lewis acid sites of H-BEA was quite similar for both temperatures (Table 3).

For the parent H-BEA zeolite the concentration of pyridine adsorbed on Lewis acid sites remained unaffected by the outgassing temperature (0.19 mmol/g). Apparently, desorption from $Al^{3+}$ Lewis acid sites did not occur at temperatures up to 450°C. For pyridine adsorbed on Zn/H-BEA at 100°C, the band assigned to interaction with Lewis acid sites increased continually with the zinc loading. In contrast, after outgassing at 450°C this band remained of equal intensity and increased above 0.26 Zn/Al.

*2.7 X-ray absorption Near-Edge Spectra*

The excitation of Zn 1s electrons causes a sharp increase in X-ray absorption near 9659 eV. The energy is a function of the electron density on the absorber atom and conceptually, decreasing electron density leads to a shift of the edge to higher energies [79], [48]. Therefore, a comparison of the edge positions of the zinc exchanged zeolites with reference compounds (i. e., Zn and ZnO) allows estimating the average charge of the incorporated zinc species. In Table 4 the edge energies of Zn/H-BEA (0.08 and 0.53 Zn/Al) before and after activation with those of Zn metal and ZnO used as reference materials are compared.

**Table 4** Absorption edge energies at the Zn K-edge for Zn/H-BEA and Zn metal, ZnO

| Sample | Zn/Al | Oxidation state | Edge energy (eV) | Sample treatment |
|---|---|---|---|---|
| Zinc metal | | $Zn^0$ | 9659.3 | - |
| ZnO | | $Zn^{2+}$ | 9661.8 | - |
| Zn/H-BEA | 0.08 | $Zn^{2+}$ | 9663.5 | Before activation |
| Zn/H-BEA | 0.08 | $Zn^{2+}$ | 9663.0 | After activation[a] |
| Zn/H-BEA | 0.53 | $Zn^{2+}$ | 9663.1 | After activation |

[a] RT – 450°C 10°C/min; 450°C 60 min

The edge energy for zinc metal and ZnO were 9659.3 and 9661.8 eV, respectively. The change of the oxidation state from 0 to 2+ leads to a shift in edge energy of 2.5 eV. For the untreated Zn/H-BEA zeolite the largest shift was observed (edge energy 9663.5 eV), while activation caused a slight decrease in the edge position (edge energy 9663.0 eV). Note that X-ray absorption spectroscopy determines the average charge of all zinc species present in the sample. The slight decrease in edge energy after activation probably reflects changes in the coordination sphere of the zinc cations by the loss of $H_2O$ ligands. For all zinc exchanged zeolites measured, the edge energies indicate that the zinc is present in the oxidation state 2+.

This is also confirmed by the Zn 1s XANES of the zeolites investigated (see Fig. 14). For the sample before activation the hydratation of $Zn^{2+}$ resulted in a marked peak above the absorption edge, while after activation two peaks, one presumably for $Zn^{2+}$ in ion exchange position and one for $Zn^{2+}$ in an oxide environment, were found. In contrast, zinc oxide showed one marked peak above the absorption edge indicating a well defined chemical structure.

The X-ray absorption data on zinc exchanged BEA zeolite (0.08 Zn/Al) (Fig. 14) showed the same dehydration-hydration sequence as reported by Iglesia et. al. for Zn/H-ZSM-5 (Zn/Al 0-0.19) [48]. This indicates that similar zinc species are present in both materials.

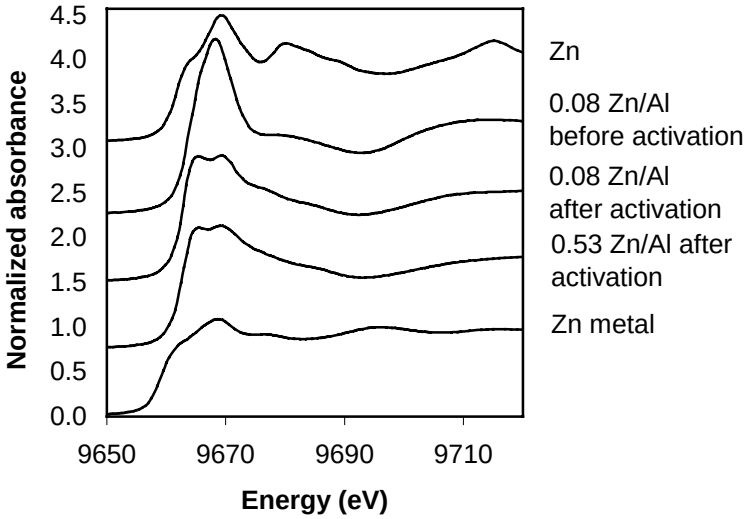


**Fig. 14** Zn K-edge X-ray absorption near-edge spectra of Zn/H-BEA (0.08 and 0.53 Zn/Al) and zinc reference materials.

*2.8 Extended X-ray Absorption Fine Structure (EXAFS)*

EXAFS measurements were performed to examine whether Zn-O, O-Zn-O or Zn-Zn species are present in the zinc exchanged zeolites. The Fourier transformed EXAFS oscillations of the samples and reference materials (ZnO and Zn metal), are shown in Fig. 15. In the non phase-shift corrected Fourier transformed EXAFS oscillations, zinc oxide exhibited a peak at 1.57 Å, which reflects the contributions of the six nearest oxygen neighbors at a distance of 1.95 Å. Both zeolite samples exhibited a similar peak at around 1.57 Å, which indicates that $Zn^{2+}$ is surrounded by oxygen atoms at distances similar to those on the oxide phase. The peak at 2.95 Å is attributed to Zn-Zn contributions in ZnO. The zinc exchanged zeolites did not exhibit such a contribution indicating that the concentration of ZnO nano-particles is below the detection limits in the exchanged zeolites. Thus, we conclude in agreement with the other characterizations that the zinc atoms are exchanged at isolated ion exchange positions. The peak at 2.23 Å corresponds to the Zn-Zn contribution. Both zinc exchanged zeolites did not contain a peak at this distance indicating that zinc metal (formed by thermal treatment) is not present in the zeolite. Activated Zn/H-BEA 0.08 Zn/Al exhibited a peak at a distance of 2.45 Å, which was not present at higher zinc loading or before activation and was located between the Zn-Zn contributions in metal (2.23 Å) and oxide (2.95 Å). This peak most probably corresponds to zinc oxygen neighbors in the zeolite formed at a low zinc ion exchange degree. This indicates that (i) samples with low ion exchange degrees are better defined than those with higher zinc contents and (ii) that zinc is

incorporated on specific sites. The observation that the peak at 2.45 Å is not present in the hydrated sample can be explained by unspecific adsorption of water which does not lead to a specific zinc oxygen distance.

The analysis of the EXAFS using phase-shift and amplitude functions calculated by FEFF are summarized in Table 5.

**Table 5** Number and distances of oxygen nearest neighbors in zinc exchanged BEA zeolites

| Sample | Zn/Al | Sample treatment | $N_{Zn-O}$[a] | $r_{Zn-O}$ (Å) | $\Delta\sigma^2$ (Å$^2$) | $E_0$ (eV) |
|---|---|---|---|---|---|---|
| Zn/H-BEA | 0.08 | Before activation | 3.62 | 2.06 | $3.96*10^{-3}$ | -2.8 |
| | | | 2.53 | 3.36 | $4.30*10^{-3}$ | 4.12 |
| Zn/H-BEA | 0.08 | After activation[b] | 4.28 | 1.96 | $1.7*10^{-2}$ | -3.6 |
| | | | 1.75 | 3.00 | $3.90*10^{-2}$ | 8.8 |
| Zn/H-BEA | 0.53 | After activation | 2.56 | 1.96 | $2.80*10^{-3}$ | -2.46 |
| | | | 2.08 | 2.60 | $2.80*10^{-3}$ | 8.05 |

[a] Number of nearest oxygen neighbors
[b] RT – 450°C 10°C/min; 450°C 60 min

In dehydrated Zn/H-BEA (0.08 Zn/Al) around four oxygen neighbors ($N_{Zn-O}$ = 4.28) were found at a distance of 1.96 Å and somewhat less than two at 3.00 Å, while in the hydrated sample the number of neighbors in the first coordination sphere decreased and the bond length was widened. Note that the number of second oxygen neighbors increased upon hydration and in parallel to the Zn-O distances. This indicates strong interaction of zinc with framework oxygen in the dehydrated samples, which decreases upon hydration.

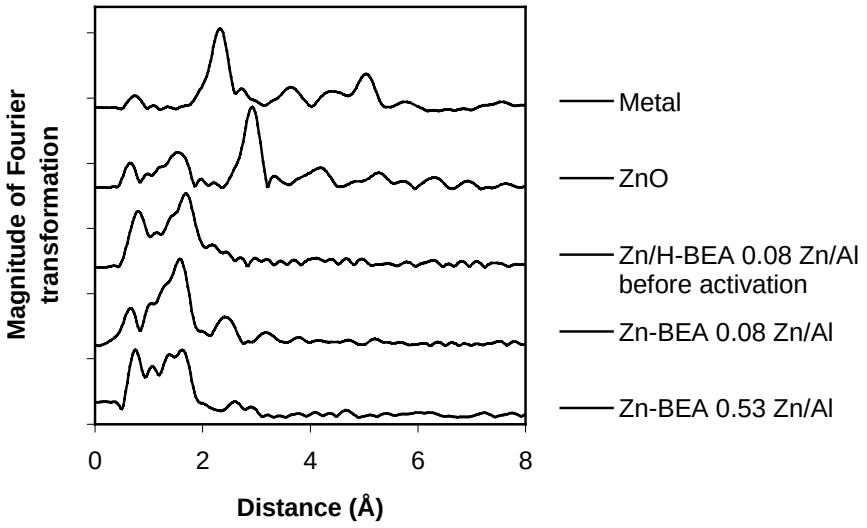


**Fig. 15** EXAFS Zn K-edge radial distribution function for Zn/H-BEA 0.53 and 0.08 Zn/Al after activation, ZnO and zinc metal.

It is possible to exchange $Zn^{2+}$ on 6, 5 and 4 membered ring positions of the BEA structure. These positions can be differentiated by the local environment of the $Zn^{2+}$ atoms evaluated by EXAFS. To firmly assign the location of $Zn^{2+}$ at the different positions, quantum chemical cluster calculations were carried out. The local environment of $Zn^{2+}$ located at the potential ion exchange positions and the relative exchange energies with respect to the energetically most stable position in the 6 membered ring are compiled in Table 6.

**Table 6** Local environment and relative exchange energy of $Zn^{2+}$ at potential ion exchange positions

| Ion exchange position | $r_{Zn-O}$ (Å) | $N_{Zn-O}$ r < 2.2 Å | $N_{Zn-O}$ r > 2.8 Å | E(exch)-E(exch)$_{6-MR}$ [kJ/mol] |
|---|---|---|---|---|
| 6 membered ring | 1.90, 1.91, 1.97, 2.01, 3.43, 3.47 | 4 | 2 | - |
| 5 membered ring | 1.98, 2.03, 2,12, 2.20, 2.83 | 4 | 1 | 9.7 |
| 4 membered ring | 1.94, 1.97, 2.06, 2.07 | 4 | 0 | 33.8 |

The exchange energy of the ion exchange was found to be the lowest for $Zn^{2+}$ at the 6-MR position. For the 5-MR positions only a slightly higher exchange energy was determined, while the 4-MR positions were significantly energetically less favored. This order of substitution sites was identical to those described in ref [150] for $Zn^{2+}$ in Chabazite, the

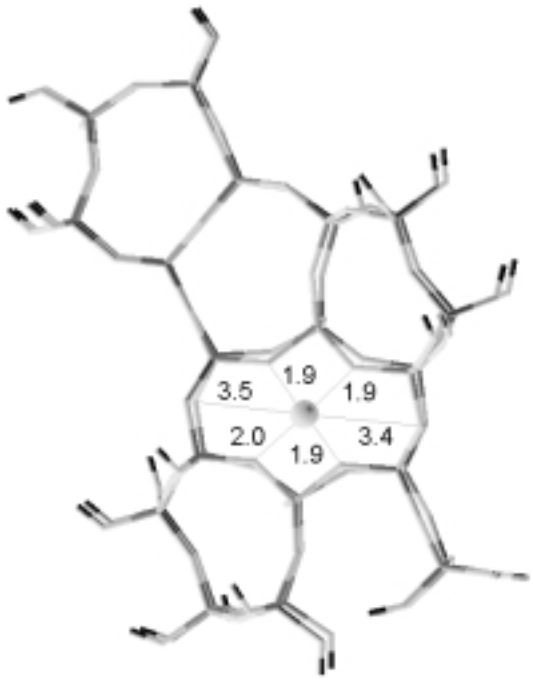


**Fig 16** Preferred location of $Zn^{2+}$ cations in zeolite BEA. Shown is zinc bound to the 6-MR position.

relative energies, however were lower indicating that the BEA framework has a higher flexibility and, therefore, an ion exchange on structurally more constraint positions might also be possible.

The simulation of the local environment of $Zn^{2+}$ at the three potential ion exchange positions resulted in a bimodal distribution of Zn-O distances below 2.2 Å and above 2.8 Å for the 6 and 5 membered ring positions, while for Zn on the 4 membered ring position only Zn-O distances below 2.2 Å were observed. This clearly indicates that the majority of $Zn^{2+}$ in the Zn/H-BEA (0.08 Zn/Al) sample is located at the 6 MR positions, as the analysis of the EXAFS resulted in 4.3 oxygen neighbors at 1.96 Å and 1.75 oxygen neighbors at 3.0 Å. The slightly lower average coordination number for the oxygen atoms with distances above 2.8 Å could indicate that a minor part of the $Zn^{2+}$ cations is located at 5-MR positions

## 3 Discussion

Zeolites in the protonic form contain several types of Brønsted and Lewis acid sites, each acid site being associated with at least one aluminum atom. For zeolite BEA, the following sites are reported: (i) tetrahedral framework aluminum forming Brønsted acid sites, (ii) tricoordinated aluminum exhibiting Lewis acid properties (iii) octahedral coordinated aluminum and (iv) extra framework aluminum [58], [59], [65], [67], [68], [80].

According to the aluminum contents measured by AAS the maximum possible acid site concentration for the H-BEA used was 1.36 mmol/g. However, gaseous ammonia adsorption/desorption experiments led to a total acid site concentration of the parent H-BEA of 0.46 mmol/g. The difference suggests that the activated material is far from being ideal. Note that in this case the Brønsted acid site concentration for the parent H-BEA was even lower (0.14 mmol/g). Two types of Brønsted acid sites, isolated (3612 $cm^{-1}$) and hydrogen bonded (3750 – 3200 $cm^{-1}$) exist in H-BEA zeolite as concluded from IR spectroscopy. IR spectroscopy of adsorbed ammonia indicated that $NH_3$ adsorbs preferentially on the unperturbed Brønsted acid sites. Thus, the Brønsted acid site concentration of 0.14 mmol/g (derived by $NH_3$ TPD) relates to the concentration of unperturbed free Brønsted acid sites. Upon liquid ammonium exchange the Brønsted acid site density increased to 0.87 mmol/g. This indicates that in a dehydrated H-BEA zeolite Brønsted acid sites are distorted in a way that they are not accessible for gaseous ammonia. Upon liquid ammonium exchange this distortion is reversed and these sites show their acidic character.

The concentration of $Al^{3+}$ Lewis acid sites in H-BEA was determined by IR spectroscopy of adsorbed pyridine (0.19 mmol/g) and acetonitrile-$d_3$ (0.27 mmol/g). The use

of a higher outgassing temperature in case of pyridine (100°C *vs*. 35°C) led to partial desorption of pyridine from weak Lewis acid sites. This suggestion is supported by IR spectroscopy of adsorbed acetonitrile-$d_3$ employing 100°C as adsorption temperature. In this case 0.21 mmol/g $Al^{3+}$ Lewis acid sites were found. The mechanism of formation and the nature of aluminum Lewis acid sites in H-BEA is still under discussion. Clearfield et. al. [58] showed that $Al^{3+}$ Lewis acid sites are formed by dehydroxylation of tetrahedral framework aluminum sites above 500°C. The authors postulated that one $Al^{3+}$ Lewis site is formed by destruction of two Brønsted acid sites in close vicinity. A similar mechanism was described by Wichterlová et al. [58], [68]. Both authors concluded that especially perturbed Brønsted acid sites tend to dehydroxylate. Timken et al. [67] showed that the reaction is, in principle, reversible. When in contact with trace amounts of water, tricoordinated aluminum sites convert to octahedral aluminum sites. Upon aqueous ion exchange with cations, such as $NH_4^+$, tricoordinated aluminum sites convert to tetrahedral aluminum framework sites. This agrees well with the increase of Brønsted acid sites observed in the liquid ammonium exchanged sample.

This sequence was further confirmed for the H-BEA zeolite used in this study. Partially hydrated H-BEA contained some octahedral aluminum as determined by $^{27}Al$ NMR. In agreement with the observations of Timken et al., these had probably formed from tricoordinated aluminum framework sites upon hydration [67]. In this case, the octahedral

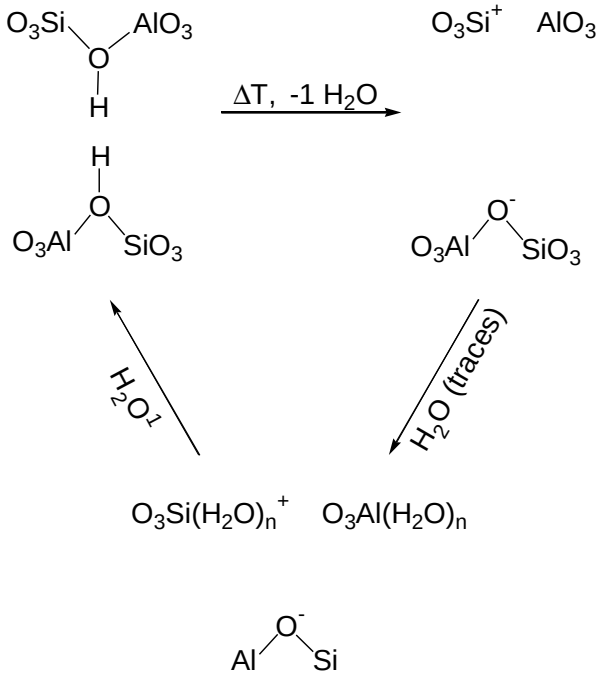


**Fig.17** Conversion of aluminium sites as proposed for zeolite BEA; [1] under ion exchange conditions, $0 \leq n \leq 4$

aluminum sites observed by NMR in the hydrated sample (roughly 20 % of the total aluminum contents) corresponds to the $Al^{3+}$ Lewis acid sites found by IR spectroscopy of adsorbed acetonitrile-$d_3$ in the dehydrated sample (19.8 % of the total aluminum content). From these data we conclude that in a dehydrated H-BEA zeolite 0.14 mmol/g isolated and free Brønsted acid sites are present. 0.53 mmol/g Brønsted sites are distorted by the dihydroxylation mechanism described above and thus only the $Al^{3+}$ Lewis acid sites (0.27 mmol/g) are accessible for gaseous ammonia. By liquid ammonia exchange 0.87 mmol/g Brønsted acid sites were found. Thus, 0.2 mmol/g Brønsted sites must be present, which are not accessible for gaseous ammonia, if dehydrated. These are tentatively attributed to Brønsted sites covered by one extra framework aluminum. In liquid phase this species can be ion-exchanged by ammonium ions. The remaining aluminum content of 0.3 mmol/g is attributed to extra framework aluminum located on the outer surface.

In principle, one $Zn^{2+}$ cation can bind (i) to two tetrahedral aluminum sites ($Zn/Al_{max} \leq 0.50$) requiring close neighborhood of the aluminum sites, (ii) as $Zn(OH)^+$ involving one tetrahedral aluminum site ($Zn/Al_{max} \leq 1.00$) or (iii) as neutral ZnO located at the pore wall or the outer surface (Zn/Al not limited). The formation of $Zn(OH)^+$ species was only reported for hydrated zeolites [69]. Recently, Iglesia et. al. showed by X-ray adsorption on zinc exchanged ZSM-5 that $Zn(OH)^+$ species are not stable and dehydrate upon thermal treatment [48]. Condensation with acidic OH groups leads to the formation of $Zn^{2+}$ cations interacting with two tetrahedral aluminums. Nevertheless, upon ion exchange conditions the formation of $Zn(OH)^+$ species exchanged on isolated Brønsted sites is possible. Similarly, van Santen et al. concluded from DFT studies that $Zn^{2+}$ cations in dehydrated chabazite are most stabilized on positions, where at least two tetrahedral aluminum atoms are in vicinity [150]. Therefore, we postulate that pairs of tetrahedral framework aluminum atoms, which are close enough to balance the divalent charge of the zinc cation, are preferentially exchanged. If this is not possible due to sterical constrains, two zinc cations will bind to one Brønsted acid site each. The divalent charge is then balanced by an oxygen atom bridging the two zinc cations (iv). In this case, a specific geometry of the ion exchange positions is required and the

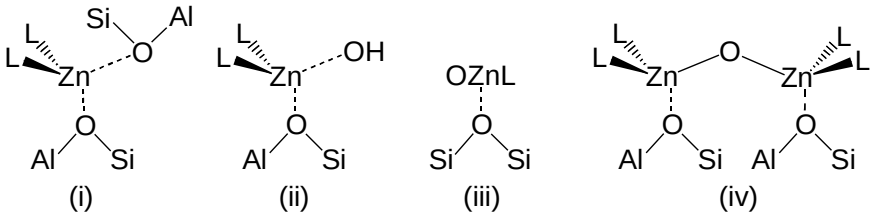


**Fig. 18** Possible Zn-sites in Zn/H-BEA.

distance between the two framework aluminums may not exceed 1.2 nm.

By stepwise zinc ion exchange, a series of Zn/H-BEA zeolites with zinc loadings between 0.02 Zn/Al (0.03 mmol/g) and 0.77 $Zn/Al_{max}$ (0.86 mmol/g) was prepared. The IR spectra of all zinc exchanged BEA zeolites showed bands assigned to unperturbed and perturbed Brønsted acid sites. The concentration of unperturbed Brønsted acid sites was determined by IR spectroscopy of adsorbed acetonitrile-$d_3$, pyridine and by TPD of ammonia and iso-propylamine. With all spectroscopic methods, an initial decrease in the concentration of unperturbed Brønsted acid sites (from 0.14 to ca. 0.10 mmol/g) was found relative to the parent H-BEA zeolite. Subsequently, the concentration remained approximately constant over the whole range of zinc exchange ($\geq$ 0.02 Zn/Al). This indicates that zinc is not exchanged on isolated Brønsted acid sites and that the initial decrease is caused by destruction of Brønsted acid sites upon zinc exchange and subsequent calcination. This hypothesis is supported by IR spectroscopy of $CD_3CN$ showing that in the decreasing amount of $Al^{3+}$ Lewis sites the concentration of zinc is reflected. The broad IR absorption band (3750 – 3200 $cm^{-1}$) remained unchanged after sorption of basic probe molecules such as $NH_3$, $CD_3CN$ or pyridine. This indicates that these sites exhibit no significant acidity and are therefore not able to be exchanged by zinc cations. Upon zinc exchange no significant changes in the intensity of this absorption band was observed. Nevertheless, the quantification appeared to be difficult as H-bonding interactions are leading to a broadening and increase in intensity of this IR-band [75].

The number of $Al^{3+}$ Lewis acid sites decreased linearly (0.22 – 0 mmol/g) with increasing zinc contents as indicated by the IR spectra of adsorbed acetonitrile-$d_3$. In parallel, the number of $Zn^{2+}$ Lewis acid sites increased linearly. This indicates a direct correlation between zinc incorporation and decrease in $Al^{3+}$ Lewis sites. We conclude that $Zn^{2+}$ ion exchange occurs preferentially on neighboring aluminum pairs. Upon $Zn^{2+}$ exchange, the neighboring $Al^{3+}$ pairs are stabilized as tetrahedral framework aluminum. During the activation procedure, remaining free aluminum sites in vicinity are dehydroxylated. This conclusion is in agreement with the constant concentration of unperturbed Brønsted acid sites. Also, the total number of Lewis acid sites (containing $Zn^{2+}$ and $Al^{3+}$ Lewis acid sites) remained constant in the range $0 \leq Zn/Al \leq 0.26$ as seen by IR spectroscopy of adsorbed pyridine (450°C). A constant level of Lewis acid sites is expected, if one $Zn^{2+}$ cation formally replaces one $Al^{3+}$ Lewis site. This is in agreement with results reported by Wichterlová et al. for incorporation of $Co^{2+}$ in BEA zeolites (0-0.25 Co/Al) [68].

The subtle details of the different $Zn^{2+}$ ion-exchanged species cannot be clearly distinguished by sorption of probe molecules such as acetonitrile-$d_3$ or pyridine. However, these zinc species can be identified by differences in their chemical behavior during temperature programmed desorption of iso-propylamine. Two different zinc sites were identified by analysis of the propene desorption features. The high temperature peak (476°C) showed a linear increase with the zinc loading from 0 - 0.15 Zn/Al, which agrees well with zinc incorporated on aluminum pairs in vicinity. The second zinc site (corresponding to the desorption maximum at 394°C) is present in this range of zinc loading in small concentrations. Between 0.15 and 0.26 Zn/Al, the concentration increases indicating incorporation of zinc cations on pairs of nearby framework aluminum. The distance between these Brønsted acid sites is probably too far to balance the charge of a divalent cation. Thus, above 0.15 Zn/Al ion exchange can only occur if zinc is additionally coordinated to an oxygen bridging between two zinc species. Note, that zinc exchange on nearby framework aluminum sites induces geometric constraints because of the formation of stable Al-O-Zn-O-Al oxygen bridges. Therefore, the concentration of oxygen bridged zinc species is limited. In the range of $0 \leq Zn/Al \leq 0.26$, the concentration of aluminum pairs decreased in parallel with the zinc incorporation as shown by IR spectroscopy of adsorbed acetonitrile-$d_3$.

At 0.26 Zn/Al all aluminum pairs in the present sample are exchanged by $Zn^{2+}$ cations. Further $Zn^{2+}$exchange can only on isolated Brønsted acid sites. Upon ion exchange conditions this is possible by the formation of $Zn(OH)^+$ species. The thermal stability of these $Zn(OH)^+$ species that exchanges at these sites is, however, low leading to migration of ZnO species presumably to the outside of the zeolite crystal and the re-establishing of the isolated Brønsted acidic hydroxyl group. Note that this is in perfect agreement with the inability to exchange the hydroxyl groups characterized by the unperturbed OH band at 3610 $cm^{-1}$. Similarly excess ion exchange and subsequent clustering may also occur on SiOH groups of the material. This situation is characterized by the linear increase in Lewis acid sites above 0.26 Zn/Al as, e.g., observed in IR spectroscopy of adsorbed pyridine (450°C). Additionally, the formation of a third zinc phase above 0.26 Zn/Al is indicated by total zinc contents determined by AAS (total zinc contents) and TPD of iso-propylamine or IR on adsorbed pyridine. At high zinc loading (0.53 Zn/Al) upon TPD and IR around 38 % of the total zinc contents were determined. The TPD desorption of acetonitrile showed, that at high zinc loading (0.53 Zn/Al) three desorption states attributed to zinc sites are present, while at low zinc loading only two of these desorption states were found. The desorption state missing at low zinc loading is probably due to the zinc oxide phase. This agrees well with desorption temperatures observed. The zinc

oxide phase exhibited acetonitrile desorption lower temperature (176°C) than the other zinc species (359 and 456°C). This indicates a lower Lewis acidity of the ZnO phase while zinc exchanged on cation exchange position in the zeolites exhibit higher Lewis acidities. This is supported by catalytic results in hydroamination reactions in which the activity of zinc based solid catalysts is attributed to the Lewis acid strength [50]. In contrast to zinc exchanged BEA zeolites ZnO was catalytically inactive.

The preferred ion exchange positions of $Zn^{2+}$ were identified by combination of X-ray absorption spectroscopy and structure simulation. For Zn/H-BEA (0.08 Zn/Al) four average Zn-O distances around of 2 Å and two around 3.0 Å were observed. The results of the quantum chemical cluster calculation revealed that this is a clear indication for the location of $Zn^{2+}$ at 6 membered oxygen ring positions facing the large 12 rings. In addition this position was found to be the energetically most stable ion exchange position for $Zn^{2+}$ within the BEA structure. Similarly, van Santen et al. found for Chabazite that $Zn^{2+}$ is best stabilized, if coordinated a six ring on that site which faces a larger 8 ring (Zn-O distances 2.01-2.08 Å) [150]. Similar ion exchange positions were found previously by Vitale et. al. for $Ca^{2+}$ in LSX and Guliants et. al. for $Cu^{2+}$ in mordenite [150], [81], [82].

## 4. Conclusion

By adsorption studies using different probe molecules we were able to assign differences in Lewis acidity in zinc exchanged BEA zeolites. These are caused by incorporation of zinc on different cation exchange positions. Close aluminum pairs, i.e., two tetrahedral framework aluminums in vicinity, were identified to be the preferential sites for zinc exchange. Close neighborhood of two negatively charged oxygen atoms is necessary for balancing the charge of a divalent cation, leading to an energetically favorable local environment around $Zn^{2+}$. In H-BEA the corresponding Brønsted acid sites are thermally unstable. Upon thermal treatment, the high local positive charge on hydrogen is reduced by rearrangement of the framework and formation of Lewis acid sites. The coordination of a cation increases the stability of close aluminum pairs. Thus, these sites are only present in ion exchanged BEA. The combination of EXAFS and structure simulation indicate that (i) the zinc cations preferentially coordinate to six membered oxygen rings and (ii) the aluminum pairs are preferentially located in six membered rings. These zinc sites lead a high catalytic activity of the material in reactions, such as hydroamination [50]. Thus, it seems most likely that zinc is readily accessible and, therefore, located on that side of the six membered rings which faces in the main channel system.

When all close aluminum pairs are covered, the concentration of a second zinc species increases sharply, indicating that this site is the next preferred zinc exchange location. Very high zinc concentrations do not lead to a further increase of this zinc species, indicating a limited concentration of this kind of aluminum sites present in zeolite BEA. The second zinc species is made of two zinc cations exchanged on nearby aluminum sites balanced by the divalent charge by an oxygen bridge. At very high zinc loading a third site, probably neutral ZnO on the outer surface, is formed. This third zinc site does not correspond to catalytic activity of Zn/H-BEA in hydroamination reactions [50].

Thus, zeolite BEA has two preferential ion exchange locations for a divalent cation. Both are not related with unperturbed Brønsted acid sites which are associated with framework aluminum. This specialty of zeolite BEA opens the possibility of designing a material with Lewis and Brønsted acidity. This type of bi-functional material could be of great potential for many acid catalyzed reactions.

# III Heterogeneous catalysts for hydroamination reactions

## 1. Introduction

Hydroamination of alkenes and alkynes, which constitutes the formal addition of a N-H bond across a carbon-carbon multiple bond, is a transformation of fundamental simplicity and would appear to offer the most attractive route to numerous classes of nitrogen containing molecules such as alkylated amines, enamines or imines. In principle, the addition of nucleophiles to a π-system may lead to two different products. Addition of the nucleophile to the sterically more hindered carbon atom gives the Markownikow product. Addition to the sterically less hindered carbon atom yields the *anti*-Markownikow product. The direct addition of nucleophiles H-$NR_2$ to activated alkenes (activated by, e.g., a keto, ester, nitrile, sulfoxide or nitro function) usually leads to *anti*-Markownikow products [83], [84]. On the other hand aliphatic olefins as well as most aromatic olefins are often aminated to give the Markownikow product.

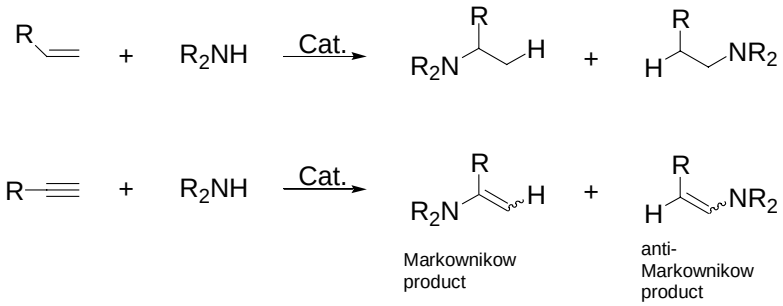


In the latter case, the rate of amine addition is dependent on the steric nature of the metal alkyl intermediate formed. The nucleophilic nitrogen reacts in such a way that the least hindered metal alkyl intermediate is formed (Markownikow addition) [3].

## 2. Parent materials

Zeolites BEA, MCM-22, MOR and Y in their acidic form were used as parent materials. In case of BEA zeolite (Süd Chemie) XRD analysis and the IR spectra of the skeletal vibrations indicated a well developed and highly crystalline BEA structure and phases other than BEA were not present in the parent material. The diameter of the crystals was 0.1 - 0.3 µm. The Si/Al ratio was determined to 11.6 by AAS spectroscopy. Solid state $^{27}$Al-NMR measurements confirmed the presence of tetrahedral and octahedral coordinated aluminum in H-BEA as reported in literature [97]. The BET surface area was 537 $m^2/g$, which is in agreement with the literature [85]. Thus, it can be concluded that the parent H-BEA zeolite is

a pure and well-defined material. The characterization of the other parent zeolites is described elsewhere [86], [87], [88] and confirms that these materials are also highly crystalline and pure zeolites.

Transition metal based zeolite catalysts were prepared by ion exchange. Except for $Cu^{+}$, $Rh^{+}$ and $La^{3+}$ all exchanges were performed by suspending the parent zeolite in an aqueous solution of metal salt. The ion exchange involving copper (I) and rhodium (I) was carried out in $CH_3CN$ using dehydrated H-BEA zeolite and an inert atmosphere, as these metals in the oxidation states stated are susceptible to oxidation and / or disproportionation. The metal loadings obtained were 0.03 - 1.6 mmol $M^{n+}$ per gram zeolite as determined by AAS (appendix Table 2). The BEA zeolite was ion exchanged with $Rh^{+}$, $Ni^{2+}$, $Pd^{2+}$, $Pt^{2+}$, $Cu^{+}$, $Zn^{2+}$ and $La^{3+}$, while in case of MCM-22, MOR and Y zeolites only $Zn^{2+}$ exchange was performed. A series of zinc exchanged BEA zeolites was prepared varying in the zinc loading. These zeolites were further characterized by nitrogen adsorption and IR spectroscopy. The nitrogen adsorption isotherms followed a typical type I adsorption isotherm, thus, providing evidence for the microporosity of the materials. It was expected, that by stepwise zinc incorporation in the zeolite pores the micropore area decreases. However, this is not the case and the micropore area remained approximately constant (appendix Table 2). This is related to the small amount of zinc incorporated in the zeolite pores [106] (up to 1.5 zinc atoms per unit cell) which does not effect the micropore area significantly. The IR spectra in the range of the skeletal vibrations indicated no changes upon zinc exchange compared to the parent material. Thus, it can be concluded that the structure of the BEA zeolites did not change upon zinc exchange.

## 3. Activity of zinc exchanged zeolite catalysts

The zinc ion exchanged zeolites (Bea, MCM-22, Mor and Y) were tested as catalysts in the cyclization of 6-aminohex-1-yne (6AHI) and 3-aminopropylvinylether (3APE). The product formation with time is compiled in Fig. 1 and 2, respectively. In case of cyclization of 6AHI, $ZnO/SiO_2$ displayed a higher activity than Zn/H-MCM-22, Zn/H-Mor or Zn/H-Y. This agrees well with patents indicating that zinc silicates are good catalysts for the gas phase reaction between alkynes and amines to give enamines (in case of primary amines) and imines (in case of secondary amines) [9]. In contrast, in the cyclization of 3APE zinc exchanged MCM-22 zeolite displayed a slightly higher activity than $ZnO/SiO_2$. The conversion rates determined for Zn/H-MCM-22, $ZnO/SiO_2$, Zn/H-Mor and Zn/H-Y are very similar. All of these catalysts show a very low activity. It is apparent that in both reactions Zn/H-BEA

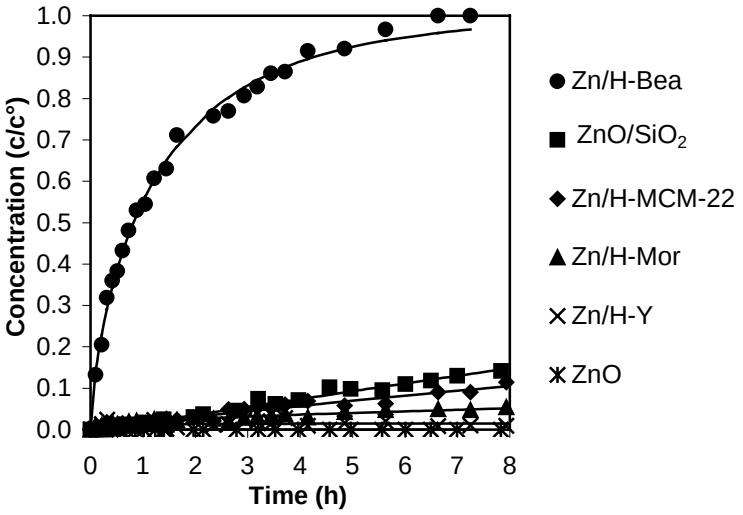


**Fig 1.** Heterogeneous zinc catalysts in the cyclization of 6AHI.

(0.40 Zn/Al) exhibited an exceptional activity, which was at least five times higher than of the other materials. This indicates that the high activity of zeolite BEA results either from structural properties (*via* an increased adsorption constant) or the special location / environment of zinc ions in the pore system. For BEA zeolite it is known that the outer surface exhibits acidic properties [89]. This enables ready adsorption of basic molecules on the outer surface and probably increases their concentration in the zeolite pores. Additionally, it is known that the lattice of BEA zeolite is especially flexible [90]. Therefore, zinc is highly stabilized on specific cation exchange positions. These are located in the 12 ring channels of the BEA zeolite and highly accessible for reactant. These properties lead to the especially high activity of the BEA zeolite. The low activity of the Zn/H-Y zeolite is related to the high zinc contents in the latter. For zinc exchanged BEA zeolites it was shown that high zinc loadings lead to the formation of an additional catalytically inactive ZnO phase. Probably, in Zn/H-Y a large proportion of the zinc cations is present as ZnO, leading to the low average conversion rate per zinc cation observed for this material. In MOR zeolites Brønsted sites can be differentiated by their location in different zeolite channels. One is assigned to bridging Brønsted acid sites located in the main channels and the other to bridging Brønsted acid sites in the side channels of mordenite [91], [92]. The latter Brønsted sites are not as easily accessed by probe molecules with a kinetic diameter > 0.26 nm as those in the main channels [93]. It is reported that approximately 40 % of the acid sites are located in the main channels [94], [95] and accessible for absorption of *n*-alkanes. In case of Ni/H-MOR, which had been prepared by ion exchange in the liquid phase, it was found that at an ion exchange degree of 83 % all nickel species are located in the side channels [91]. With the Zn/H-MOR material studied, the degree of ion exchange was 81 % and it is most likely that, similar to the nickel

based material, these are located in the side channels of the mordenite structure. If located in the side channels zinc is not accessible for reactants such as 6AHI or 3APE. This explains the low catalytic activity observed for the Zn/H-MOR. In order to confirm that ZnO formed during the calcination process was not the source of activity, ZnO was tested in the cyclization reactions. In contrast to the zinc ion exchanged zeolites ZnO did not show catalytic activity. The complete lack of catalytic activity observed for ZnO is attributed to the nature of this material. This is in agreement with the observation that the addition of bases impedes hydroamination reactions [108]. Employing $ZnO/SiO_2$ as catalyst lower reaction rates were found compared to Zn/H-BEA. This is attributed to the Lewis acid strength decreasing in the sequence Zn/H-BEA > $ZnO/SiO_2$ > ZnO.

To ensure that the high activity of the Zn/H-BEA zeolite is not related to zinc cations leached into the toluene solution, the zinc contents of Zn/H-BEA (0.53 Zn/Al) was re-determined after the reaction. No change in the zinc concentration of the material was found, indicating that, during catalysis, zinc remains in the zeolite pores.

In contrast to the cyclization of 6AHI it was not possible to obtain complete conversion for 3APE. In all catalytic mixtures the catalyst was deactivated after around 4 h, which is probably related to traces of oxygen in the reaction mixture.

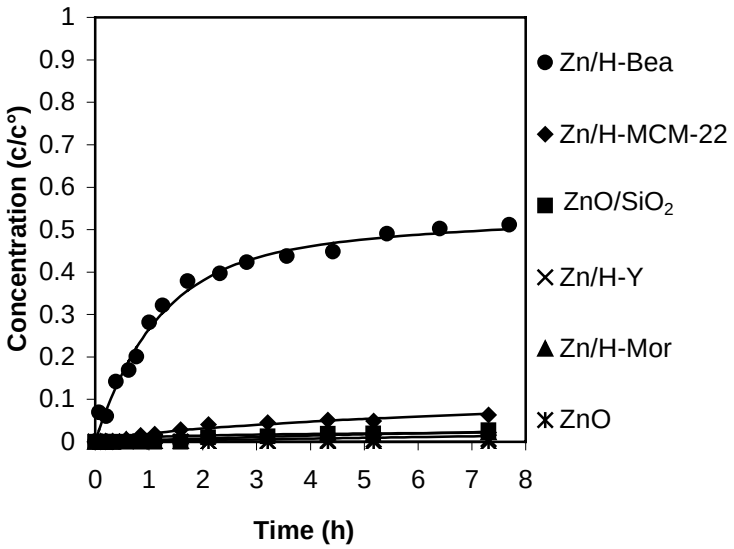


**Fig. 2** Heterogeneous zinc catalysts in the cyclization of 3APE.

## 4. Product selectivity of hydroamination reactions

In principle, for the cyclization of 6-aminohex-1-yne (6AHI) and 3-aminopropylvinylether (3APE) the formation of a 6 - or 7 - membered ring system is possible. Former corresponds to the generally preferred Markownikow addition of the amine to the CC multiple bond, whereas latter is an *anti*-Markownikow addition.

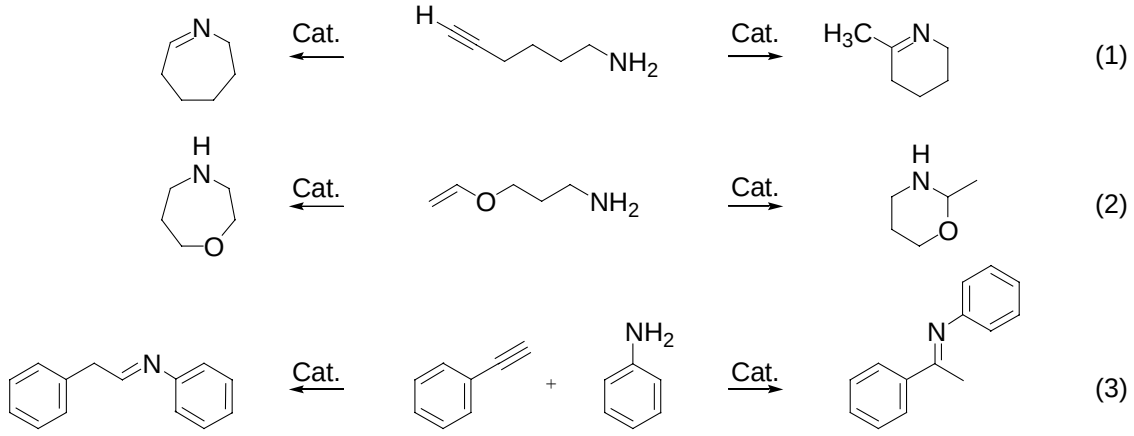


Testing different catalysts for the cyclization of 6AHI and 3APE, only the products with 6- membered rings were formed, i. e., 2-methyl-1,2-dehydropiperidine (2MDP) and the N,O-acetal tetrahydro-2-methyl-1,3-oxazine, respectively. The high regio-selectivity of the reactions is also related to the fact that the transition state for the formation of a 6 - membered ring is energetically favored. Additionally, the ring tension in a 6 - membered ring is slightly smaller than in a 7 – membered ring [96]. Therefore, the formation of a 6 - membered ring is energetically favored relative to the formation of a 7 - membered ring. In principle, the hydroamination product for cyclization of 6AHI is the enamine 2-methylenepiperidine. However, this is not observed as product because of *in situ* isomerization to the more stable imine product 2MDP. In case of cyclization of 3APE, the mesomeric effect of the vinylether oxygen leads to an increase in the electron density mainly on the β carbon atom of the π bond. In parallel, the inductive effect of the vinylether oxygen lowers the electron density on the α-carbon atom. Both effects activate the α-carbon atom for a nucleophilic attack. Thus, the electronic effect can also explain the preferential formation of the 6 - membered ring.

The reactivity of double bonds in hydroamination reactions is generally lower in comparison to triple bonds [3]. Therefore, in cyclization of 3APE lower reaction rates are expected. Indeed, the reaction rates determined for the cyclization of 3APE were around half of those for 6AHI. Also for the intermolecular hydroamination reaction between phenylacetylene and aniline a Markownikow type addition was observed. This reaction is

preferred as it leads to the sterically least hindered metal alkyl intermediate [105]. In case of Markownikow addition the product is stabilized by a mesomeric system connecting both phenyl rings, whereas the product formed by *anti* Markownikow addition is not. Therefore, thermodynamically the formation of the former product is favored. According to the Hammond postulate this often correlates with a lower activation energy.

## 5. Initial activity of H-BEA

The parent H-BEA zeolite had a non-negligible activity in the cyclization of 6AHI and 3APE (Fig. 3, 4). Thus, more detailed studies were performed on the cyclization of 6AHI in order to explore if this is related to Brønsted or Lewis acid sites in the solid material. Reflux in toluene did not lead to conversion of 6AHI. The same result was obtained for an acidic toluene solution ($CF_3SO_3H$, $3.5 \times 10^{-3}$ M). Thus, the initial activity of H-BEA is not related to Brønsted acid catalysis. Sodium exchanged BEA zeolite displayed exactly the same catalytic activity as H-BEA zeolite (Fig. 3). This indicates that during both experiments similar active species were present. These are probably based on Lewis acidic aluminum cations being present in both samples. For H-BEA zeolite no other catalytically active Lewis acid site can be present. To support this hypothesis Zn/H-BEA (0.53 Zn/Al, 103 mg) dispersed in toluene (150 $cm^3$) was heated to reflux for 24 h, separated carefully from the hot solution by centrifugation and analyzed by AAS. While the zinc content remained constant, the aluminum content decreased from 1.24 to 1.04 mmol/g indicating partial extraction of aluminum into the

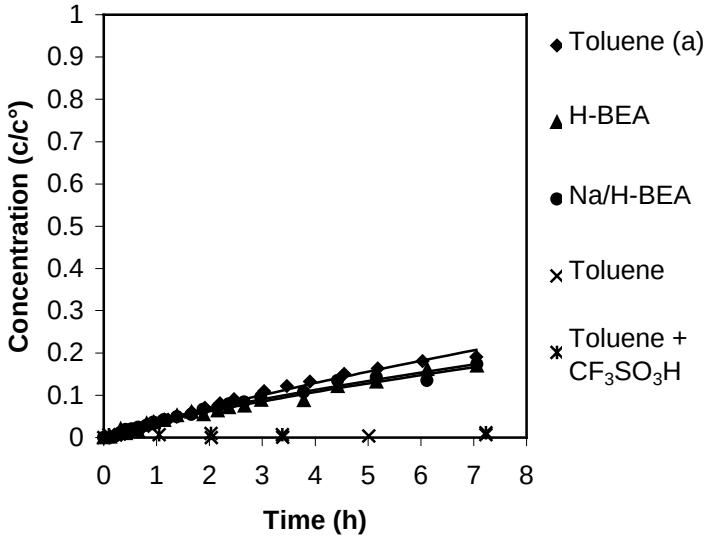


**Fig. 3** Activities of H-BEA zeolite in the conversion of 6AHI; in comparison to pure toluene, acidic toluene, reused toluene (a: see text) and Na/H-BEA.

toluene solution. The remaining toluene was used in the cyclization of 6AHI. In this case, a similar catalytic activity was observed as for activated H-BEA or Na/H-BEA zeolite. This indicates that Lewis acidic $Al^{3+}$ species extracted from the zeolite are responsible for the initial activity observed for H-BEA and Na/H-BEA.

In the cyclization of 3APE the initial activity of the parent H-BEA zeolite (13.6 mmol/(g×h)) was high relative to 6AHI (1.7 mmol/(g×h)). Also in this case, $Al^{3+}$ ions leached in the toluene solution are responsible for the activity of the material. $Al^{3+}$ Lewis sites generally exhibit a strong preference to coordinate oxygen ligands, while interactions to nitrogen ligands are comparably weak [97]. Probably, the vinylether group coordinates *via* the oxygen atom to the $Al^{3+}$ Lewis sites, which might directly or indirectly activate the double bond for a nucleophilic attack of the amine. A direct activation would be the result of a reduced electron density on the double bond caused by coordination of the oxygen atom to the $Al^{3+}$ Lewis site. An indirect activation would proceed *via* initial coordination of the oxygen atom on the $Al^{3+}$ Lewis site. This yields a complex in which the unsaturated carbon-carbon double bond is located closely to the catalytically active metal cation. A slight shift of the ligands leads to coordination of the double bond to the metal center and consequently initiates the hydroamination reaction.

The parent H-BEA zeolite also showed a small catalytic activity in the intermolecular hydroamination reaction between phenylacteylene (PAE) and aniline (AIL). However, the observed product concentrations were very low and close to the experimental error.

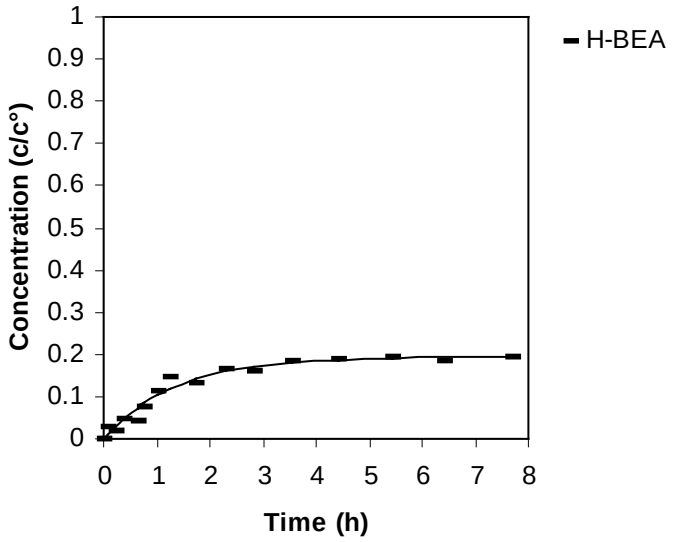


**Fig. 4** Activity of H-BEA zeolite in the conversion of 3APE.

## 6. The activity of transition metal based BEA catalysts

Many homogeneous catalysts for hydroamination reactions are complexes of late transition metals [3]. Corresponding solid materials were prepared based on the metal ions $Cu^{+}$, $Cu^{2+}$, $Rh^{+}$, $Pd^{2+}$, $Pt^{2+}$, $Ni^{2+}$ and $La^{3+}$ and tested for their activity in hydroamination reactions. As the support for the metal cations the zeolite BEA was chosen. Materials with metal loadings between 0.15 – 0.88 mmol $M^{n+}$/g were prepared; the details are summarized in the appendix (Table 2). In case of $Ni^{0}$, $Zn^{2+}$, $Pd^{2+}$, $Pt^{2+}$ and $La^{3+}$ exchanged BEA, the activated (dehydrated) materials were used as catalysts expecting that the metal cations remained in the oxidation states stated. Before use, the $Ni^{2+}$ exchanged zeolites were reduced in hydrogen to obtain a $Ni^{0}$ containing catalyst. The $Cu^{+}$ and $Rh^{+}$ based zeolites were used as obtained, handled in inert atmosphere, because copper (I) and rhodium (I) are susceptible to oxidation and / or disproportionation. The materials were then tested for their catalytic activity in the cyclization of 6AHI and 3APE (Fig. 5, 7).

In the cyclization of 6AHI La/H-BEA, Ni/H-BEA and Pt/H-BEA had an activity that was only slightly higher than that of the parent H-BEA. In contrast, Cu(I)/H-BEA and Rh(I)/H-BEA zeolites showed an even higher activity than Zn/H-BEA (Fig. 4). The activity of Pd/H-BEA was intermediate between the activity of Pt/H-BEA and Zn/H-BEA. The low activity of Pt/H-BEA is probably due to the formation of a stable complex between $Pt^{2+}$ and an organic intermediate, which blocks the catalytic cycle. In homogeneous catalysis a low activity of $Pt^{2+}$ catalysts relative to other similar metal centers, such as $Pd^{2+}$, is frequently observed. Compared to $[PtH(PEt_3)_2]NO_3$ which, employed as homogeneous catalyst (s/c = 100) yielded 29% conversion in 20 hours [98], Pt/H-BEA is more active (s/c = 100, 29%

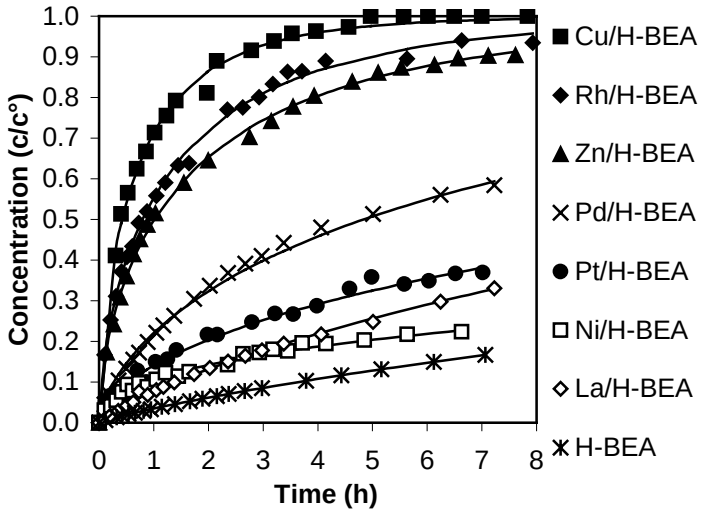


**Fig. 5** Cyclization of 6AHI with transition metal exchanged BEA zeolites.

conversion in 4 hours). In contrast, Ni/H-BEA showed a higher activity than H-BEA, but lower activity than the best homogeneous nickel(0)-catalyst [(Ni(Triphos))$_2$(COD)] (COD = cyclooctadiene). Latter gave 100% conversion in less than 20 hours, although it was susceptible to decomposition. The Ni/H-BEA zeolite had been prepared by aqueous ion exchange from a solution of Ni($CH_3CO_2$)$_2$ (0.03 M). The acid sites were first exchanged with $Ni^{2+}$ cations followed by reduction with hydrogen. It is known that $Ni^0$ sites are not stabilized on a silica surface in the presence of OH groups [99]. In the absence of molecular hydrogen as reducing agent the $Ni^0$ is easily reoxidized to $Ni^{2+}$. The low activity of the Ni/H-BEA can, thus, be related to the formation of $Ni^{2+}$, which did not show catalytic activity in homogeneous catalysis. For $La^{3+}$ exchanged BEA zeolites a strong relation between the activity of the material and the activation temperature was observed. The increase in activation temperature from 200°C to 450°C led to an increase in initial reaction rate from 0.9 to 2.7 mmol/(g×h). La exchanged zeolites are known to be hydrophilic and upon temperature treatment the formation of lanthanum hydroxide species is reported [100]. Activation at 200°C led to an activity similar to H-BEA. Therefore, the $La^{3+}$ cations seem to be catalytically inactive, probably, because water adsorbed on the metal cation disables the coordination of 6AHI. Activation of the La/H-BEA at 400°C led to a three fold higher catalytic activity. The activity is comparable to the nickel catalyst, but the forms of the kinetic curves differ significantly. For La/H-BEA, the initial rate of reaction is high, while the reaction slows down remarkably at longer reaction times. In contrast, for Ni/H-BEA the reaction approximately follows first order kinetics. This indicates that, in case of lanthanum, another mechanism is probably valid and/or deactivation of the catalyst occurs.

In case of copper exchanged BEA zeolites more detailed studies were performed. The main question was whether Cu(I) or Cu(II) is the catalytically active species in the cyclization of 6AHI. Cu(II) exchanged zeolites are known to be unstable upon temperature treatment in inert atmospheres and reduction of Cu(II) to Cu(I) was reported for these systems [101]. A recent paper [102] proposed that the Cu(I) species have their origin in $[Cu^{II}\text{-}OH]^+$ cations, which are charge balanced by one framework aluminum. Thermal treatment initially leads to the formation of $[Cu\text{-}O\text{-}Cu]^{2+}$. At higher temperatures (500°C) the Cu(II) is reduced to Cu(I) in an inert atmosphere or vacuum [101], [103] according to:

$$[Cu\text{-}O\text{-}Cu]^{2+} \rightarrow 2Cu^+ + ½O_2$$

For further study, Cu(II) exchanged BEA zeolites were prepared by aqueous ion exchange from a Cu($CH_3CO_2$)$_2$ solution as described previously. A reference sample containing Cu(I) was prepared employing anhydrous and oxygen free conditions to avoid

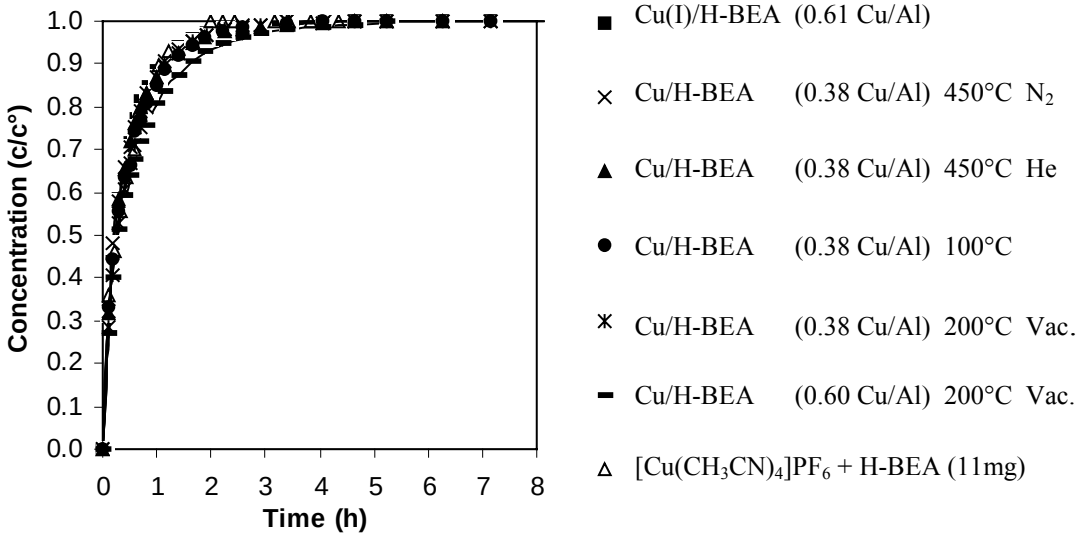


**Fig. 6** Activity of copper exchanged BEA zeolites in the cyclization of 6AHI in dependence of the pretreatment.

oxidation and/or disproportionation of Cu(I). The metal loadings obtained were 0.45 and 0.67 mmol/g for the Cu(II) based and 0.47 mmol/g for the Cu(I) based zeolites. This corresponds to a ratio of 0.38, 0.60 and 0.61 Cu/Al, respectively. The catalytic activities of Cu(II) exchanged BEA zeolites (0.38 and 0.60 Cu/Al) were then examined in dependence on the activation procedure. The materials were activated according to the following procedures:

(i) 450°C, He (100 ml/min)

(ii) 450°C, $N_2$ (100 ml/min)

(iii) 200°C, vacuum ($10^{-1}$ mbar)

(iv) 100°C, air

When tested for the cyclization of 6AHI all materials displayed the same activity independent of the pre-treatment and the metal loading (Fig. 6). Note, that in all experiments the same amount of copper cations was employed. The observation indicates that similar catalytically active sites were present in the same quantity during catalysis. For zinc exchanged BEA zeolites it was shown that the catalytically active zinc species remain exchanged in the zeolites pores. In comparison, it is most likely that this is also valid for copper exchanged BEA and the catalytically active metal centers are located in the zeolite pores.

In addition, an *in situ* exchange experiment was performed. Dehydrated H-BEA zeolite was stirred at reflux temperature in a solution of $[Cu(CH_3CN)_4]PF_6$ in toluene ($3.5 \times 10^{-4}$ M) and the reaction started after 60 min by addition of 6AHI. A complete exchange of copper in the zeolite pores would result in a material with 0.48 mmol $Cu^+$/g. The

same activity as for Cu(I)/H-BEA (0.47 mmol $Cu^+$/g) was observed indicating that similar active sites are present in both materials (Fig.6).

To examine the oxidation state of the copper ions in Cu/H-BEA EXAFS studies were performed. The excitation of Cu 1s electrons causes a sharp increase in X-ray absorption spectra near 8977 eV. The edge energy is dependent on the electron density of the absorber atom. Conceptually, decreasing electron density leads to a shift of the edge to higher energies [104]. Therefore, a comparison of the edge positions of the copper exchanged zeolites with reference compounds (i.e., metallic Cu, $Cu_2O$ and CuO) allows estimating the average charge of the incorporated copper relative to those compounds. Table 1 compares the edge energies of copper exchanged BEA zeolites (0.38 Cu(II)/Al and 0.47 Cu(I)/Al) in dependence of the activation procedure with those of the reference materials.

**Table 1** Absorption edge energies at the Cu K-Edge for Cu/H-BEA and reference materials.

| Sample | Metal contents (mmol/g) | Edge energy (eV) | Oxidation state | Sample treatment |
|---|---|---|---|---|
| Cu | - | 8977.0 | 0 | |
| $Cu_2O$ | - | 8980.9 | +I | |
| CuO | - | 8984.3 | +II | |
| Cu(II)/H-BEA | 0.45 | 8986.8 | +II | Before activation |
| Cu(x)/H-BEA | 0.45 | 9982.1 | | After activation[a] |
| Cu(I)/H-BEA | 0.47 | 8980.6 | +I | No activation[b] |

[a] RT-450°C 10°C/min; 450°C 0.5 h; in $N_2$ (65 ml/min)
[b] handled in inert atmosphere

The edge energies of Cu metal, $Cu_2O$ and CuO were 8977.0, 8980.9 and 8984.3 eV, respectively. Thus, a change of the oxidation state from 0 to +I and +II leads to a shift in edge energy towards higher energies ($\Delta E_{edge}$ = 3.9 eV and 7.3 eV, respectively). For Cu(II) introduced in zeolite BEA an even larger shift in edge energy ($\Delta E_{edge}$ = 9.8 eV) relative to Cu was observed. This indicates that copper, when coordinated to zeolite framework atoms has a lower electron density than in CuO. This might be related to the coordination of water molecules to the Cu cations in the zeolite matrix. A similar difference in edge energy had been observed for Zn(II) introduced in zeolite BEA relative to ZnO ($\Delta E_{edge}$ = 1.2 eV) [106]. Additionally, the oxidation state +II of copper is indicated by the presence of a small peak with maximum at around 8976 eV, due to a (forbidden) 1s→3d electron transition. In case of copper in the oxidation states 0 or +I this transition is not possible, because in these cases the 3d orbital is completely filled in the ground state [121]. However, for Cu(I) a pre edge peak with maximum at 8982 eV is usually observed which results from the 1s →$4p_{x,y}$ electric-dipole allowed transition. Activation of Cu(II) exchanged BEA zeolite in an inert atmosphere

led to a shift in edge energy from 8986.8 to 8982.1 eV ($\Delta E_{edge}$ = - 4.7 eV). Additionally, the peak at 8976 eV decreased in intensity. These observations indicate partial reduction of the copper atoms and a change in the oxidation state from +II to +I. The difference in edge energy of 1.5 eV relative to the Cu(I) exchanged BEA zeolite is probably related to the different sample treatment. Calcination was only performed after Cu(II) ion exchange. Therefore, all coordinating anions are oxygen atoms originating from the zeolite. For Cu(I)/H-BEA it can not be excluded that some of the anions originating from the metal salt or $CH_3CN$ was not removed during drying and remained coordinated to the copper cations. The different edge energy might have resulted from incomplete removal of $CH_3CN$. Therefore, copper had a different coordination sphere in the two samples. In summary, the identical catalytic activities of BEA zeolites ion exchanged with Cu(I) and Cu(II) salts can be explained by the presence of similar Cu(I) species during catalysis.

The $Cu^+$, $Rh^+$, $Zn^{2+}$ and $Pd^{2+}$ based BEA catalysts were also tested in the cyclization of 3APE (Fig. 7). Similar to the parent H-BEA, these catalysts deactivated after approximately 4 h. The rates of reaction were around half of those for 6AHI. Zn/H-BEA had the highest initial catalytic activity followed by Rh(I)/H-BEA, Cu(I)/H-BEA, H-BEA and Pd/H-BEA. This contrasts to the cyclization of 6AHI where the catalytic activity decreased in the following sequence: Cu(I)/H-BEA > Rh(I)/H-BEA > Zn/H-BEA > Pd/H-BEA > H-BEA. The trend in activity observed is an effect of the ether functionality in 3APE and can be explained by the HSAB concept. $Zn^{2+}$ is the harder acid in comparison to $Cu^+$ and $Rh^+$, which are typical soft acids. Amine nitrogen and ether oxygen atoms are both hard bases. Nevertheless, a

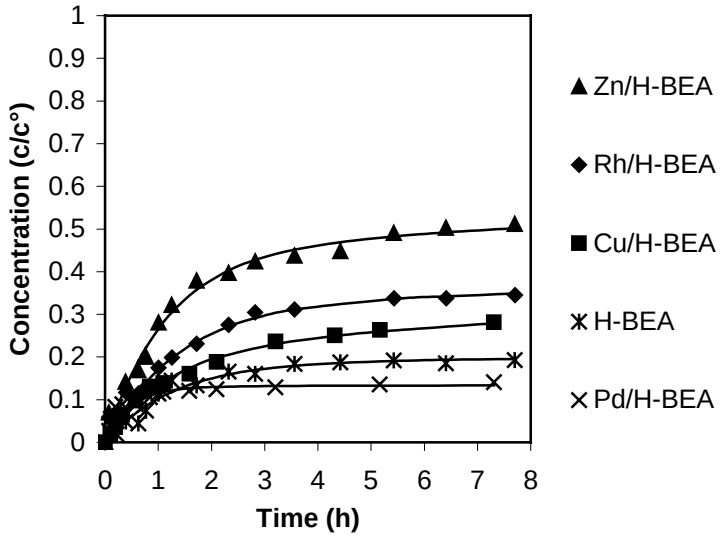


**Fig. 7** Cyclization of 3APE with transition metal exchanged BEA zeolites.

resonance stabilization by a neighboring polarizable double bond decreases the hardness of the ether oxygen [105]. Thus, it is most likely, that the softer Lewis acids $Rh^+$ and $Cu^+$ exhibit stronger interactions to the softer vinylether oxygen than to the harder amine nitrogen in 3APE. This preferred coordination to oxygen probably slows down the overall reaction rate.
Pd/H-BEA (0.32 Pd/Al) had a slightly lower activity in the cyclization of 3APE than the parent H-BEA zeolite. This indicates a very low activity of the palladium in this reaction. Incorporation of palladium in zeolite BEA prevents leaching of $Al^{3+}$ Lewis acid sites, which are responsible for the initial activity of H-BEA.

## 7. Activity of zinc exchanged BEA zeolites

The role of the cation-concentration in zeolite BEA for catalysis was explored for zinc concentrations of up to 0.86 mmol/g (0.77 Zn/Al). The intramolecular and the intermolecular hydroamination reactions were performed using the same amount of zinc exchanged zeolite (10.7 mg). In consequence, the total amount of zinc varied in the reaction mixture. By analysis of the initial reaction rates and correlating them to the zinc loading the catalytic activity of each zinc site in the material can be estimated. In Fig. 8, 10, 12 the formation of the products *versus* time are compiled. For all reactions explored the rate of reaction correlated non-linearly with the zinc concentration. At low zinc loading the activity of catalysts increased, while at higher zinc loadings it remained constant (Fig. 9, 11, 13).

Characterization of the zinc exchanged BEA zeolites showed that, depending on the metal content, up to three different zinc sites are present. Generally, in the range 0 - 0.30 Zn/Al zinc is exchanged on framework aluminum atoms. Within this range of zinc contents two zinc sites were found differing in the location of charge balancing oxygen atoms. The zinc cations are most stabilized on positions in which the divalent charge is directly balanced by two framework oxygen atoms. This requires a close vicinity of two framework aluminum atoms (zinc site A). Additionally, a second ion exchange position was found, which is formed preferentially at ion exchange degrees between 0.15 and 0.30 Zn/Al. In this case, the charge of two divalent zinc cations is balanced by two $AlO_2^-$groups and one oxygen bridging two zinc cations (zinc site B) [106]. Above 0.30 Zn/Al zinc is incorporated as ZnO (zinc site C) [106]. In case of the cyclization of the 6-aminohex-1-yne a linear correlation between the activity and the zinc loading was observed in the range 0 - 0.26 Zn/Al. This correlates with the increasing amount of zinc, which is incorporated in the zeolites as zinc site A and B. This shows that in this range of zinc loading a constant proportion of the zinc cations is available for catalysis. For loadings above 0.26 Zn/Al the activity approached a constant

level indicating that zinc incorporated as ZnO (zinc sites C) is catalytically not active. This is expected, as pure ZnO did not show activity in hydroamination reactions.

In case of the cyclization of 3 APE the initial reaction rates were comparable to 6AHI (Fig. 9, 11). A linear correlation between the activity and the zinc loading was observed in the range 0 - 0.33 Zn/Al. This correlates with the increasing amount of zinc, which is exchanged in the zeolites pores as zinc site A and B. Zinc exchanged on these sites is located in the 12 ring channels of zeolite BEA, where catalytically active sites are most accessible for reactants. For loadings above 0.33 Zn/Al the activity approached a constant level indicating that zinc incorporated in zeolite BEA as ZnO (zinc site C) is catalytically inactive.

The intermolecular reaction was around 100 fold slower compared to the intramolecular reactions (Fig. 12, 13). Nevertheless, also in this case analysis of the initial reaction rates showed the same trend with the zinc loading as observed for cyclization of 3APE. Zinc exchanged in the zeolites pores is catalytically active, while the ZnO phase did not show any catalytic activity.

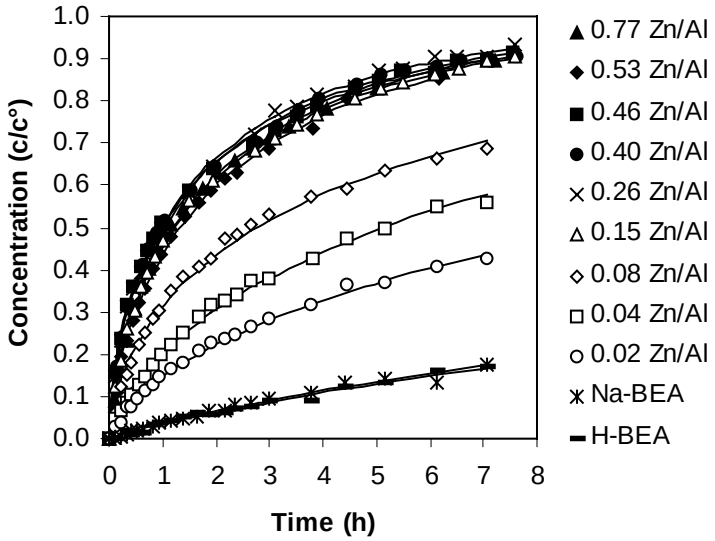


**Fig. 8** Cyclization of 6AHI with Zn/H-BEA catalysts loaded with different amounts of $Zn^{2+}$ cations.

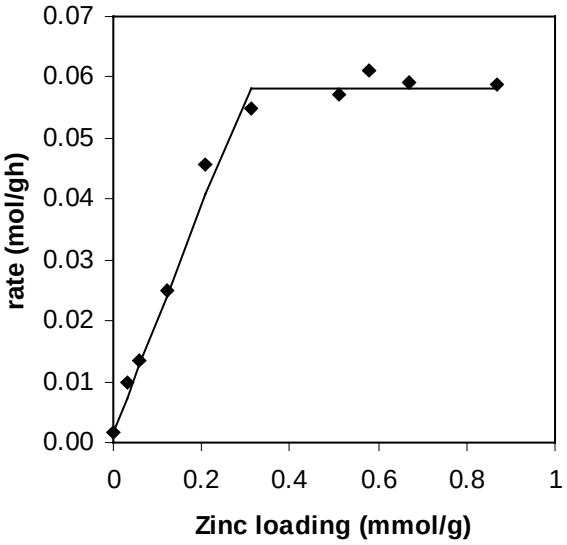


**Fig. 9** Initial rates for the cyclization of 6AHI with zinc exchanged BEA zeolites containing different amounts of $Zn^{2+}$ cations.

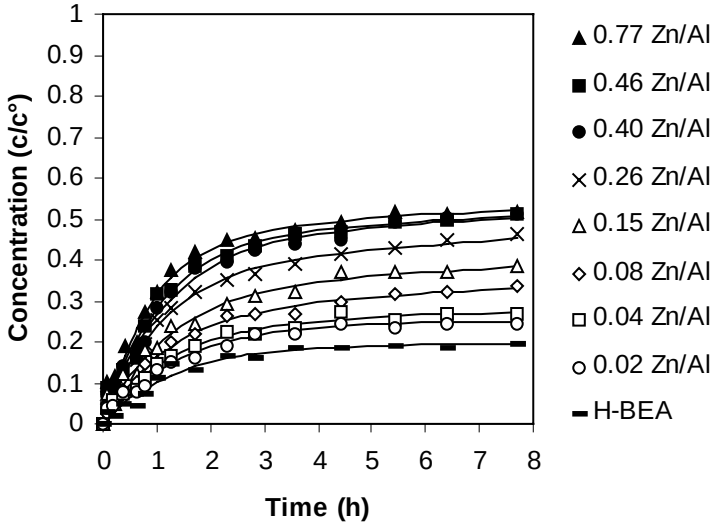


**Fig. 10** Cyclization of 3APE with Zn/H-BEA catalysts loaded with different amounts of $Zn^{2+}$ cations.

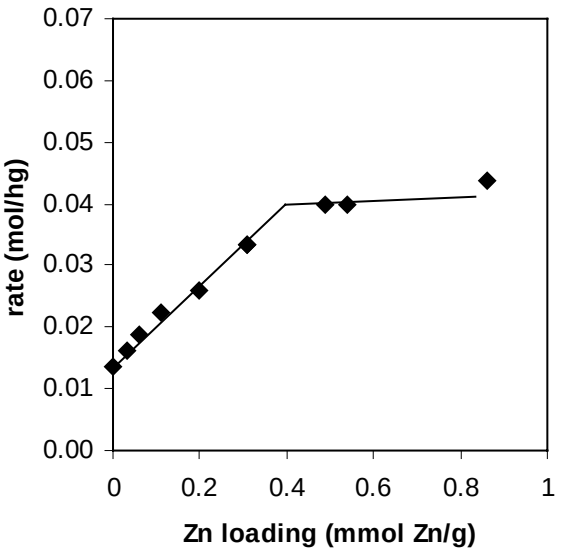


**Fig. 11** Initial rates for the cyclization of 3APE with zinc exchanged BEA zeolites containing different amounts of $Zn^{2+}$ cations.

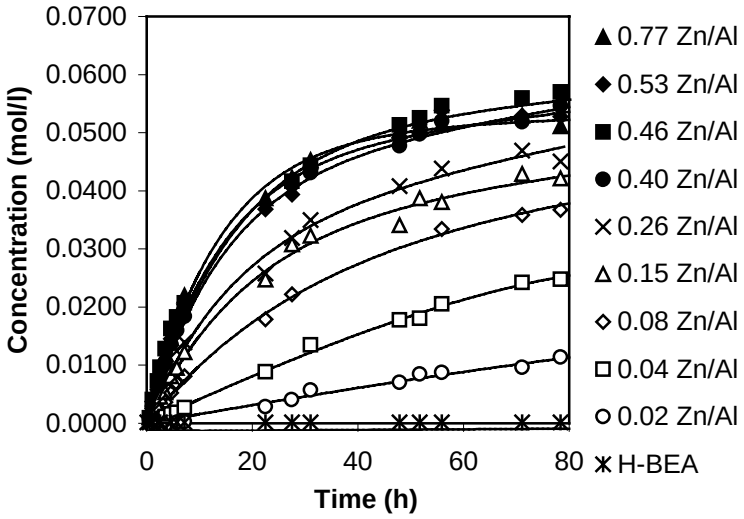


**Fig. 12** Addition of aniline to phenylacetylene with Zn/H-BEA catalysts loaded with different amounts of $Zn^{2+}$ cations.

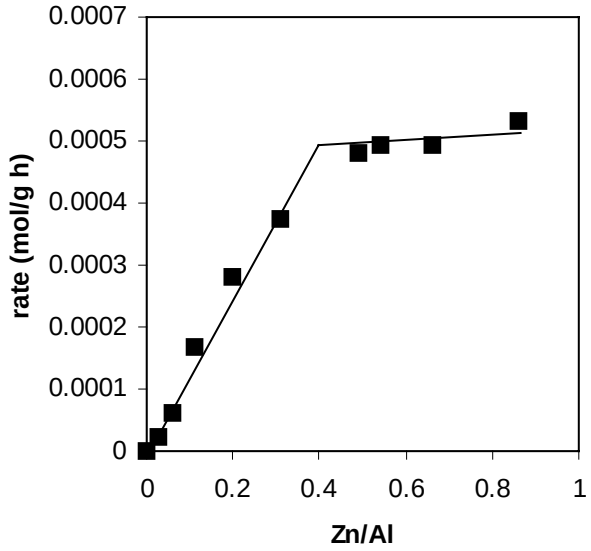


**Fig. 13** Initial rates for the addition of aniline to phenylacetylene with zinc exchanged BEA zeolites containing different amounts of $Zn^{2+}$

The order in catalyst was determined for the cyclization of 6AHI by varying the amount of catalyst (Zn/H-BEA 0.08 Zn/Al) in the range of $0.35 \times 10^{-2}$ to $2.10 \times 10^{-2}$ mmol $Zn^{2+}$. The rate of reaction increased linearly with the amount of zeolite employed. By analysis of the initial rates an order in catalyst of 1.18 was determined. In case of the hydroamination reaction between phenylacetylene and aniline similar experiments were performed, varying the amount of catalyst (Zn/H-BEA 0.08 Zn/Al) in the range of $0.7 \times 10^{-2}$ to $2.00 \times 10^{-2}$ mmol $Zn^{2+}$. The order in catalyst was 1.14 for the intermolecular reaction. Note that an order of one in catalyst indicates that external transport limitations from the bulk solution to the zeolite particles do not exist.

In cyclization of 6AHI, the catalytic activity of Zn/H-BEA zeolites remained constant at zinc loadings above 0.26 Zn/Al. This indicates that in these materials the number of catalytically active zinc cations remained constant independent of the total zinc contents. In respect to their catalytic properties, Zn/H-BEA zeolites with zinc loadings ≥ 0.26 Zn/Al are therefore, equal materials. To further confirm this conclusion the order in these catalysts was determined. Conceptually, not the order in catalyst at one specific zinc loading is of interest, but the order in catalyst determined by employing Zn/H-BEA zeolites with different zinc loadings (≥ 0.26 Zn/Al). In the experiment, the amount of Zn/H-BEA catalysts was varied in the reaction mixture, as indicated in Fig.14. The rate of formation of 2-methyl-1,2-dehydropiperidine increased with the amount of catalysts employed, although approximately the same amount of zinc cations was present. However, if only the concentration of

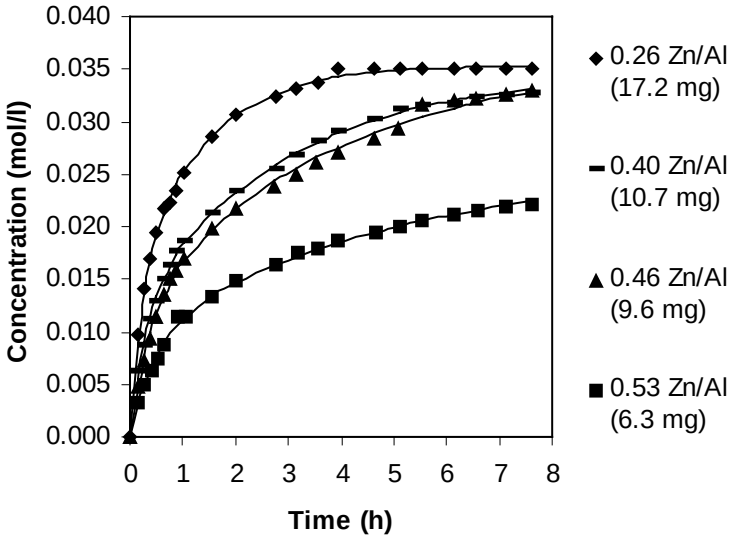


**Fig. 14** Cyclization of 6AHI employing Zn/H-BEA with high zinc contents (> 0.26 Zn/Al, see text)

catalytically active zinc cations is considered, the order in catalyst calculated to 1.21. This result is in good agreement with the order in catalyst of 1.18 obtained at one zinc loading (0.08 Zn/Al). Therefore, it is concluded that above a zinc loading of 0.26 Zn/Al, the same concentration of catalytically active zinc is present in the material.

The activation energies in the cyclization of 6AHI were determined for zinc based homogeneous ($Zn(CF_3SO_3)_2$) and heterogeneous Zn/H-BEA (0.40 Zn/Al) catalysts [107]. Fig. 15 shows the determination of the activation energy using Arrhenius law for Zn/H-BEA (0.40 Zn/Al) as catalyst in the temperature range 82 – 125°C.

The formation of the product was followed by UV-spectroscopy. For the heterogeneous catalyst an activation energy of 62 kJ/mol was calculated from the rate of reaction. For the corresponding homogeneous catalyst $Zn(CF_3SO_3)_2$ an activation energy of 44 kJ/mol was found. As the activation energy is higher for the heterogeneous catalyst, than for the homogeneous catalyst diffusion limitation seems unlikely.

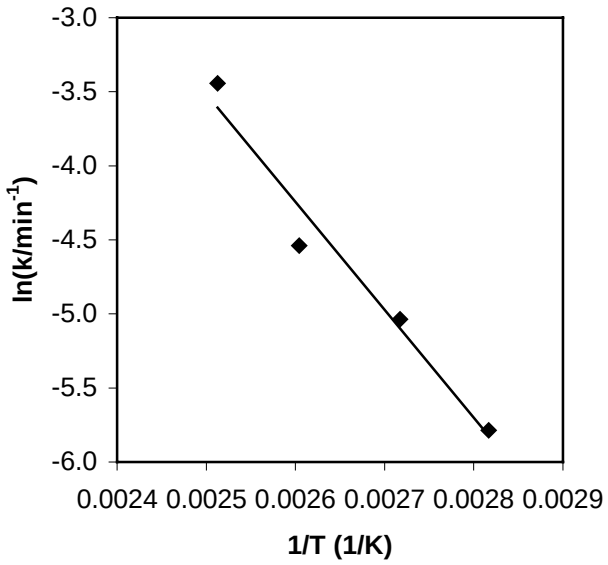


**Fig. 15** Detemination of the activation energy for Zn/H-BEA (0.40 Zn/Al) catalyst (NIR, toluene, s/c 100).

## 8. Kinetic model of the cyclization of 6AHI

More detailed mechanistic studies on the cyclization of 6AHI were performed using NIR- and UV-spectroscopy [107]. Fig.16 shows the change in concentration of substrate 6AHI and product 2MDP as obtained from *in situ* NIR-spectroscopy. Initially, the concentration of 6AHI decreased rapidly, whereas 2MDP was formed with a time delay. At

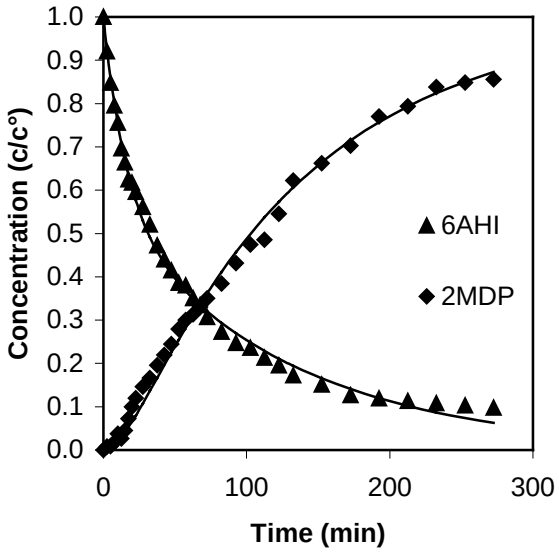


**Fig. 16:** Concentrations of 6AHI and 2MDP measured (points) and calculated from the model (lines) in the cyclization of 6AHI with Zn/H-BEA (NIR, toluene, 125°C, s/c 100).

longer reaction times, the concentration of 2MDP increased, but always remained lower than expected from the decrease in the concentration of 6AHI. The mass balance can, however, be closed by assuming that an intermediate species had formed in the reaction mixture. In order to confirm the nature of the intermediate, the reaction was followed with *in situ* $^{1}$H-NMR spectroscopy [108]. Transient signals were observed at 3.40 and 3.24 ppm and assigned to the two chemically different methylene protons of the enamine. This confirmed that the intermediate was 2-methylenepiperidine.

A mathematical model was developed to describe the course of the reaction and to derive the rate constants of each reaction step. The simplest model which described the reaction adequately, was based on a reversible conversion of substrate S to the intermediate I, followed by irreversible reaction to the product P (eq. 1) [109].

(1) $$S \underset{k_{-1}}{\overset{k_1}{\rightleftharpoons}} I \xrightarrow{k_2} P$$

This reaction sequence can be mathematically described by the improved steady-state solution [110]. The exact solutions are known, [111], [112] and are given in equations 2 to 4.

(2) $$[S]_t = \frac{[S]_0}{\alpha - \beta}\left\{(k-\alpha)e^{-\alpha t} - (k-\beta)e^{-\beta t}\right\}$$

(3) $$[I]_t = \frac{k_1[S]_0}{\beta - \alpha}\left(e^{-\alpha t} - e^{-\beta t}\right)$$

(4) $$[P]_t = [S]_0\left(1 + \frac{\beta}{\alpha - \beta}e^{-\alpha t} - \frac{\alpha}{\alpha - \beta}e^{-\beta t}\right)$$

where $k = k_{-1} + k_2$, $\alpha\beta = k_1 k_2$, $\alpha + \beta = k_1 + k_{-1} + k_2$.

Using this set of equations, the parameters α, β and *k* were fitted to the experimental data. From these parameters the respective rate constants $k_j$ for the individual reaction steps were calculated. As an example, in case of cyclization of 6AHI with Zn/H-BEA (0.40 Zn/Al) at 125°C values of $k_1 = 31.9 \times 10^{-3}$, $k_{-1} = 23.3 \times 10^{-3}$ and $k_2 = 15.9 \times 10^{-3}$ $min^{-1}$ were found (Fig. 16). The slowest step in the reaction sequence was the isomerization of the enamine to the imine product. Both sequential reactions were faster than the irreversible reaction. This is in line with the fact that an intermediate is formed in significant concentrations. The equilibrium constant $K_{eq}$, which formally describes the equilibrium between substrate and intermediate, is on the side of the intermediate ($K_{eq} = 1.3$). In the kinetic analysis, the role of the catalyst was neglected as its concentration remained constant. Therefore, the rate constants $k_i$ are effective rate constants, which have to be divided by the catalyst concentration to obtain the rate per metal cation.

The mathematical model allowed predicting the concentration of the intermediate, which reached a maximum concentration of ca. 37 % after 1/2 hours. Both data and model indicate the formation of an intermediate species, which was assigned to the free enamine. Thus, the rate of reaction is limited by the isomerization of the enamine to the imine product, whereas the metal catalyzed part, as well as intra-porous or external diffusion, had less influence on the overall rate of reaction [113].

## 9. **Conclusions**

The activity of transition metal based heterogeneous catalysts in hydroamination reactions was studied for the cyclization of 6AHI and 3APE, as well as for the reaction between phenylacetylene and aniline. It was shown that catalyst systems based on $Rh^+$, $Cu^+$, and $Zn^{2+}$ exchanged BEA zeolites were especially suitable in hydroamination reactions. The

low activity of the catalysts in the intermolecular hydroamination reaction is related to the unfavorable reaction entropy. However, it was demonstrated that, in principle, a zeolite catalyst system is suitable. A small but not negligible activity of the parent H-BEA zeolite in the conversion of 6AHI and 3APE was explained by leaching of aluminum into the toluene phase. The influence of the metal loading on the catalytic activity was examined for Zn/H-BEA zeolites. It was found that the reactivity of zinc is directly related to its location in the structure. To exhibit catalytic activity zinc must be coordinated to two Brønsted acid sites in vicinity. A kinetic model was developed which allowed describing the reaction kinetics of the cyclization of 6AHI. The simplest mathematical model, which described the course of the reaction adequately was based on a reversible followed by an irreversible reaction to the product.

# IV Mechanistic studies

## 1. Introduction and theory

Several reaction pathways have been suggested for hydroamination reactions. However, experimental evidence is, at present, insufficient to distinguish unambiguously between these reaction mechanisms. For late transition metals two possible pathways are described. These involve either activation of the amine functionality or of the triple bond. Oxidative addition of the amine group to the metal center yields a hydrido-amido intermediate (Scheme 1 left). During this elementary reaction, the formal oxidation state of the metal center increases from n to n+2. The oxidative character of the addition and, thus, the change in electron density on the metal center strongly depends on the electronegativity of the metal and the new ligand formed [114]. For the oxidative addition of amines to late transition metals, a decrease in electron density on the metal is expected, as both hydrido and amido ligand have a higher electronegativity than the metal. By subsequent insertion of the unsaturated CC group

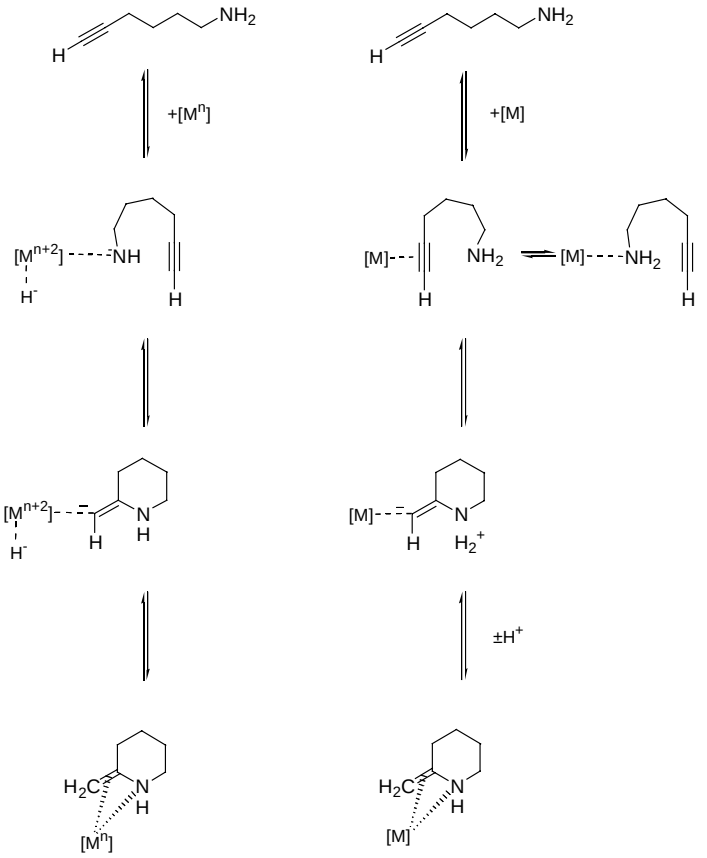


**Scheme 1** Possible pathways of hydroamination reactions catalyzed by transition metals. Shown are mechanisms *via* oxidative addition (left) and nucleophilic attack (right) for the model substrate 6AHI.

into the metal - amide bond, the new carbon nitrogen bond is formed. Reductive elimination yields the hydroamination product and regenerates the metal center in the original oxidation state. The only examples, where this reaction pathway seems likely, are based on Ir and Rh catalysts [28], [29]. Theoretical studies on group 9 and 10 transition metals showed, that oxidative addition to Rh and Ir complexes is an exothermic process ($\Delta H$ = - 72 kJ/mol) [115]. The overall hydroamination reaction is slightly exothermic or approximately thermoneutral [3], [116], [117]. From the energy balance it is speculated, that either the insertion of the olefin into the metal – nitrogen bond or the reductive elimination is the most endothermic and, thus, rate limiting step in the oxidative addition pathway. This hypothesis is supported by observations on Rh catalyzed hydroamination. A reaction order of 0.14 in amine and 0.85 in aromatic olefin is consistent with rapid activation of the amine by oxidative addition to the rhodium center, followed by a slow insertion reaction [29].

For $Zn^{2+}$ based hydroamination catalysts an oxidative addition pathway seems unlikely and an alternative pathway is probably valid. Initial coordination of the unsaturated CC functionality to the metal center renders the $\pi$-system susceptible to attack by exogenous nucleophiles (Scheme 1 right). C - N bond formation can then occur by subsequent nucleophilic attack of the amine yielding an 2-ammonioalkenyl complex. A formal [1,3] - hydrogen shift leads to protonation of the carbon attached to the metal yielding the metal coordinated enamine product. For group 10 transition metals hydroamination *via* nucleophilic attack seems energetically favorable [137]. According to this study, the [1,3] - hydrogen shift from the ammonium group to the alkenyl carbon atom has a very high activation barrier ($E_A$ = 108 kJ/mol) and is, therefore, the rate limiting step.

The metal complex, which is formed before the rate limiting step occurs during the reaction cycle and will have the highest concentration of all intermediates in the reaction mixture. Therefore, in case of nucleophilic attack, the 2-ammonioalkenyl complex will be the most abundant metal species. In case of the oxidative addition pathway, the hydrido-(2-aminoalkenyl) complex, or possibly the hydrido amido complex, will be present in the highest concentration. The two prevailing metal complexes in these pathways have a significantly different electron density at the metal center. Therefore, it is expected that - in case of nucleophilic attack - a higher electron density, whereas - in case of oxidative addition - a lower electron density will be present at the catalytically active metal center. *In situ* observation of the oxidation state will indicate which of the two routes is preferred.

## 2. X-ray absorption spectroscopy

The effect of chemisorption of adsorbate molecules on the catalytically active metal centers was studied by *in situ* XANES measurements. This technique enables to follow the changes in electron density at the metal center [118]. The excitation of 1s electrons by X-ray absorption (K-edge) is strongly related to the electron density on the absorber atom. The first inflection point of the absorption edge was defined as the edge energy. Conceptually, decreasing electron density leads to a shift of the edge to higher energies [104]. Additionally, the electron density is reflected in the intensity of the white line stemming from photo-excitation of electrons from the 1s to the 4p orbital. Increasing electron density leads to a more occupied 4p orbital and, thus, to a decreasing white line. Experimentally, the intensity of the white line was determined by fitting an arctangent and a Lorentzian function to the normalized spectrum [119]. The area between the two curves is attributed to the intensity of the white line. Note, that the area of the white line can only be compared for similar coordination spheres. The shape and the intensity of the white line also vary with the local geometry and the number of ligands around the absorber atom. For metal containing zeolites it had been noted before that adsorption of solvent molecules generally leads to a sharp absorption edge and to an increase of the white line area compared to the solvent free material [120].

The local structure and binding sites were determined by Extended X-ray Absorption Fine Structure (EXAFS) measurements. A photoelectron emitted, which travels as a spherical wave, may be backscattered by surrounding atoms. The reflected wave, which is phase shifted, undergoes self-interference with the outgoing wave; this interference modifies the absorption cross-section and results in fine structure which extends above the absorption edge. Since backscattering will occur from several shells around the absorber atom, the resulting fine structure represents the sum of the individual sine-wave-like contributions from each individual shell and extends about 1500 eV above the edge [118]. In summary, the coordination sphere around the absorber atom is reflected in the shape of the EXAFS spectra.

## 3. *In situ* measurements

EXAFS and XANES spectra were recorded (i) for the parent catalyst in the solid state, (ii) catalyst dissolved (dispersed) in the appropriate solvent and (iii) after the addition of reactant, i.e., 6AHI. In the appendix, the experimental conditions, the reference materials and the edge energies are summarized (Table 5).

### *3.1 Oxidation states of the parent catalyts*

By comparison of the edge energies from reference materials and parent catalyst in the solid state, the oxidation state of the latter can be estimated. Copper in oxidation state +I can be distinguished by a pre-edge peak with a maximum at 8982 eV [121]. This peak is assigned to the $1s \rightarrow 4p_{x,y}$ electric-dipole allowed transition. It was found that CuO had also a pre-edge peak but the maximum is located at 8986 eV which is discussed controversially in the literature. It is either assigned to a 1s→4s or to a 1s→4p transition [121], [122], [123]. However, the peak intensity is generally low and the position not below 9885 eV. For comparison of the edge energies the first inflection points of the pre-edge peaks were used. For the copper reference materials edge energies of 8977.00 eV for metallic copper, 8980.85 eV for $Cu_2O$ and 8984.25 eV for CuO were found. The untreated copper catalysts $[Cu(CH_3CN)_4]PF_6$ and Cu(I)/H-BEA (0.61 Cu/Al) showed edge energies similar to $Cu_2O$ (8980.88 eV and 8980.59 eV, respectively). Furthermore, in the XANES spectra of both samples the characteristic Cu(I) pre-edge peak was present. Thus, Cu in the untreated copper catalysts was present in the expected oxidation state +I. For the zinc reference materials edge energies of 9659.00 eV for metallic zinc and 9661.82 eV for ZnO were found. The untreated zinc catalysts $Zn(CF_3SO_3)_2$ and Zn/H-BEA (0.08 and 0.53 Zn/Al) showed slightly higher edge energies (9663.86 eV, 9663.00 eV and 9663.05 eV, respectively). This indicates a lower electron density on zinc compared to ZnO. This is attributed to the significantly different coordination sphere around zinc [106]. The formal oxidation state of the parent catalysts will be equal to +II, as - for zinc - higher oxidation states are unlikely. From the edge energies determined for the palladium reference material (metallic palladium 24350.00 eV; PdO 24362.17 eV) and catalysts (Pd/H-BEA (0.32 Pd/Al) 24362.22 eV; $[Pd(Triphos)](CF_3SO_3)_2$ 24364.39 eV) it is concluded, that the latter were present in the expected oxidation state +II.

### *3.2 XANES studies on copper based catalysts*

Dissolution of the homogeneous copper catalyst ($[Cu(CH_3CN)_4]PF_6$) in $CH_3CN$ did not lead to major changes in the XANES spectra. This indicates that the metal center had a similar electron density and coordination sphere in solution and in the solid state. This is expected as the solvent $CH_3CN$ does not lead to changes in the coordination sphere around the copper metal cation. Apparently, the number of $CH_3CN$ molecules in the ligand sphere remained unchanged. In contrast, dispersion of the heterogeneous catalyst Cu(I)/H-BEA (0.61 Cu/Al) in $CH_3CN$ led to a shift in edge energy of 0.30 eV to higher energy.

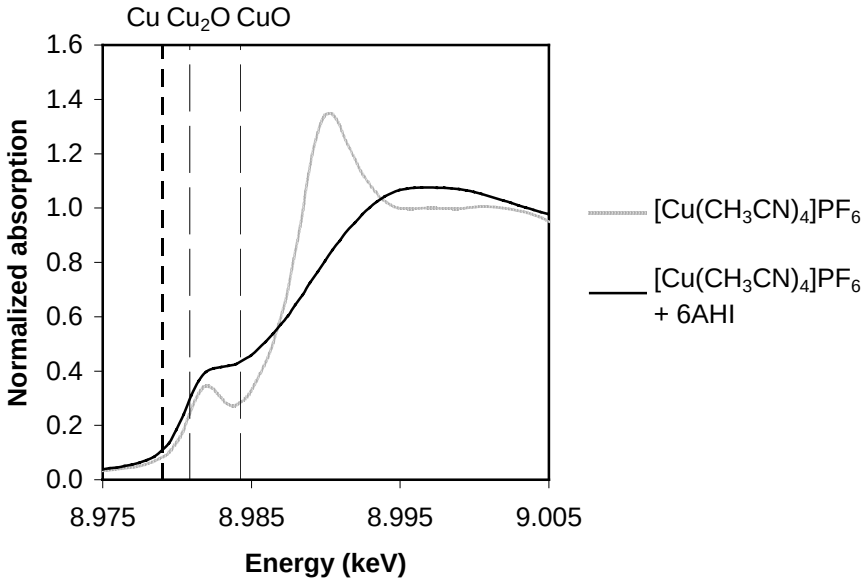


**Fig. 17** XANES spectra of $[Cu(CH_3CN)_4]PF6$ dissolved in $CH_3CN$ before and after the addition of 6AHI. Indicated are the edge positions of the metallic Cu, $Cu_2O$ and CuO.

Conceptually, this indicates a lower electron density on copper caused by coordination of $CH_3CN$. In the untreated Cu(I)/H-BEA the copper probably has a similar coordination sphere as in Zn/H-BEA [106], which can be described as a distorted square pyramidal arrangement. Four oxygen atoms of the zeolite framework constitute the base and the copper atom the tip of the pyramid. By adsorption of $CH_3CN$, copper can adopt a more preferred tetrahedral geometry. A similar mechanism was published for adsorption of probe molecules on zinc exchanged zeolites [124]. Upon coordination of $CH_3CN$ the average distance from copper to the negatively charged oxygen atoms increases. Electron donation by the oxygen ligands is partly replaced by that of nitrogen ligands. π-Backbonding from an occupied copper d-orbital to the empty $p_\pi^*$ (2 π) – orbital of the nitrile group lowers the electron density on copper [125].

After addition of 6AHI to each of the solutions containing the copper catalysts, the shape of the XANES spectra changed significantly (Fig. 17, shown for the homogeneous catalyst). This indicates that the electron density and the coordination sphere around copper had changed relative to the activated catalyst. For both homogeneous and heterogeneous catalyst the white line decreased in intensity upon addition of 6AHI. This is in perfect agreement with the shift in edge energy observed for the homogeneous catalyst ($\Delta E_{edge}$ = - 0.16 eV), also indicating a higher electron density on copper (Fig. 18). Note that, for copper in Cu(I)/H-BEA, a higher edge energy was observed ($\Delta E_{edge}$ = + 0.20 eV) in contrast. For both samples the changes in edge energy were small in comparison to the shift

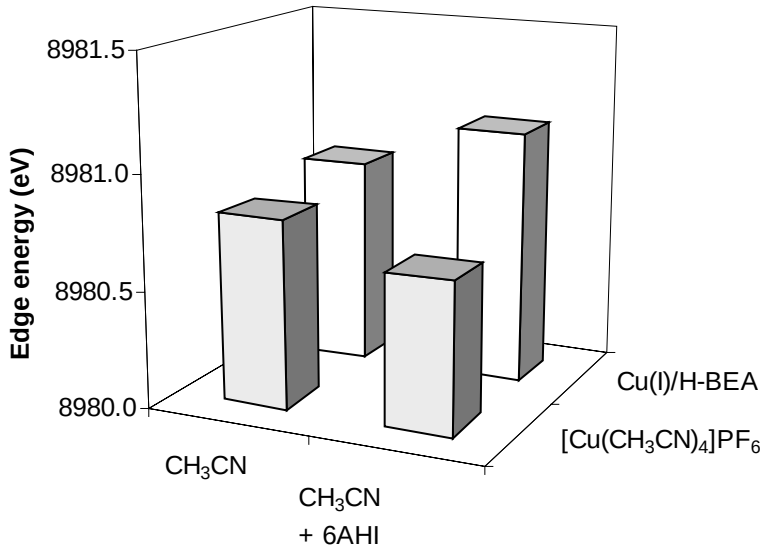


**Fig 18** Cu K-edge energies for copper catalysts dissolved (dispersed) in $CH_3CN$ and under *in situ* conditions.

caused by different oxidation states ($\Delta E_{edge} \approx \pm 4.0$ eV). This indicates that copper is present in the oxidation state +I during catalysis. This result is supported by the presence of the pre-edge transition at 8982 eV, which is characteristic for copper in the oxidation state +I.

As discussed above, an oxidative addition should lead to a significant decrease in electron density on the copper center. This was not observed after the addition of 6AHI. Also the decreasing intensity of the white line is consistent with this conclusion. Thus, it seems unlikely that, during catalysis with copper catalysts, a hydrido-amido complex or a hydrido-(2-aminoethenyl) intermediate was formed *via* the oxidative addition pathway. The results rather support a reaction mechanism *via* activation of the triple bond and subsequent nucleophilic attack, which does not require changes in the oxidation state of the metal center. It is most likely that, similar to group 10 metals, a 2-ammonioalkenyl complex was formed (Fig. 19).

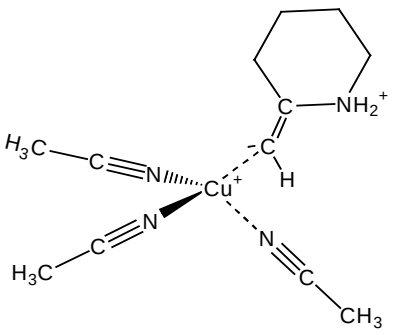


**Fig. 19** 2-Ammoniumalkenyl copper complex proposed as intermediate in the cyclization of 6AHI.

*3.3 EXAFS studies on copper based catalysts*

To confirm this hypothesis the experimental EXAFS signal was extracted from the raw spectra according to standard methods [126]. The threshold energy $E_0$, defining the zero wave vector, was taken at the inflection point of the absorption edge. In Fig. 20 the magnitudes of Fourier transformations (FT) of the Cu-K edge k $\chi$ (k) are compiled for the homogeneous catalyst dissolved in acetonitrile before and after addition of 6AHI. The structure of $[Cu(CH_3CN)_4]^+$ and the 2-ammonioalkenyl complex (Fig.19) was then calculated and, on basis of these data, the radial distribution function (r.d.f.) estimated using FEFF calculations [127].

In case of the homogeneous catalyst peaks were present in the radial distribution function below 1.5 Å. These reflect backscattering of photoelectrons from interstitial charge density around the absorber atom [128], which results in peaks in the Fourier transform at approximately half of the nearest neighbor distance. For $[Cu(CH_3CN)_4]PF_6$ dissolved in acetonitrile and the cation $[Cu(CH_3CN)_4]^+$ in the geometry calculated good agreement between the radial distribution functions was observed. The r.d.f. is dominated by the first-shell Cu-O contributions at 1.67 Å and 1.57 Å, respectively, in the non phase-shift corrected Fourier transform. These peaks reflect the contributions of the four nearest nitrogen neighbors at a distance of 1.99 Å after phase shift correction. At further distances, peaks were present at 2.76 Å and 2.67 Å in the observed and calculated radial distribution function, respectively.

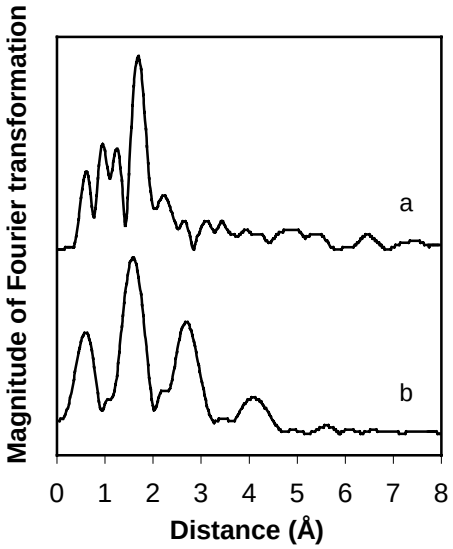


**Fig.20** EXAFS Cu K-edge radial distribution function for
a) $[Cu(CH_3CN)_4]PF_6$ + 6AHI in $CH_3CN$
b) $[Cu(CH_3CN)_4]PF_6$ in $CH_3CN$

These peaks may be ascribed to the backscattering carbon atoms in the second shell at a distance of 3.17 Å after phase shift correction.

For the mixture of $[Cu(CH_3CN)_4]PF_6$ and 6AHI the first shell contribution was at 1.72 Å in the Fourier transformation. This indicates coordination of an atom at a larger distance to the metal center or the formation of a second coordination sphere around copper. The corresponding contribution calculated for the 2-ammonioalkenyl complex was located at a closer distance (1.57 Å). However, the calculations do not take into account the contributions of the $CH_2$-group at C3 (see Fig. 19). The first shell contribution reflects the coordination of the three nearest nitrogen and single carbon neighbors to copper. In the second coordination sphere a peak was present at 2.30 Å in the observed and the calculated radial distribution function. This indicates a similar coordination around copper at this distance. It probably reflects the contribution of three carbon neighbors from coordinated $CH_3CN$ and one carbon neighbor of the 2-ammonioalkenyl ligand. In case of the heterogeneous copper catalyst similar results were obtained. The formation of a 2-ammonioalkenyl intermediate mainly results in changes in the second coordination sphere. The comparison of the observed with the calculated radial distribution function confirms this hypothesis. This is in agreement with a copper coordinated 2-ammonioalkenyl intermediate as the most abundant metal species in homogeneous and heterogeneous catalyzed reaction.

### *3.4 XANES studies on zinc based catalysts*

*In situ* XANES measurements were also performed to investigate whether an oxidative addition or nucleophilic attack route is more likely for $Zn^{2+}$ based catalysts. In a first step the parent homogeneous ($Zn(CF_3SO_3)_2$) and the activated heterogeneous (Zn/H-BEA 0.08; 0.53 Zn/Al) catalysts were compared to the corresponding catalysts dissolved / dispersed in acetonitrile. The addition of $CH_3CN$ to $Zn^{2+}$ based catalysts led to an increase in the white line area. This is attributed to the adsorption of polar solvent molecules on the zinc Lewis acid sites. For metal exchanged zeolites such an increase in the white line area is frequently observed [120]. Additionally, upon addition of $CH_3CN$ the shape of the XANES signal changed significantly at energies higher than 15 eV above of the edge. Thus, the coordination sphere around zinc had changed by coordination of $CH_3CN$. In case of the homogeneous catalyst $Zn(CF_3SO_3)_2$ the Zn K-edge is shifted by 1.18 eV to lower energy. It is known that $CH_3CN$ coordinates more strongly to transition metals than $CF_3SO_3^-$ [129]. This shows that replacement of the two $CF_3SO_3^-$ anions by most likely, four $CH_3CN$ molecules in the zinc coordination sphere leads to a significant increase in electron density on zinc. In contrast,

dispersion of Zn/H-BEA (0.08 Zn/Al) in $CH_3CN$ led to a shift in edge energy by 0.98 eV to higher energy. This indicates a lower electron density on zinc. In the parent material zinc is bound to six membered rings of oxygen atoms. It was shown that these 6 membered rings are distorted leading to four nearest and two distant oxygen neighbors [106]. The adsorption of $CH_3CN$ molecules on such zinc cations leads to a framework relaxation [106], [130] as well to a more preferred tetrahedral geometry of ligands around zinc. The higher zinc oxygen distances observed in this case and the additional coordination of $CH_3CN$ in total lower the electron density on zinc. Additionally, the π-backbonding from an occupied zinc d-orbital to the empty $p_\pi^*$ (2 π) – orbital of the nitrile group will also lower the electron density at the zinc center. In contrast, when a sample of Zn/H-BEA with a high zinc loading (0.53 Zn/Al) was dispersed in $CH_3CN$, the zinc K-edge was shifted to lower energy ($\Delta E_{edge}$ = - 0.17 eV). Thus, a higher electron density on the metal center was observed. This can be explained by the presence of different zinc sites in this material. Only 40 % of the total zinc cations are bound to six membered oxygen rings, while 60 % is present as ZnO. From XANES spectra it is not possible to distinguish between these zinc phases as the excitation of 1 s electrons is not energetically separated.

The addition of 6AHI to $Zn(CF_3SO_3)_2$ and Zn/H-BEA (0.08 Zn/Al) dissolved (dispersed) in $CH_3CN$ led to a shift of the edge to lower energy and a decrease in the intensity of the white line (Fig. 21). This indicates a higher electron density on zinc during catalysis. However, the changes in edge energy are small ($\Delta E_{edge}$ = - 0.51 and – 1.34 eV) in comparison

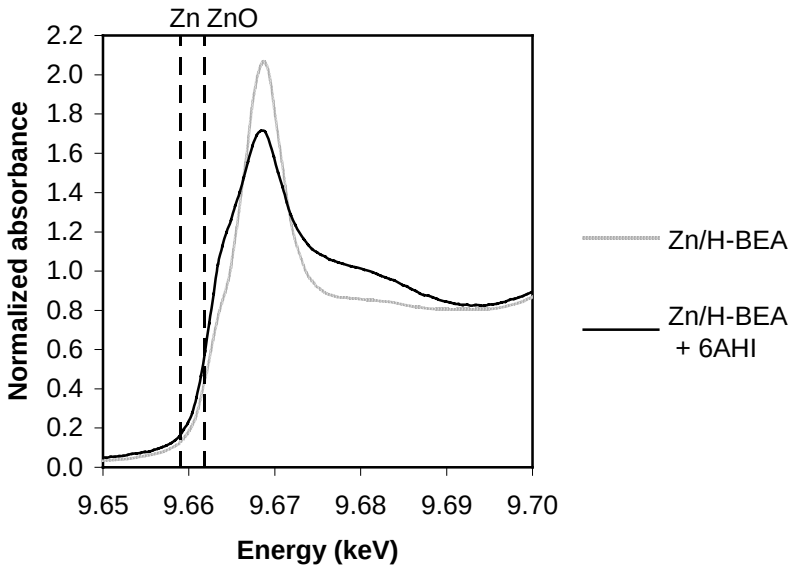


**Fig. 21** XANES spectra of Zn/H-BEA (0.08 Zn/Al) dispersed in $CH_3CN$ before and after the addition of 6AHI.

to the shift in edge energy caused by changes in the oxidation state ($\Delta E = \pm 2.80$ eV). This indicates that, during catalysis, strongly electron donating ligands are bound to the zinc center. Additionally, upon the addition of 6AHI the shape of the XANES signal changed slightly at energies higher than 15 eV above of the edge. Thus, in comparison to the catalysts dissolved (dispersed), the coordination sphere around zinc changed during catalysis. Similar to the copper catalysts, these observations support a mechanism involving coordination of the triple bond and subsequent nucleophilic attack.

Upon addition of 6AHI no change in edge energy was observed for Zn/H-BEA (0.53 Zn/Al) indicating similar electron densities of this material dissolved in $CH_3CN$ and during catalysis. In the former material an additional ZnO phase is present with approximately 60 %, which was not catalytically active. Catalytically active zinc (present with approximately 40 %) showed a shift in edge energy of - 1.34 eV. Therefore, if the edge energy of ZnO does not change by addition of 6AHI the average edge should be shifted by $\Delta E_{edge} = - 0.73$ eV to lower energy. However, this is not observed indicating partial interaction between 6AHI and this ZnO phase. In contrast, upon addition of 6AHI the intensity of the white line decreased significantly, indicating a higher electron density on zinc. This observation is attributed to the catalytically active zinc species which also showed a remarkable decrease in white line area in Zn/H-BEA (0.08 Zn/Al).

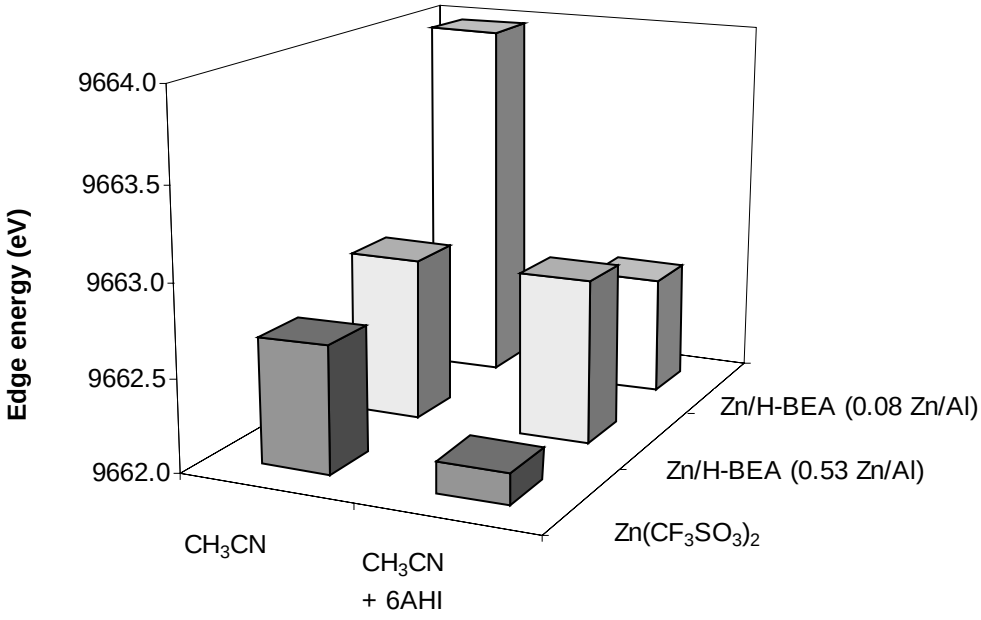


**Fig 22** Zn K-edge energies for zinc catalysts dissolved (dispersed) in $CH_3CN$ and under *in situ* conditions.

### *3.5 XANES studies on palladium based catalysts*

*In situ* XANES measurements were also performed for palladium catalysts. The same set of experiments was repeated with the homogeneous catalyst [Pd(Triphos)]$(CF_3SO_3)_2$ and the heterogeneous catalyst Pd/H-BEA (0.32 Pd/Al). In the homogeneous catalyst the phosphine is coordinated in a three-dentate fashion to the palladium center (Fig 23). In the solid state, the coordination site *trans* to the PPh phosphorus atom is occupied by an oxygen atom of one trifluoromethylsulfonate anion. The geometry is based on the normal square-planar geometry of Pd (II) centers as confirmed by single crystal X-ray analysis [131]. Compared to amine or nitrile ligands, phosphine ligands form stronger σ – bonds to transition metal centers [105]. Therefore, it seems unlikely that, the three-dentate phosphine ligand is displaced during catalysis.

The addition of $CH_3CN$ to [Pd(Triphos)]$(CF_3SO_3)_2$ led to a shift in edge energy of 4.42 eV to lower energy. Thus, replacement of the coordinating $CF_3SO_3^-$ by $CH_3CN$ led to an increase in electron density on palladium. A similar effect was observed when $Zn(CF_3SO_3)_2$ was dissolved in $CH_3CN$. The shape of the XANES signals before and after addition of $CH_3CN$ to [Pd(Triphos)]$(CF_3SO_3)_2$ are very similar indicating minor changes in the coordination sphere around palladium. This is expected as only one coordination site is available for binding of $CH_3CN$ and the new ligand is located at the same place and roughly same distance relative to the palladium center.

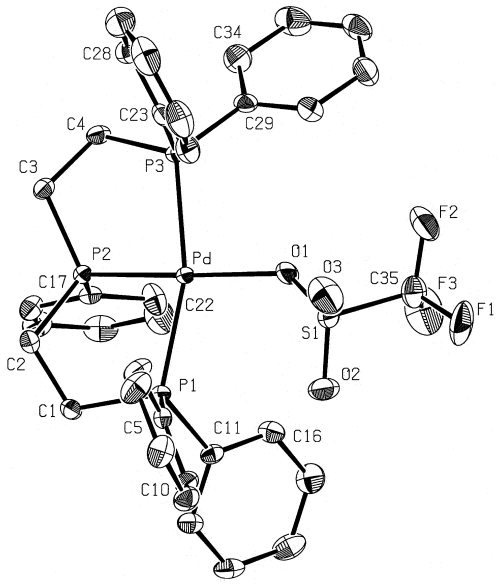


**Fig 23** ORTEP representation of the monocationic part of compound [Pd(Triphos)]$(CF_3SO_3)_2$ in the solid state. Thermal ellipsoids are at the 50% probability level.

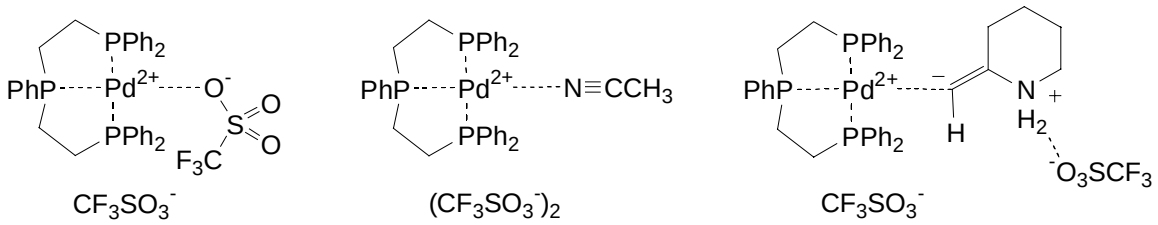


**Fig. 24** Molecular structure of the complex [Pd(Triphos)]$(CF_3SO_3)_2$ in the solid state, when dissolved in $CH_3CN$ and after the addition of an excess of 6AHI.

Slurrying of Pd/H-BEA (0.32 Zn/Al) in $CH_3CN$ led to a shift in edge energy of 0.31 eV to higher energy. This indicates a lower electron density on palladium. Similar results were obtained for dispersion of Cu(I)/H-BEA and Zn/H-BEA and are discussed above.

The addition of 6AHI to [Pd(Triphos)]$(CF_3SO_3)_2$ dissolved in $CH_3CN$ led to a shift in edge energy of 0.23 eV to higher energy and to a decrease in white line area. The shift in edge energy indicates a lower electron density on the metal, whereas from the decreasing white line area an increasing electron density can be concluded. Thus, no clear trend in electron density can be distinguished for this sample. In comparison to the other transition metal catalyst systems examined the changes are small. The signal to noise ratio was high in case of the palladium samples and the determination of the exact edge energy appeared to be difficult. Probably the changes in the white line area are more accurate and the overall electron density increased during catalysis. Similarly, the addition of 6AHI to Pd/H-BEA (0.32 Pd/Al) dispersed in $CH_3CN$ led to an increase in electron density on palladium as can be concluded from the shift in edge energies ($\Delta E_{edge}$ = - 0.17 eV). For both palladium catalysts the changes

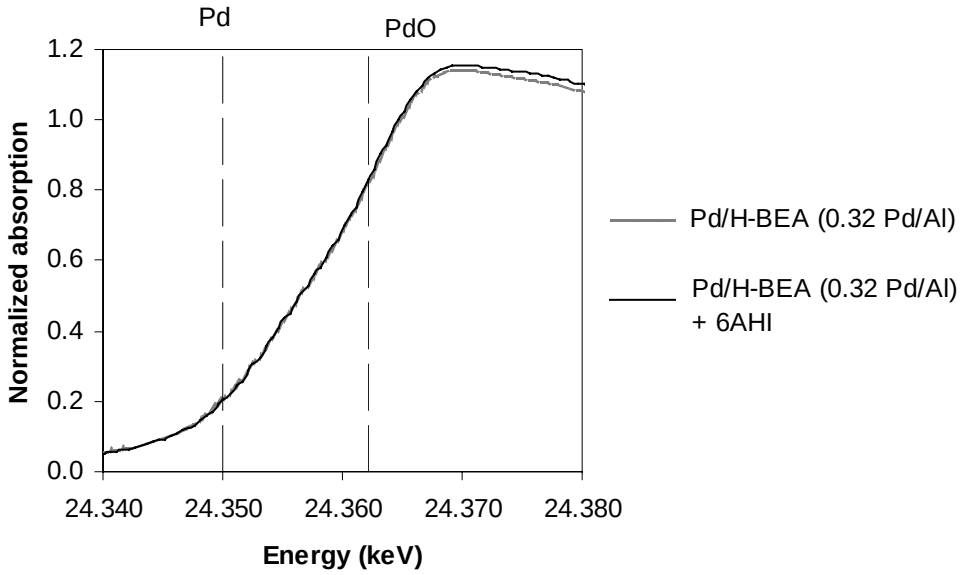


**Fig. 25** XANES spectra of Pd/H-BEA (0.32 Pd/Al) dissolved in $CH_3CN$ before and after the addition of 6AHI.

in edge energy were small indicating minor changes. Nevertheless, similar to copper and zinc the data are consistent with a mechanism involving initial coordination of the triple bond and subsequent nucleophilic attack.

This conclusion is in perfect agreement with results published in literature. Olefins coordinated to dicationic palladium complexes were found to be highly activated towards nucleophilic addition [141]. According to a DFT study on the coordination of olefin vs. nitrogen ligands to Pd (II) catalysts, alkyl-substituted amines of the general equation $CH_2{=}CH(CH_2)_nNH_2$ ($n \geq 1$) show a larger relative preference for π binding to the unsaturated CC bond [30]. Additionally, in case of the homogeneous catalyst the tridentate phosphine ligand inevitably makes the oxidative addition of H–N more difficult as only one coordination site is available. In consequence for this catalyst, the mechanism suggested is favored as it requires a single coordination site. However, the mechanism proposed is not necessarily applicable to reactions involving palladium complexes with bi- and mono-dentate ligands [132], [133].

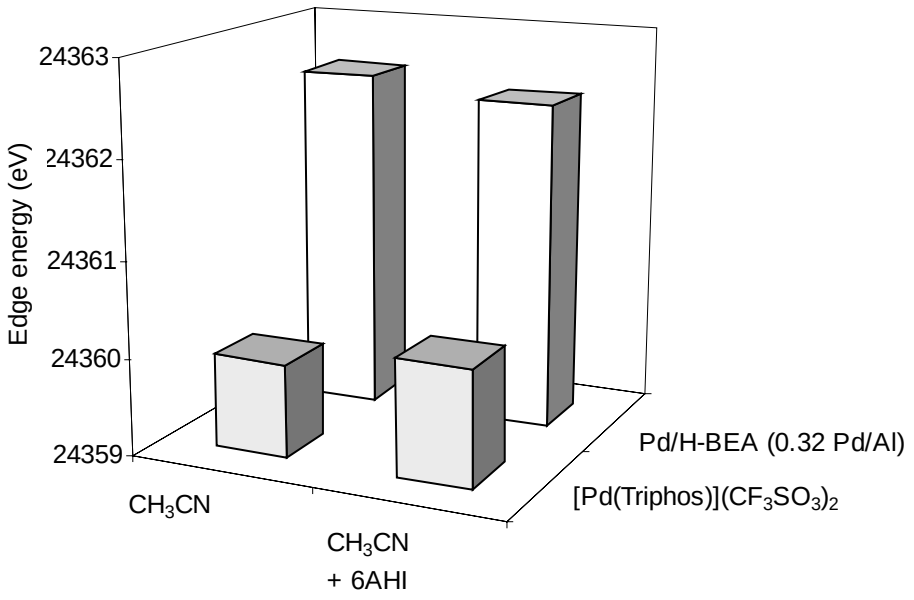


**Fig 26** Pd K-edge energies for palladium catalysts dissolved (dispersed) in $CH_3CN$ and under *in situ* conditions.

## 4. $^{31}$P-NMR – study on palladium catalysts

To confirm the nature of the reaction intermediate, which is present in the highest concentration, *in situ* $^{31}P\{^1H\}$-NMR study was employed [134]. The chemical shift of the $^{31}P$ nuclei is a sensitive probe for processes occurring at the palladium center. An oxidative addition to the palladium center would lead to a large shift in the $^{31}P\{^1H\}$-NMR signal to

higher frequencies. In contrast, a route *via* nucleophilic attack would lead to intermediate species with approximately the same chemical shift as in the parent complex. In the experiment, a 100 fold excess of 6AHI was added to a solution of [Pd(Triphos)]$(CF_3SO_3)_2$ (**1**) in $CDCl_3$ and a $^{31}P\{^1H\}$-NMR spectrum of the mixture taken. Only two NMR signals were observed at 102.8 and 45.2 ppm in a ratio of 1:2 (Fig. 27). These can be assigned to the PPh moiety and the two $PPh_2$ groups of an unknown palladium complex 4. The high concentration of the complex 4 in the catalytic mixture indicates that it is an intermediate in the reaction sequence. The chemical shift of the unknown intermediate is, however, very close to the parent complex 1 (116.7 and 52.7 ppm). This indicates a mechanism via nucleophilic attack.

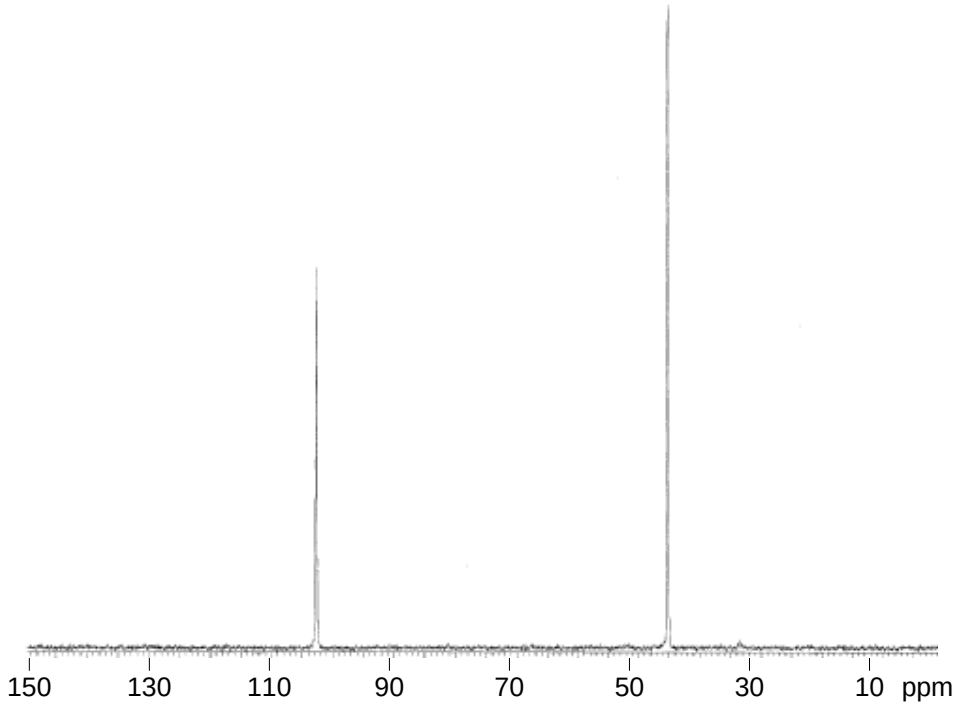


**Fig. 27** $^{31}P\{^1H\}$-NMR spectrum of the reaction mixture during the cyclization of 6AHI with [Pd(Triphos)]$(CF_3SO_3)_2$.

In order to identify this complex, one equivalent of 6AHI was added to a solution of [Pd(Triphos)]$(CF_3SO_3)_2$ in $CDCl_3$. The $^{31}P\{^1H\}$-NMR spectrum of the mixture showed two signals at 109.5 and 53.9 ppm in a 1:2 ratio. These are assigned to formation of the cyclization product which remains coordinated to the palladium center (**5**). Additional weaker signals at 116.7/52.7 ppm and 102.7/45.2 ppm can be assigned to the parent palladium complex (**1**) and the unknown intermediate (**4**), respectively (Table 2). To test the hypothesis that the unknown intermediate is the result of a nucleophilic attack [135], [136], heptyne and $NEt_3$ were added in stochiometric quantities to a solution of [Pd(Triphos)]$(CF_3SO_3)_2$. A complex **2** formed *in situ* and gave rise to two signals in the $^{31}P\{^1H\}$-NMR spectrum which occur at exactly the same chemical shift as observed for the unknown intermediate. Thus, the direct environment

of the palladium center must be very similar in the two complexes and is assigned to [(Triphos)$Pd^{2+}$($CH^{-}$=CR-$NR'_3{}^{+}$)] with R = alkyl, R' = H/alkyl. This assignment is in agreement with the results obtained from EXAFS measurements where a mechanism involving nucleophilic attack was postulated. This mechanism yields a similar 2 - ammonioalkenyl complex. Theoretical calculations on hydroamination of ethylene with ammonia catalyzed by group 10 and group 9 complexes [137] showed that an ammonioalkyl-complex is a likely intermediate during this reaction pathway. Additionally, two pairs of signals were observed with lower intensity at 116.7/52.5 and 112.7/47.5 ppm. Comparison of the chemical shift with reference materials confirmed that these are the parent catalyst **1** and [Pd(Triphos)$(NEt)_3$]$(CF_3SO_3)_2$ (**3**), respectively.

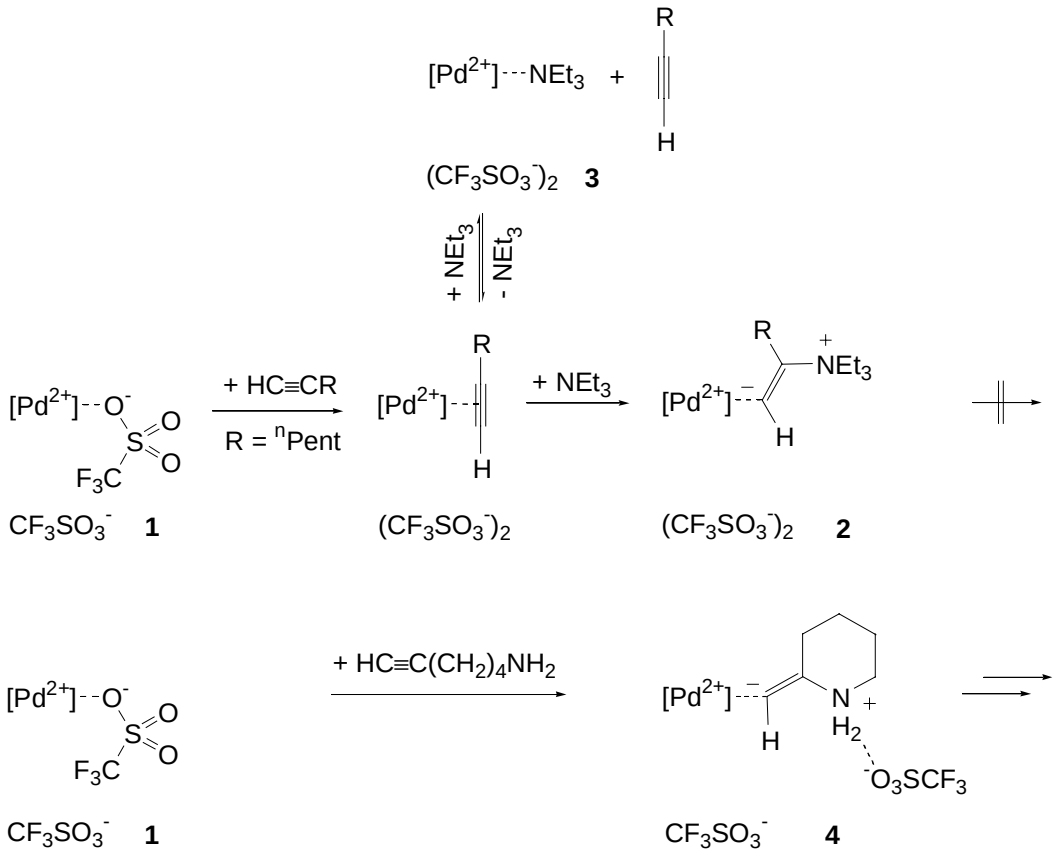


**Scheme 2** Reaction steps for hydroamination on a palladium based catalyst employing various starting materials; [$Pd^{2+}$] indicates [Pd(Triphos)]$^{2+}$.

**Table 2** $^{31}P\{^{1}H\}$-NMR signals observed for *in situ* mixtures of [Pd(Triphos)]$(CF_3SO_3)_2$ and various ligands.

| Ligand for [Pd(Triphos)]$(CF_3SO_3)_2$ | δ(P1) [ppm] | δ (P2/3) [ppm] | Concen-tration [%] | Assign-ment |
|---|---|---|---|---|
| 1 eq. $HC{\equiv}C(CH_2)_4NH_2$ | 116.7 | 52.7 | 2 | **1** |
| | 109.5 | 53.9 | 90 | **5** |
| | 102.7 | 45.2 | 8 | **4** |
| 100 eq. $HC{\equiv}C(CH_2)_4NH_2$ | 102.8 [a] | 45.2 [a] | 100 | **4** |
| 1.) 1 eq. $HC{\equiv}C(CH_2)_4CH_3$ | 116.7 | 52.5 | 4 | **1** |
| 2.) 1 eq. $NEt_3$ | 112.7 | 47.5 | 5 | **3**[b] |
| | 102.9 | 45.3 | 91 | **2** |

[a] 102.8 t ($J(^{31}P,^{31}P)$ = 17.7 Hz); 45.2 d ( $J(^{31}P,^{31}P)$ = 17.8 Hz)
[b] [Pd(Triphos)$(NEt_3)$]$(CF_3SO_3)_2$

## 5. Reaction order

The similar observations in XANES indicate that zinc, copper and palladium catalyze the hydroamination *via* the same reaction pathway. This is most likely the pathway involving the nucleophilic attack, which is rate limited by the 1,3-hydrogen shift. For this pathway an order in amine and alkyne of one is expected, as the new C-N bond is formed before the rate determining step. In order to probe this, we have determined the reaction orders in starting materials for the zinc catalyzed (Zn/H-BEA 0.15 Zn/Al) hydroamination of phenylacetylene and aniline. The concentration of aniline and phenylacetylene in the reaction mixture was varied in the concentration range 0.03 – 0.1 mol/l. The reaction rate strongly depended on the amount of starting material used. By analysis of the initial reaction rates a reaction order of 0.88 in both aniline and phenylacetylene was found. This result is in agreement with the mechanism involving nucleophilic attack.

In contradiction for rhodium catalyzed intermolecular hydroamination an order of 0.14 in amine, 0.85 in aromatic olefin and 1.05 in catalyst was reported [29]. The mechanism is probably different and probably involves activation of the amine functionality by oxidative addition to the rhodium center. This reaction is fast relative to the insertion of the olefin into the rhodium – nitrogen bond. Therefore, the concentration of amine in the reaction mixture does not influence the reaction rate. In contrast, for rhodium catalyzed hydroamination of aliphatic alkynes with anilines a reaction order of one in catalyst, one in amine and zero in

alkyne concentration is reported [138]. The authors assumed that the alkyne is activated by the rhodium center to rate determining nucleophilic attack of the amine.

## 6. Conclusions: The mechanism of hydroamination on transition metal based catalysts

Two reaction pathways have been suggested for hydroamination catalyzed by late transition metals. The key step involves either oxidative addition of an amine to the metal center or nucleophilic attack of an amine an a coordinated alkene/alkyne. In case of the oxidative addition pathway, a hydrido-(2- aminoalkenyl) complex, or a hydrido amido complex, will be formed as intermediate. In case of the nucleophilic attack a 2-ammonioalkenyl complex will be the most abundant metal species. *In situ* XANES spectroscopy on copper, zinc and palladium based catalysts indicated higher electron densities on the metal centers during catalysis. This observation is in agreement with a reaction pathway involving nucleophilic attack. In case of the palladium based homogeneous catalyst $^{31}$P-NMR spectroscopy confirmed the 2-ammonioalkenyl complex as intermediate species.

Based on these observations a catalytic cycle is proposed involving nucleophilic attack. This mechanism is suggested for zinc, palladium and copper based homogeneous and heterogeneous catalysts (Scheme 3). In the first step the substrate is coordinated to the metal center *via* the triple bond. Equilibrium exists, in which the aminoalkyne is coordinated *via* the amine functionality, but does not lead to further reactions. Coordination of π(C≡C) to the

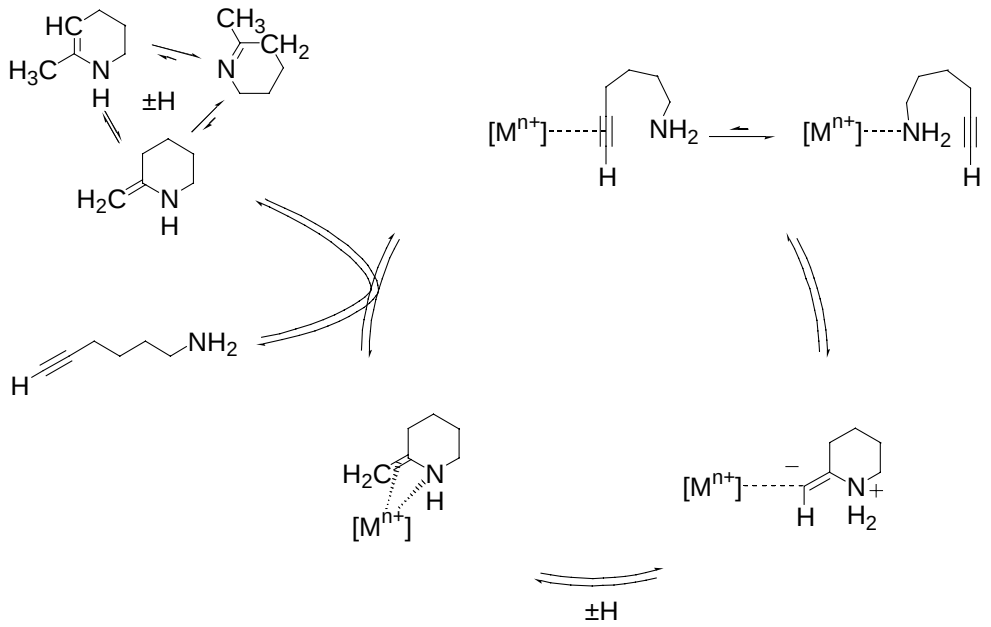


**Scheme 3.** Mechanism proposed for the cyclization of aminoalkynes.
Formal [1,3]-hydrogen shifts are indicated with ±H.

metal center activates the triple bond for a nucleophilic attack of the free electron pair on nitrogen and results in a 2-ammonioalkenyl complex. Protonation of the carbon which is attached to the metal center gives the product 2-methylene-piperidine with an exocyclic double bond. Subsequent desorption of the enamine closes the catalytic cycle. The enamine then reacts *in situ* to the more stable isomeric imine 2-methyl-1,2-dehydropiperidine.

# V The role of protons in hydroamination reactions

## 1. Activity of homogeneous *vs*. heterogeneous catalysts

Hydroamination with homogeneous and heterogeneous catalysts was compared for zinc, copper and rhodium based material. Compared were ion exchanged BEA zeolites and the most active homogeneous catalysts reported [98] employing similar reaction conditions (temperature, molar ratio of reactant to catalyst). In particular, Rh(I)/H-BEA, Cu(I)/H-BEA and Zn/H-BEA were employed as heterogeneous catalysts and $[Rh(NOR)_2]ClO_4$, $[Cu(CH_3CN)_4]PF_6$ and $Zn(CF_3SO_3)_2$ as the corresponding homogeneous catalysts. The cyclization reactions of 6AHI and 3APE (Fig. 28, 29, 30, 31) were studied as model reactions.

In case of cyclization of 6AHI, the transition metal exchanged BEA zeolites were about 5 × more active than the corresponding homogeneous catalysts. After 5 hours 98, 91 and 84 % conversion was obtained for Cu(I)/H-BEA, Rh(I)/H-BEA and Zn/H-BEA, while for the homogeneous catalysts 48, 13 and 58 % conversion was observed for $[Cu(CH_3CN)_4]PF_6$, $[Rh(NOR)_2]ClO_4$ and $Zn(CF_3SO_3)_2$, respectively. Note, that the order in activity was different for the homogeneous (Zn > Cu > Rh) and heterogeneous (Cu > Rh > Zn) catalysts. However, the catalysts based on different metals cannot be directly compared, as the conditions employed were not strictly equal. For the zeolite catalysts the metal loading varied, being 0.47, 0.15 and 0.51 mmol $M^{n+}$ / g zeolite for Cu(I)/H-BEA, Rh(I)/H-BEA and Zn/H-BEA respectively. The complexes employed as homogeneous catalysts have different ligand spheres and counter ions. The coordination of norbornadiene to rhodium is stronger than that

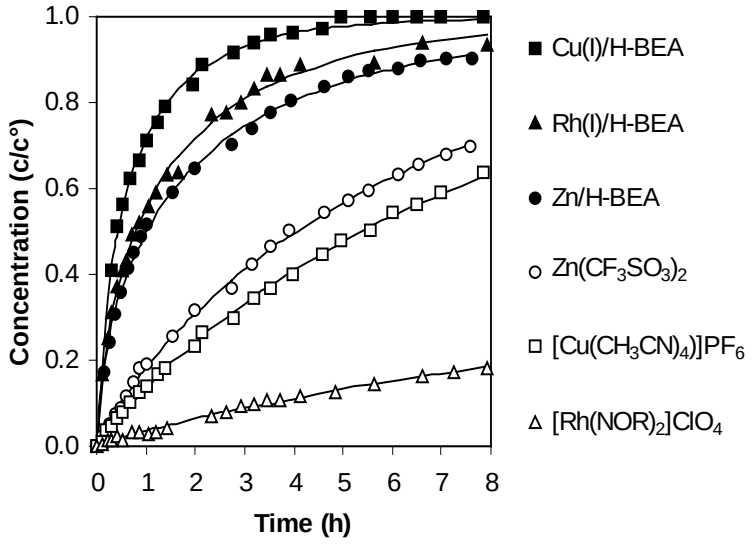


**Fig. 28** Cyclization of 6AHI employing transition metal based BEA zeolites in comparison to the corresponding homogeneous catalysts.

of acetonitrile to copper. In contrast, the zinc cation in $Zn(CF_3SO_3)_2$ is not coordinated to any ligands other than the counter anion $CF_3SO_3^-$. As ligands and coordinating counter anions have to be displaced by the substrate prior to catalysis the order of activity expected for the homogeneous catalysts is Zn > Cu > Rh. The order in activity (Zn > Cu > Rh) observed for the homogeneous catalysts is in perfect agreement with this hypothesis.

As stated above the heterogeneous catalysts were more active than the corresponding homogeneous catalysts. This is contrary to expectation as heterogeneous catalysts are often shown to be less active than homogeneous catalysts. In case of heterogeneous catalysts external diffusion phenomena like interparticular diffusion can slow down the overall reaction rate. The higher activity of homogeneous catalysts results from the higher dispersion of catalyst and the more favored local structure around the cation. Therefore, it is assumed that the high catalytic activity of the heterogeneous catalysts is related to an additional co-catalytic function present in the solid catalysts.

## 2. Mechanistic considerations on protons involved in hydroamination reactions

In the mechanism proposed (Scheme 3) protons are involved in three elementary steps:
(A) As the amine group is the strongest base present in the reaction mixture, added acids will protonate it *in situ* to the ammonium salt, which has a lower tendency to coordinate to the metal center. Thus, the probability of coordination of the alkyne group to the metal center is increased in acidic reaction media.
(B) The protolytic cleavage of the metal - carbon bond in the intermediate 2-ammonioalkenyl complex is facilitated in acidic conditions. The formal [1,3] - hydrogen shift from the ammonium group to the α-carbon atom is, as [1,3] sigmatropic rearrangement, orbital-forbidden [139]. A recent theoretical study suggested that an intermolecular proton transfer was more likely [140]. In this case, an additional proton acceptor, e.g., the counter ion or the solvent, can act as a proton shuttle.
(C) The isomerisation of enamine to the imine is accelerated in the presence of protons. If dissociation of enamine from the coordination sphere is slow, the lower transient concentration of enamine in acidic conditions would result in a higher overall rate of reaction. This requires that the imine formed coordinates not as strong to the metal center as the enamine.

To test hypothesis C the influence of the imine product on the catalytic activity was examined. 2-Methyl-1,2-dehydropiperidine (0.24 mmol) was added to the activated Zn/H-BEA (0.40 Zn/Al) catalyst suspended in toluene and the reaction started by addition of 6AHI. In Fig. 29 the formation of the imine product is compared for reaction mixtures in the

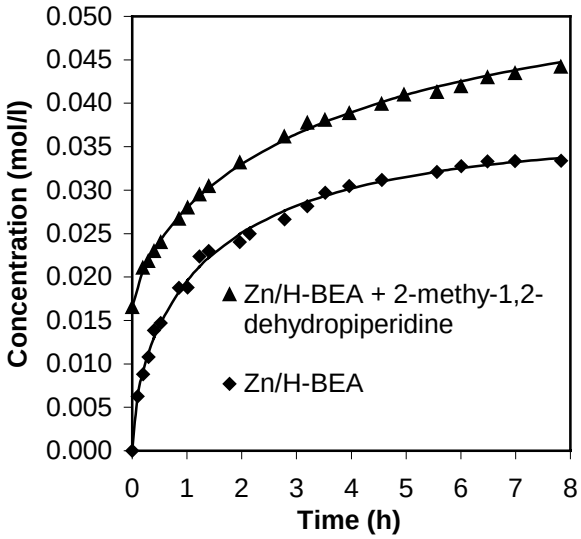


**Fig. 29** Cyclization of 6AHI employing Zn/H-BEA (0.40 Zn/Al) in the presence of 2-methy-1,2-dehydropiperidine (0.24 mmol) compared to standard conditions.

presence and absence of product at the start of the reaction. Similar reaction rates were observed in both experiments. Thus, in cyclization of 6AHI the reaction is not inhibited by product. It therefore seems likely that the product is coordinated only relatively weak to the catalytically active metal center.

Considering the kinetic model developed to describe the reaction (see chapter IV), the rate constant $k_2$ describes a true elementary reaction step, i.e., the isomerization of the enamine to the imine. In this respect it is known that in acidic conditions the equilibrium constant for the enamine imine tautomerism is completely on the side of the imine [142], [143]. This renders the reaction of the enamine to the imine effectively irreversible. $k_1$ and $k_{-1}$ constitute formal rate constants describing the overall rate for the sequence of reaction steps leading from 6AHI to the enamine and the reverse reaction, respectively. The reversibility of a similar reaction cycle has been proven for the addition of nucleophiles to ethylene coordinated on palladium catalysts [141]. The effect of Brønsted acid co–catalysis on the reaction steps B and C can be quantified by calculating the corresponding rate constants. From the data obtained by *in situ* NIR spectroscopy on the cyclization of 6AHI employing the homogeneous catalyst $Zn(CF_3SO_3)_2$ (s/c = 100, 125°C, toluene) the rate constants $k_1 = 5.15 \times 10^{-3}$ min$^{-1}$, $k_{-1} = 7.21 \times 10^{-3}$ min$^{-1}$ and $k_2 = 1.93 \times 10^{-3}$ min$^{-1}$ were calculated. Employing the same reaction conditions, the rate constants $k_1 = 31.9 \times 10^{-3}$ min$^{-1}$, $k_{-1} = 23.3 \times 10^{-3}$ min$^{-1}$ and $k_2 = 15.9 \times 10^{-3}$ min$^{-1}$ were found for the corresponding heterogeneous catalyst. This shows, that in case of the heterogeneous catalyst the following steps are accelerated: (i) the

hydroamination step from 6AHI to the enamine (step B) and (ii) the isomerization of the enamine to the imine product (step C). For latter reaction Brønsted acids are known to be effective catalysts [142], [143], [144], [145]. The rate constant $k_2$ of the isomerization of the enamine to the imine was around 8-fold higher for the heterogeneous compared to the homogeneous catalyst. In zinc exchanged zeolite BEA the concentration of unperturbed Brønsted acid sites remained unchanged upon zinc exchange (0.10 mmol/g) [106]. The latter is also likely for exchange with other late transition metal cations [146]. Thus, in all heterogeneous catalysts, a considerable amount of protons is present. The higher activity of the zeolite catalyst in comparison to the homogeneous catalyst is, therefore, attributed to the presence of Brønsted acid sites with the protons acting as co-catalysts.

To test this, $CF_3SO_3H$ (20 equivalents relative to $Zn^{2+}$) was added to a mixture of $Zn(CF_3SO_3)_2$ and 6AHI [147] (Fig 30). The overall rate of reaction $k$ increased sharply from $0.36 \times 10^{-3}$ to $2.52 \times 10^{-3}$ $min^{-1}$. Whereas $k_1$ and $k_{-1}$ doubled from $2.28 \times 10^{-3}$ to $6.30 \times 10^{-3}$ $min^{-1}$ and $3.19 \times 10^{-3}$ $min^{-1}$ to $5.45 \times 10^{-3}$ $min^{-1}$, respectively, an eight fold increase in $k_2$ was observed (from $1.03 \times 10^{-3}$ to $7.84 \times 10^{-3}$ $min^{-1}$). This clearly shows that protons function as co-catalysts (i) in the hydroamination step (step B) and (ii) in the isomerization of the enamine to the product molecule (step C).

Similar results were obtained for the homogeneous catalyst $[Pd(Triphos)](CF_3SO_3)_2$. Also in this case the cyclization of 6AHI was accelerated by addition of $CF_3SO_3H$ to the

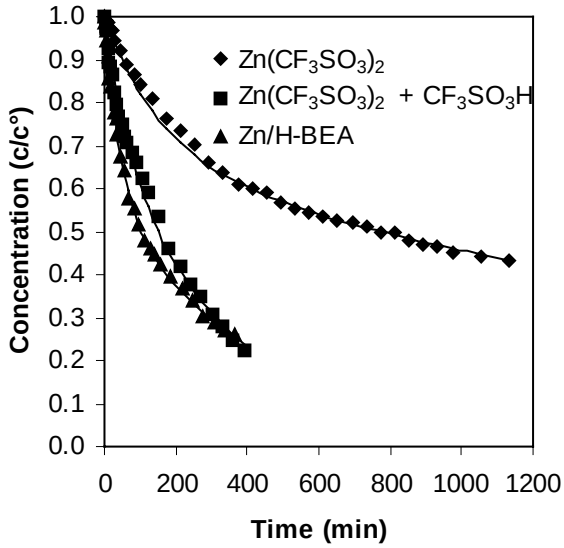


**Fig 30** Cyclization of 6AHI using the heterogeneous catalyst Zn-BEA, the homogeneous catalyst $Zn(CF_3SO_3)_2$ and $Zn(CF_3SO_3)_2$ in the presence of a 20 fold molar excess of $CF_3SO_3H$ (Toluene, 111°C, NIR, s/c 100).

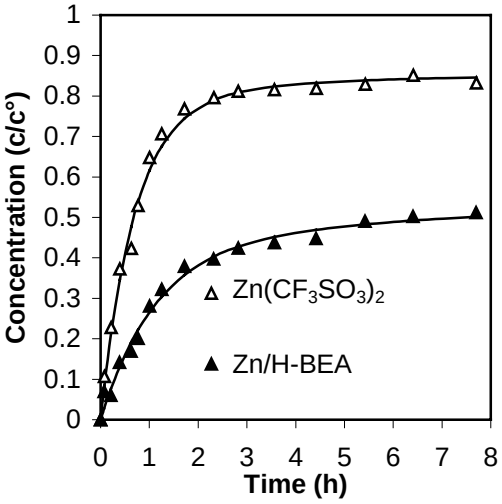


**Fig. 31** Cyclization of 3APE employing the heterogeneous Zn/H-BEA (0.40 Zn/Al) and homogeneous $Zn(CF_3SO_3)_2$ catalysts.

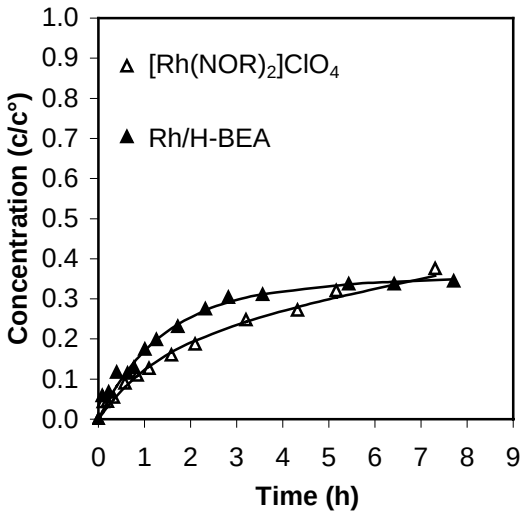


**Fig. 32** Cyclization of 3APE employing the heterogeneous Rh/H-BEA (0.12 Rh/Al) and homogeneous $[Rh(NOR)_2]ClO_4$ catalysts.

catalytic mixture [131]. Therefore, we postulate that Brønsted and Lewis acid sites may be necessary in an ideal hydroamination catalyst. Both sites are present in the ion exchanged BEA catalyst leading to the high catalytic activities observed.

In case of cyclization of 6AHI, Brønsted acid sites had a higher influence on the rate of the isomerization step compared to the hydroamination reaction. Intramolecular hydroamination of 3APE , which contains a CC double bond, yields N,O-acetal tetrahydro-2-methyl-1,3-oxazine. In this case, no subsequent isomerization step can occur. A comparison of the initial reaction rates employing these two starting materials enables us to distinguish the influence of protons on the hydroamination step and on the isomerization step. Therefore, the cyclization of 3APE was studied employing Zn/H-BEA, Cu(I)/H-BEA and Rh(I)/H-BEA in comparison to the homogeneous catalysts $Zn(CF_3SO_3)_2$, $[Rh(NOR)_2]ClO_4$ and $[Cu(CH_3CN)_4]PF_6$. The homogeneous catalyst $Zn(CF_3SO_3)_2$ exhibited a higher catalytic activity compared to the Zn/H-BEA (0.40 Zn/Al) catalyst (Fig. 31). In contrast, for rhodium and copper the heterogeneous catalysts showed a slightly higher initial catalytic activity (Fig. 32, 33). However, the differences in catalytic activity between copper and rhodium based homogeneous and heterogeneous catalysts were small in comparison to the cyclization of 6AHI. In summary, these observations show that in case of cyclization of 3APE protons have much less influence on the rate of reaction compared to the cyclization of 6AHI. These observations confirm that, in the hydroamination of 6AHI protons are involved mainly in the isomerization of the free enamine to the imine product, leading to a faster desorption of the

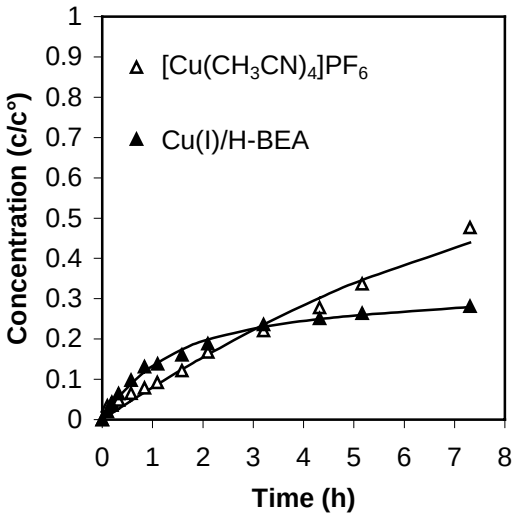


**Fig. 33** Cyclization of 3APE employing the heterogeneous Cu(I)/H-BEA 0.61 Cu/Al and homogeneous $[Cu(CH_3CN)_4]PF_6$ catalysts.

enamine from the metal center. This, in turn leads to an increase in the rate of the metal catalyzed part of the reaction.

To distinguish whether homogeneous or heterogeneous Brønsted acids are more effective co-catalysts it was tested, if the heterogeneous catalyzed reaction could be further accelerated by the addition of a Brønsted acid. Therefore, in case of cyclization of 6AHI, $CF_3SO_3H$ was added to the reaction mixture containing ion exchanged BEA and 6AHI. For the zinc and copper based BEA catalysts the cyclization of 6AHI was not accelerated by the addition of $CF_3SO_3H$ as demonstrated in Fig. 34 and 35. Possible explanations for this observations are (i) that $CF_3SO_3H$ does not enter the pore system, (ii) that already sufficient protons are present in the zeolite pores to achieve maximum reaction rate or (iii) that the mobility of the zeolitic protons along the walls of the pores enables an especially effective co-catalytic function [148]. The more polar environment in the zeolite pores is favorable for polar molecules, such as $CF_3SO_3H$ compared to the solvent toluene.

As $CF_3SO_3H$ is small enough (approximately 4 Å × 3 Å) to enter the 12 ring channel system of the BEA zeolite (7.7 Å × 6.6 Å) it seems unlikely that $CF_3SO_3H$ does not enter the zeolite pores. To increase the catalytic activity of $Zn(CF_3SO_3)_2$ to such an extent that it was similar to the Zn/H-BEA (0.40 Zn/Al) a 20 fold molar excess of $CF_3SO_3H$ was required (equivalents relative to $Zn^{2+}$). For Zn/H-BEA (0.40 Zn/Al) it was shown that approximately 0.25 mmol/g catalytically active zinc and 0.11 mmol/g Brønsted acid sites are present. In a zeolite catalyst the Brønsted acid sites are located inside the pore system and, therefore close

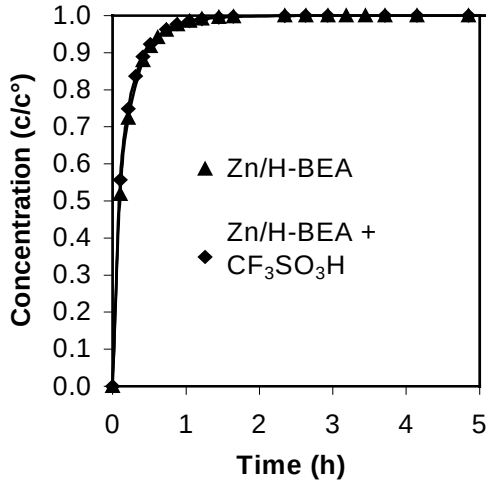


**Fig 34** Cyclization of 6AHI using Zn/H-BEA (0.40 Zn/Al) in the presence of $CF_3SO_3H$ (s/c = 100, c/acid = 1).

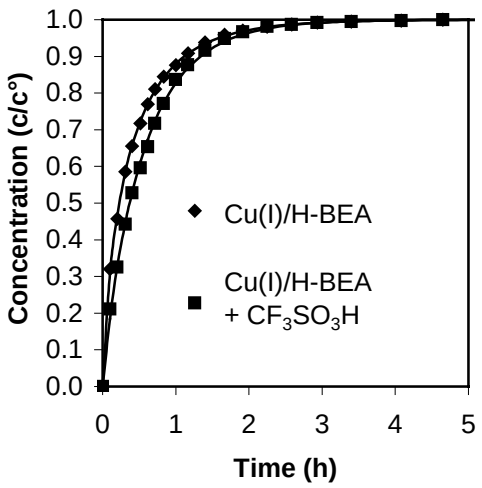


**Fig 35** Cyclization of 6AHI using Cu(I)/H-BEA (0.61 Cu/Al) in the presence of $CF_3SO_3H$ (s/c = 100, c/acid = 0.1).

to the catalytically active metal sites. In contrast employing a homogeneous acid it is diluted in the entire solvent, which results in a significantly larger distance between the metal and the Brønsted acid. Therefore, the zeolitic protons act much more efficiently as co-catalysts and $CF_3SO_3H$ is not able to interact in the mechanistic cycle.

## 3. Conclusions

In contrast to initial expectations, the initial reaction rates in the cyclization of 6AHI were higher when employing the heterogeneous BEA catalyst than for the corresponding homogeneous catalysts. This can be explained by the presence of protons in the ion exchanged zeolites. Similarly, the addition of Brønsted acid to the homogeneous catalyzed reaction led to higher conversion rates. The cyclization of 6AHI is adequately described with a kinetic model based on reversible hydroamination of 6AHI, followed by an effectively irreversible isomerization of the enamine to the imine product. It was shown that the former step required the presence of a metal catalyst, whereas the latter step was catalyzed by protons. However, the metal catalyzed hydroamination cycle was also faster in acidic reaction media. Additionally, it was shown that zeolitic protons act much more efficiently as co-catalysts than homogeneous Brønsted acids. For the latter case the dilution in liquid is responsible for the less effective co-catalysis. In summary, these results show that Brønsted and Lewis acidic groups in close vicinity may be necessary in an ideal catalyst for hydroamination reactions.

## VI Conclusions

The cyclizations of 6-aminohex-1-yne (6AHI) and 3-aminopropylvinylether (3APE), as well as the reaction between phenylacetylene and aniline, were studied as model reactions for the direct addition of amine N–H to CC multiple bonds (hydroamination). Based on the knowledge on homogeneous hydroamination catalysts a heterogeneous catalyst system was developed for these reactions. $Rh^{+}$, $Cu^{+}$, and $Zn^{2+}$ immobilized on heterogeneous supports like zeolites or silicate were especially suitable as catalytically active metal centers. The corresponding ion exchanged BEA zeolites displayed a significantly higher activity in the cyclization reactions compared to other catalyst systems. A small but not negligible activity of the parent H-BEA zeolite in the conversion of 6AHI and 3APE was explained by leaching of aluminum into the toluene phase. For Zn/H-BEA it was shown that this high activity is not related to leaching of zinc into the liquid phase. It is concluded that the high activity is related to, on the one hand, the higher Lewis acid strength, which decreases in the sequence Zn/H-BEA > $ZnO/SiO_2$ > ZnO and, on the other hand, to properties of BEA zeolites. In respect to the latter it was shown that the preferred cation exchange positions are located in highly accessible parts of the BEA channel system. In addition, the high polarity of the outer surface leads to an increased concentration of reactants in the pore system relative to the bulk liquid phase. The reaction between phenylacetylene and aniline served as a model for an intermolecular hydroamination reaction. In comparison to the intramolecular, the intermolecular reaction was much slower. This is related to the less favorable thermodynamics of the reaction, especially to the unfavorable reaction entropy. However, it was demonstrated that, in principle, a zeolite catalyst system is suitable.

The influence of the metal loading on the catalytic activity was examined for Zn/H-BEA zeolites. Depending on the zinc loading up to three different zinc sites were found in zeolite BEA. The most stable zinc site is formed by exchange of zinc on close aluminum pairs, i.e., two tetrahedral framework aluminums in vicinity. In H-BEA the corresponding pairs of Brønsted acid sites are thermally unstable. Upon thermal treatment, the high local positive charge on the hydrogen is reduced by rearrangement of the framework and formation of Lewis acid sites. The coordination of a divalent cation increases the stability of close aluminum pairs and latter were identified as the preferential sites for zinc exchange. The close neighborhood of two negatively charged oxygen atoms is necessary for balancing the charge of a divalent cation, leading to an energetically favorable local environment around $Zn^{2+}$. When all close aluminum pairs are covered, the concentration of a second zinc species increases sharply, indicating that this site is the next preferred zinc exchange location. This

zinc species is made of two zinc cations exchanged on nearby aluminum sites balanced by the divalent charge of an oxygen bridge. These two zinc species are formed at low ion exchange degrees in the range 0 – 0.30 Zn/Al. At higher zinc loading (≥ 0.30 Zn/Al) a third site, probably neutral ZnO on the outer surface, is formed. It was found that the reactivity of zinc is directly related to its location in the structure. The initial rates of reaction increased linearly with the zinc contents (< 0.33 Zn/Al), whereas further increase of the zinc contents (0.33 > Zn/Al > 0.77) did not lead to a higher catalytic the activity of the material. This proves that, in order to exhibit catalytic activity, zinc must be coordinated to Brønsted acid sites. The combination of EXAFS and structure simulation indicated that (i) the zinc cations preferentially coordinate to six membered oxygen rings and (ii) the aluminum pairs are preferentially located in six membered rings. Thus, it seems most likely that zinc is located on that side of the six membered rings, which faces in the main channel system and, therefore, is readily accessible for reactant.

By mechanistic studies, employing *in situ* $^{1}$H-NMR, $^{31}$P-NMR, EXAFS/XANES and NIR / UV-spectroscopy, we were able to confirm a mechanism for hydroamination reactions on late transition metal catalysts. From the EXAFS/XANES studies performed we were able to exclude an oxidative addition pathway for our catalyst systems. The most likely mechanism is initiated by coordination of the unsaturated carbon-carbon bond to the metal center followed by subsequent nucleophilic attack of the amine functionality. $^{31}$P-NMR spectroscopy confirmed the rate determining step in the metal catalyzed part of the reaction. This was assigned to the subsequent [1,3] - hydrogen shift reaction. Co-catalysis by Brønsted acid sites was shown to accelerate this rate limiting reaction as shown by NIR- and UV-spectroscopy. In case of cyclization of 6AHI the isomerization reaction from the enamine to the imine product was found to be also catalyzed by protons. However, both parts of the reaction are independent from each other.

The influence of different transition metals on heterogeneous and homogeneous catalyzed reactions was studied in the cyclization of 6AHI and 3APE. Zinc, copper, and rhodium exchanged BEA exhibited high initial reaction rates, also in comparison to the corresponding homogeneous catalyst systems. This was assigned to the presence of Brønsted acid sites in the BEA catalysts, which act as co-catalysts. In this respect it was proven that hydroamination is not catalyzed by pure Brønsted acids. In summary, the simultaneous presence of Lewis and Brønsted acid sites and their co-catalytic function are the reason why transition metal exchanged BEA zeolites are excellent catalysts for hydroamination reactions.

# VII Experimental

## 1. IR spectroscopy

IR spectroscopy was performed on a Bruker FTS 88 spectrometer with using MCT detector. The spectra were taken in a vacuum cell equipped with $CaF_2$ windows and connected to a dosing system operating in a pressure range of $10^{-3}$ – 1 mbar. The samples were prepared as self supporting wavers of approximately 10 mg/cm$^2$ weight. The spectra were recorded with a resolution of 4 cm$^{-1}$. The zeolite samples were activated *in situ* (RT-450°C 10°C/min; 1 h at 450°C) at $10^{-4}$ mbar prior to adsorption. Before adsorption, liquids were degassed by freeze thaw cycles. Acetonitrile-$d_3$ was adsorbed at $10^{-1}$ mbar at 35°C for 15 min. Pyridine was adsorbed at $10^{-2}$ mbar at 100°C for 1 h. Spectra were recorded after outgassing the samples for 1 h and, in case of pyridine adsorption, also after outgassing at 450°C (RT - 450°C 10°C/min). Deuterium oxide (Aldrich) was adsorbed at a partial pressure of $5 \times 10^{-1}$ mbar at 100°C, followed by outgassing at 400°C (100 - 400°C 10°C/min). All spectra were analyzed using Grams (Version 5.10). The spectra were normalized to the intensities of the skeletal vibrations in the region between 2115 and 1753 cm$^{-1}$. Difference spectra were calculated by subtracting the spectra of the activated zeolite from the spectra of the zeolite with adsorbed probe molecules. For acetonitrile-$d_3$ adsorption, the difference spectra were baseline corrected in the region of the CN vibrations (2350 - 2200 cm$^{-1}$). The intensity of each individual band was obtained by using a deconvolution routine (0.5 Gaussian and 0.5 Lorentzian curves).

## 2. Temperature programmed desorption (TPD)

The TPD experiments were performed in a custom built apparatus consisting of a quartz sample tube connected to a vacuum system separated from the pump by a liquid nitrogen trap. About 80 - 100 mg sample was placed in the quartz tube as powder. The sample tube was heated uniformly by an electrical oven. A constant fraction of the desorbing molecules enter the mass spectrometer part *via* a leak valve. Regulation of the pressure in the mass spectrometer to around $2 \times 10^{-7}$ mbar and standard measurements of well characterized samples ensured reproducibility. The setup includes a dosing system by which probe molecules are introduced in a pressure range from $10^{-3}$ – 10 mbar.

Before adsorption, the samples were activated by heating to 450°C (10°C/min) for 1 h in vacuum (p=$10^{-4}$ mbar). The probe molecules acetonitrile (Aldrich), ammonia (Aldrich) and iso-propylamine (Aldrich) were adsorbed at 1 mbar for 10-15 min at the temperatures stated.

Subsequently, the samples were outgassed in vacuum for 1.5 h, 1.5 h and 3 h, respectively. The temperature programmed desorption was performed by heating the samples to 650°C with a temperature ramp of 10°C/min. The rate of molecules desorbing was monitored by mass spectroscopy. The resulting MS-signals were normalized to the sample mass and the data series analyzed using m/e = 16 for ammonia, 41 for acetonitrile, 41 for propene, 44 for iso-propylamine.

### 3. Microbalance experiments

Microbalance experiments were performed on a modified microbalance (Setaram). The sample crucible was filled with parts of self supporting wavers from the parent zeolites of about 15-20 mg total weight. The microbalance is connected to a dosing system, by which probe molecule pulses of around 10 mbar can be introduced. The sample chamber contains a heating system which allows activation and temperature programmed desorption of the adsorbed molecules up to 600°C. Desorbing molecules were detected by a connected mass spectrometer. The signal intensities were calibrated on the mass of probe molecules adsorbed. Before adsorption, the samples were activated in vacuum ($10^{-4}$ mbar) by heating to 450°C (10°C/min) for 1 h. Adsorption of probe molecules was performed at 1 mbar at the temperatures stated (10-15 min), followed by outgassing in vacuum for 1-3 h. The equilibration of adsorption and outgassing was followed gravimetrically.

### 4. Structure simulation

A cluster consisting of 35 T-atoms (terminated with -OH groups) was isolated from the crystallographic structure of zeolite BEA and used to calculate energetic contributions and the geometry and of $Zn^{2+}$ cations at different ion exchange position of BEA using density functional theory method (DFT). The cluster chosen was sufficiently large to allow the use the same cluster for all ion exchange positions investigated in order to avoid artifacts due to a different cluster size used in the individual calculations. The geometry was optimized with respect to the energy calculated using a double numerical basis set and after geometry optimization was achieved the final energy was calculated using the exchange correlation based on the Becke, Lee, Yang Parr (BLYP) functional. The program DMol3 was used for the theoretical calculations [149].

$Zn^{2+}$ cations were located at 4-MR, 5-MR and 6-MR positions and for each of the geometries two $Si^{4+}$ atoms were replaced by $Al^{3+}$ to maintain the neutral charge of the cluster. To account for the different energies for the substitution of $Al^{3+}$ into the three positions (4-MR, 5-MR and 6-MR) the charge was balanced with two protons end the energy was

calculated for each of the geometries. The stability of the $Zn^{2+}$ cations was determined from the exchange energy according to [150]:

$$E(exch)_{pos\ n\text{-}MR} = E(Zn\text{-}BEA)_{pos\ n\text{-}MR} - E(H\text{-}BEA)_{pos\ n\text{-}MR}$$

where $E(Zn\text{-}BEA)_{pos\ n\text{-}MR}$ is the energy of the $Zn^{2+}$ containing cluster and $E(H\text{-}BEA)_{pos\ n\text{-}MR}$ of the cluster with two charge balancing protons.

## 5. $^{27}$Al NMR spectroscopy

$^{27}$Al-MAS-NMR were measured on a *Bruker MSL-300* NMR spectrometer at a field strength of 7.5 T and 8 - 15 kHz spinning frequency. The samples were dried at 100°C and pressed into 4 mm $ZrO_2$-rotors. Spectra were taken at a frequency of 78.205 MHz with 1.0 µs excitation pulses and 0.1 s recycle times. The $^{27}$Al chemical shifts were referenced to solid $Al(NO_3)_3$ ($\delta$ = 0.0 ppm).

## 6. Ion exchange

Nickel(II)-, platinum(II)-, palladium(II)-, copper(II)-, zinc(II)-exchanged zeolites were made by repeated ion exchange of the protonic form of the corresponding zeolites. The $SiO_2/Al_2O_3$ ratio specifies by the producer were 25, 18 and 5.1 for H-BEA, H-Mor and H-Y, respectively. In a typical procedure, the ion exchange was performed in a water solution of metal salt at 80°C. The zeolite was separated by centrifugation (5000 rpm, 20 min) and, to obtain a certain ion exchange degree, the procedure was repeated several times. This procedure was followed by calcination in a flow of air (100 ml / min) and, for Ni-BEA, by reduction with $H_2$.

Copper(I) and rhodium(I) zeolites were prepared using a different method since, upon heating, copper(I) and rhodium(I) salts are susceptible disproportionation. Thus, the parent H-BEA zeolite was activated by heating to 150°C in vacuum (10 mbar) and ion exchanged by stirring the activated zeolite in an $CH_3CN$ solution (40 cm3, 82°C, 12 h) of the complexes $[Rh(NOR)_2]ClO_4$ (0.1 g, NOR = norbornadiene) or $[Cu(CH_3CN)_4]PF_6$ (1.5 g). The final catalysts were obtained by removing the solvent under vacuum and the sample maintained in an inert atmosphere. In case of lanthanum exchange the parent material was ground with $LaCl_3 \times 7\ H_2O$ in an agate ball mill for 30 min. The ground mixture was heated in a stream of air (100 ml/min, RT – 120°C 2°C/min; 120°C 2 h; 120 – 500°C 2°C/min). The sample was washed and dried at 100°C. The exact procedure used for the ion exchange and the results of the chemical analysis (AAS and BET) are summarized in the appendix (table 1 and 2).

Ammonia exchanged BEA zeolites were obtained by ion exchange of H-BEA in an aqueous solution of $NH_4NO_3$ (1 M, 80°C) for 12 h. The modified zeolite was separated by

centrifugation (5000 rpm, 20 min), washed several times with distilled water and dried at 100°C.

## 7. Catalytic experiments

In a typical experiment for testing the catalytic activity, metal exchanged zeolites ($5.3 \times 10^{-3}$ mmol $M^{n+}$, if not stated otherwise) were activated at 200°C in vacuum (10 mbar) for 12 h. The Cu (I) – and Rh (I) -zeolites were used in an inert atmosphere without activation. Dry toluene (15 $cm^3$) was added, the mixture heated to reflux temperature (111°C) and the catalytic reaction started by addition of starting materials (0.53 mmol, if not stated otherwise). During the reaction, samples were taken for GC-analysis. Samples containing heterogeneous catalyst were centrifuged for 10 min at 14000 rpm before analysis.

The technical parameters of the analytical gas chromatography is given in 2.3 and the temperature programs used and the resulting $R_F$ values of products and starting materials are summarized in the appendix (table 3). Calibration standards containing 0.1, 0.2, 0.3 and 0.4 vol% of each component were used for calibration.

*In situ* observation of the reactions was carried out in custom built 100 or 120 $cm^3$ steel autoclaves [151]. Both reactors were equipped with quartz probes for *on line* UV- and NIR-spectroscopy. The probes were connected with optical fibres to a Perkin Elmer Lambda 16 UV- and a Bruker Vector 22/N NIR-spectrometer, respectively.

All kinetic measurements were performed according to the following procedure: A solution of the catalyst in the appropriate solvent was introduced into the reactor. The mixture was stirred and heated to the desired temperature. The reaction was then started by introducing a solution of the substrate from a sample loop with known volume into the reactor. The amount of catalyst and 6AHI, the solvent and the reaction conditions employed in the experiments are summarised in Table 4 (appendix).

The program OPUS was used to analyse the spectra [152]. After base line correction (NIR), the spectra were integrated. The reaction was performed in toluene (suitable solvent for hydroamination reactions.[153]. Toluene showed a strong absorption in the UV-region and the reaction could only be followed with NIR-spectroscopy. The substrate 6AHI had an absorption maximum at 208 nm (due to the C–N $n \rightarrow \sigma^*$ transition) with a weak shoulder extending to 320 nm. The product 2-methyl-1,2-dihydropiperidine had an absorption maximum at 220 nm (due to the C=N $\pi \rightarrow \pi^*$ transition) and an additional absorption maximum at 305 nm (due to the C=N $n \rightarrow \pi^*$ transition). The latter absorption maximum was used to follow the concentration of the product with UV spectroscopy, performing the quantitative analysis of 2-methyl-1,2-dihydropiperidine in the region 220-370 nm.

The parameters α, β and k of the model (see text below) were fitted to the experimentally determined concentrations using the solver module of Excel [154].

## 8. Synthesis and characterization of starting materials and products

$^{1}H$ $^{13}C\{^{1}H\}$ and $^{31}P$ NMR spectra were recorded on a Bruker AM 400 instrument and referenced in ppm relative to the solvent shift [155] or tetramethylsilane. GC analyses were performed on a Hewlett-Packard HP 5890 gas chromatograph equiped with a crosslinked 5% diphenyl- 95 % dimethyl-polysiloxane column (30 m, Restek GmbH, Rtx-5 Amine) and a flame ionisation detector. ). He was used as carrier gas with a column head pressure of 10 psi. GCMS analyses were performed on a Hewlett-Packard HP 5890 gas chromatograph equiped with a crosslinked 5% diphenyl- 95 % dimethyl-polysiloxane column (30 m, Restek GmbH, Rtx-5 Amine) and a mass selective detector HP 5971A (Hewlett- Packard). IR spectra were obtained on a Perkin-Elmer FT-IR 2000 spectrometer as KBr pellets. Mass spectroscopic analyses were performed on a Finnigan MAT 311A mass spectrometer by chemical ionization (CI).

### *8.1 Synthesis and characterization of 6AHI*

The compound 5-cyanopent-1-yne (25.0 g, 0.269 mol) was dissolved in $Et_2O$ (100 $cm^3$) and added over a period of 60 minutes to a magnetically stirred mixture of $LiAlH_4$ (11.0 g, 0.289 mol) in $Et_2O$ (400 $cm^3$) at 0°C. The mixture was refluxed overnight, the excess $LiAlH_4$ destroyed by addition of $H_2O$ (75 $cm^3$), the mixture filtered, and the organic layer separated. The $Et_2O$ was removed to yield a yellow liquid. Addition of HCl (1M in $Et_2O$, 300 $cm^3$, 0.300 mol) precipitated the product as the hydrochloride, which was filtered off and dried in vacuum. The hydrochloride (23.3 g) was dissolved in methanol (100 $cm^3$), $Na_2CO_3$ (18.5 g, 0.175 mol) added, and the mixture stirred at room temperature for 1h. The solvent was removed and the product destilled (69-70°C at 18 mm) [156].

Yield: 11,1 g, 43 %. $^{1}H$ NMR ($CDCl_3$): δ 2.74 (t, 2H, H6), 2.21 (m, 2H, H3),1.95 (t, 2H, H1), 1.58 (m, 4H, H4-5), $^{13}C\{^{1}H\}$ NMR ($CDCl_3$): δ 85.0 (C2), 69.0 (C1), 42.2 (C6), 33.3 (C5), 26.4 (C4),18.8 (C3), GC: $R_F$ 1.214

### *8.2 Synthesis and characterization of 2-methyl-1,2-dehydropiperidine*

The catalyst $Zn(CF_3SO_3)_2$ (0.03 g, 0.088 mmol) was dissolved in toluene (50 $cm^3$), magnetically stirred and heated to reflux temperature. The reaction was started by addition of 6-aminohex-1-yne (1.01 g, 8.8 mmol) and the mixture was refluxed overnight. GC analysis of the reaction mixture was performed whether 100 % conversion of 6AHI was obtained. Addition of HCl (1M in $Et_2O$, 9.0 $cm^3$, 9.0 mmol) precipitated the product as the hydrochloride, which was filtered off and dried in vacuum. The hydrochloride of the product

was characterized using GC and NMR spectroscopy and confirmed as 2-methyl-1,2-dehydropiperidine.

Yield: 0.45 g, 53 %. $^{1}$H NMR ($CD_3OD$): δ 4.86 (s, 1H, $NH^+$), 3.63 (t, 2H, $^{3}$J=4 Hz, $CH_2$-$N^+$), 2.80 (m, 2H, $CH_2$-C=N), 2.39 (s, 3H, $CH_3$), 1.86 (m, 4H, $CH_2CH_2$), $^{13}C\{^{1}H\}$ NMR ($CD_3OD$): δ 164.4 (C2), 27.3 (C3), 21.5 (C4), 30.3 (C5), 49.0 (C6), GC: $R_F$ 1.264.

*8.3 Synthesis and characterization of N-(methyl-benzylidene)-aniline*

The catalyst $Zn(CF_3SO_3)_2$ (0.004 g, 0.01 mmol) an the compound aniline (0.009 g, 0.1 mol) were dissolved in toluene (180 $cm^3$), magnetically stirred and heated to reflux temperature. The reaction was started by addition of phenylacetylene (0.004 g, 0.04 mol) and the mixture was refluxed overnight. GC analysis of the reaction mixture was performed whether 100 % conversion of phenylacetylene was obtained. The product was separated by column chromatography using hexane/ethyacetate 50/30 as solvent and silica gel 60 as stationary phase. The solvents were evaporated and the single product (white powder) was characterized using NMR, MS (CI), GC-MS and IR analyses and confirmed as N-(methyl-benzylidene)-aniline.

Yield: 1.3 g, 16.7 %. $^{1}$H NMR ($CDCl_3$): δ 6.7-8 (m, 10H, Ph), 2.2 (s, 3H, $CH_3$), $^{13}C\{^{1}H\}$ NMR ($CDCl_3$): δ 164.5 (C=N), 151.7 (N-C), 139.5 (Ph), 130.5 (Ph), 129.0 (Ph), 128.4 (Ph), 127.2 (Ph), 123.3 (Ph), 119.4 (Ph), 115.1.0 (Ph), IR: 3054 (m), 1630(vs), 1591 (vs), 1446 (s), 1214 (s), 761 (s), 693 (vs), 572 (w), 528 (w), GC: RT 29.239 min GCMS: $R_F$ 8.241 *m/z* 180 ($M^+$-$CH_3$), MS (CI) *m/z* 195 ($M^+$).

A reference compound was synthesized using the addition of aniline (29.4 g, 0.3 mol) to acetophenone (25.36 g, 0.25 mol) in toluene (50 $cm^3$) catalyzed by $CF_3SO_3H$ (0.03 g, 0.2 mmol) at reflux temperature (12 h). The reaction mixture was dried over $MgSO_4$ and distillated (110°C, 30 mm, product fraction). The product was recrystallized from hexane and analyzed using IR and NMR spectroscopy. The spectra obtained confirmed N-(methyl-benzylidene)-aniline as product of the hydroamination of phenylacetylene with aniline.

## 9. In situ X-ray Adsorption Spectroscopy

*In situ* observation of the oxidation state on zinc copper and palladium based catalysts was performed by X-ray absorption spectroscopy. The spectra were collected at the beam-line X1 at the HASYLAB, DESY Hamburg. A Si (111) monochromator was used and the intensity of incident and transmitted X-rays were recorded using ionization chambers. Energy calibration was performed by measuring a zinc, copper or palladium foil, located between the second and third ionization chamber simultaneously, during all experiments. All samples were calculated to achieve a total absorption of $\mu x = 2.5$. The catalysts were dissolved (dispersed)

in $CH_3CN$ and the reaction started by addition of 6AHI. After approximately10 min the reaction mixture was transferred to a purpose build Teflon tube and frozen in liquid nitrogen. The conversion obtained was determined by GC analysis and reached approximately 5 – 10 %. The Teflon tube was placed in a sample holder equipped with a cooling system and spectra were taken at liquid nitrogen temperature. Spectra were recorded from the catalysts dissolved (dispersed) in $CH_3CN$ before and after the addition of 6AHI. Additionally, spectra were taken from reference materials as the untreated catalysts or metal oxides and metal foil. These measurements were performed from self supporting wavers or wavers prepared from solid and polyethylene. The wavers were placed in a sample holder equipped with a heating and cooling system, which allowed activation up to 450°C, as well as cooling to liquid nitrogen temperature. The sample holder was placed in a stainless steel reactor containing Kapton windows and a gas inlet and outlet system. The gas flow rates inside the reactor were regulated using an electronic gas flow meter. Activation was performed by heating the sample to 450°C (10°C/min) for 1 h in He with a flow of 65 ml/min.

The analysis was performed using Winxas (Version 2.0) [157]. The spectra were calibrated to the energy using the first inflection point of the K-edge from the simultaneously measured metal foil. Background correction and normalization were performed by fitting the pre-edge region with a $2^{nd}$ order polynom the section above the edge by a polynomial spline with seven nodes. The oscillations were weighted with $k^2$ and Fourier transformed in the range k = 2.1 – 16 $Å^{-1}$.

The local environment of the zinc atoms was determined from the EXAFS using phase-shift and amplitude functions for Zn-O and Zn-Zn resulting from multiple scattering FEFF calculations (Version 8.10) [158] on a ZnO cluster.

## VIII Literature


[1] Roundhill, D. M. *Chem. Rev.* **1992**, 91, 1.

[2] Roundhill, D. M. *Cat. Today*, **1997**, 92, 1-27.

[3] Müller, T. E. and Beller, M. *Chem. Rev.*, **1998**, 98, 675-703.

[4] Penzien, J.; Müller, T. E.; Lercher, J. A. *Microp. Mesop. Mater.* **2001,** *48*, 285.

[5] Van Nhu, N.; Müller, T. E.; Lercher, J. A.**,** *AIChE Journal***,** accepted for publication.

[6] Penzien, J; Müller, T. E.; Lercher, J. A. *J. Am. Chem. Soc.* **2002**, manuscript in preparation.

[7] Eller, K.; Kummer, R.; Stops, P. Process for Producing Amines from Olefins on Zeolites of Types, **1995,** SSZ-26, SSZ-33, CIT-1 of Mixtures Thereof, WO 97/21661 and Dingerdissen, U.; Kummer, R.; Stops, P.; Müller, U.; Herrmann, J. and Eller, K.

Method of Preparing Amines from Olefins over Boron β-Zeolites, **1996**, WO 97/07088.

[8] Richmond, M. K.; Scott, S. L.; Alper, H *J. Am. Chem. Soc.* **2001**, 123, 10521.

[9] Breuer, K.; Teles, J. H.; Rieber, N.; Demuth D. and Hibst H. Verfahren zur Herstellung von Iminen und Enaminen und gegebenenfalls deren Weiterhydrierung zu Aminen, DE, **1998**,198 36 814.

[10] Straub, T.; Haskel, A.; Neyroud, T. G.; Kapon, M.; Botoshansky, M.; Eisen M. S. *Organometallics* **2001**, 20, 5017.

[11] Dash, A. K.; Wang, J. Q.; Eisen, M. S. *Organometallics* **1999**, 18, 4724.

[12] Li, Y.; Marks, T. J. *J. Am. Chem. Soc.* **1996**, 118, 9295.

[13] Hartung, G. C.; Tillack, A.; Trauthwein, H.; Beller, M. *J. Org. Chem.* **2001**, 66, 6339

[14] Beller, M. and Breindl, C. *Tetrahedron*, **1998**, 6359.

[15] Shi, Y.; Ciszewski, J. T.; Odom, A. L. *Organometallics* **2001**, 20, 5011.

[16] Molander, A. G.; Dowdy, E. D.; Pack, S. K. *J. Org. Chem.* **2001**, 66, 4344.

[17] Haak, E.; Bytschkov, I. and Doye, S. *Angew. Chem. Int. Ed.*, **1999,** 38, 3389.

[18] Molander G. A. and Dowdy E. D. *J. Org. Chem.*, **1999,** 63, 8983.

[19] Bürgstein, M. R.; Berberich H. and Roesky, P. *Organometallics*, **1998,** 17, 1452.

[20] Blomberg, M. R. A.; Siegbahn, P. E. M.; Svensson, M. *Inorg. Chem.* **1993**, 32, 4218.

[21] Tokunaga, M.; Eckert, M. and Wakatsuki, Y. *Angew. Chem. Int. Ed.*, **1999**, 3222.

[22] Beller, M.; Trauthwein, H.; Eichberger, M.; Breindl, C. and Müller, T. E. *Eur. J. Inorg. Chem.*, **1999,** 1121.

[23] T. E. Müller, M. Grosche, E. Herdtweck, A.-K. Pleier, E. Walter, Y.-K. Yan, *Organometallics*, **2000**, *19*, 170.

[24] Uchimaru, Y. *J. Chem. Soc., Chem. Comm.*, **1999,** 1133.

[25] Burling, S.; Field, L. D. and Messerle, B. A. *Organometallics*, **2000,** 19, 87.

[26] Dorta, R.; Egli, P.; Zürcher, F. and Togni, A. *J. Am. Chem. Soc.*, **1997** 119, 10857.

[27] Kadota, I.; Shibuya, A.; Lutete, L. M. and Yamamoto, Y. *J. Org. Chem.*, **1999,** 64, 4570.

[28] Casalnuovo, A. L.; Calabrese, J. C. and Milstein, D. *J. Am. Chem. Soc.*, **1988**, 110, 6738.

[29] Beller, M.; Trauthwein, H.; Eichberger, M.; Breindl, C.; Herwig, J.; Müller, T. E. and Thiel, O. R. *Chem. Eur. J.*, **1999** 5, 1306.

[30] Deubel, D. V.; Ziegler, T. *Organometallics,* **2002**, 21, 1603.

[31] Beller, M.; Thiel, O. R.; Trauthwein, H.; Hartung, C. G. *Chem. Eur. J.* **2000**, 6, 14, 2513.

[32] Kadota, I.; Shibuya, A.; Lutete, L. M.; Yamamoto, Y. *J. Org. Chem.* **1999**, 64, 4570.

[33] Kawatsura, M.; Hartwig, J. F. *Organometallics*, **2001**, 20, 1960.

[34] Löber, O.; Kawatsura, M.; Hartwig, j. F. *J. Am. Chem. Soc.* **2001**, 123, 4366.

[35] Löber, O.; Kawatsura, M.; Hartwig, j. F. *J. Am. Chem. Soc.* **2000**, 122, 9546.

[36] A. Chauvel, B. Delmon, W. H. Hölderich, Appl. Catal., 115 (1994) 173.

[37] W. Hölderich, M. Hesse, F. Naumann, Angew. Chem. Int. Ed. Eng., 27 (1988) 226.

[38] M. Lequitte, F. Figueras, C. Moreau, S. Hub, *J. Catal.*, **1996**, *163*, 255.

[39] N. Mizuno, M. Tabata, T. Uematsu, M. Iwamoto, *J. Catal.*, **1994**, *146*, 249.

[40] Haw, J. F.; Nicholas, J. N.; Song, W.; Deng, F.; Wang, Z.; Xu, T.; Heneghan, C. S. *J. Am. Chem. Soc.* **2000**, *122*, 4763.

[41] Maxwell, I. E.; Stork W. H. J.; in: van Bekkum, H.; Flanigen, E. M.; Jansen, J. C. (Eds.) *Studies in Surface Science and Catalysis* Elsevier Amsterdam, **1991**,Vol. *58*, 571.

[42] Borreto, L.; Camblor, M. A.; Corma, A.; Perez-Pariente A. *J. Appl. Catal.* **1992**, *82*, 37.

[43] Jansen, J. C.; Creyghton, E. J.; Njo, S. L.; van Koningsveld, H.; van Bekkum, H. *Catal. Today* **1997**, *38*, 205.

[44] Jansen, J. C.; Creyghton, E. J.; Njo, S. L.; van Koningsveld, H.; van Bekkum, H. *Catal. Today* **1997**, *38*, 205.

[45] Pandey, P. A.; Singh, A. P. *Catal. Lett.* **1997**, *44*, 129.

[46] Ma, Y.; Wang, Q. L.; Jiang, W.; Zuo, B. *Appl. Catal. A.* **1997**, *165*, 199.

[47] Djakovitch, L.; Koehler, K. *J. Am. Chem. Soc.* **2000**, *132*, 5990.

[48] Biscardi, J. A.; Meitzner, G. D.; Iglesia E. *J. Catal.* **1998**, *179*, 192.

[49] Ono, Y. *Catal. Rev. Sci. Eng.* **1992**, *34*, 179.

[50] Penzien, J.; Müller, T. E.; Lercher, J. A. *Microp. Mesop. Mater.* **2001,** *48*, 285.

[51] Hagen, A.; Roessner, F. in: Krager, H. G.; Weitkamp, J. (Eds.) *Studies in Surface Science and Catalysis* Elsevier Amsterdam, **1999**,Vol. *98*, 189.

[52] Onyesták, G. Y.; Kalló, D. in: Delmon, B.; Froment, G. F. (Eds.) *Studies in Surface Science and Catalysis* Elsevier Amsterdam, **1987**,Vol. *34*, 605.

[53] Onyesták, G. Y.; Papp, J.; Kalló, D. in: Karge, H. G.; Weitkamp, J. (Eds.) *Studies in Surface Science and Catalysis* Elsevier Amsterdam, **1989**,Vol. *46*, 241.

[54] Senger, S.; Radom, L. *J. Am. Chem. Soc.* **2000**, *122*, 2613.

[55] Treacy, M. M. J.; Newsam, J. M. *Nature* **1988**, *332*, 249.

[56] Higgins, J. B.; LaPierre, R. B.; Schlenker, J. L.; Rohrmann, A. C.; Wood, J. D.; Kerr, G. T.; Rohrburg, G. J. *Zeolites* **1986**, *8*, 446.

[57] Jansen, J. C.; Creyghton, E. J.; Njo, S. L.; van Koningsveld, H.; van Bekkum, H. *Catal. Today* **1997**, *38*, 205.

[58] Borade, R. B.; Clearfield, A. *J. Phys. Chem.* **1992**, *96*, 6729.

[59] Kirisci I.; Flego, C.; Pazzuconi, G.; Parker, W. O., Jr.; Millini, R.; Perego, C.; Bellussi G. *J. Phys. Chem.* **1994**, *98*, 4627.

[60] van Bokhoven, J. A.; Koningsberger, D. C.; Kunkeler, P.; van Bekkum, H.; Kentgens, A. P. M. *J. Am. Chem. Soc.* **2000**,*122*, 12842.

[61] Jentys, A.; Lercher, J. A. *Stud. Surf. Sci. Catal.* **2001**, 137, 345

[62] Gorte, R. J. *Catal. Lett.* **1999**, *62*, 1.

[63] Karra, M. D.; Sutovich, K. J.; Mueller, K. T. *J. Am. Chem. Soc.* **2001,**

[64] Turro, N. J.; Lei, X.;Li, W.; Liu, Z.; Ottaviani, M. F. *J. Am. Chem. Soc.* **2000**, *122*, 12571.

[65] Miyamoto, Y.; Katada, N.; Niwa, M. *Microp. Mesop. Mater.* **2000**, *40*, 271.

[66] Stockenhuber, M.; Lercher, J. A. *Micropor. Mater.* **1995**, *3*, 457.

[67] Kuehl, G. H.; Timken, H., K. C. *Microp. Mesop. Mater.* **2000**, *35-36*, 521.

[68] Bortnosvsky, O.; Sobalík, Z.; Wichterlová, B. *Microp. Mesop. Mater*. **2001**, 46, 265.

[69] Barbosa, L. A. M. M.; van Santen, R. A. *Catal. Lett*. **1999**, *63*, 97.

[70] Eubanks, J. R. I.; Sims, L. B.; Fry, A. *J. Am. Chem. Soc.* **1991**, *113*, 8821.

[71] Bourns, A. N.; Frosst, A. C. *Can. J. Chem.* **1970**, *48*, 133.

[72] Kirby, A. J.; Logan, C. L. *J. Chem. Soc., Perkin Trans. II* **1978**, 642.
[73] Bourgeat-Lami, E.; Massiani, P.; Di Renzo, F.; Espiau, P.; Fajula, F. *Appl. Cat.* **1991,** 72, 139
[74] Jähnchen, J.; Peeters M. P. J.; van Wolput, J. H. M. C.; Wolthuizen, J. P.; Lohse, U.; van Hoof, J. H. C. *J. Chem. Soc. Faraday Trans.* **1994**, *90(7)*, 1033.
[75] Desiraju, G. R.; Steiner, T. *The Weak Hydrogen Bond* **1999**, Oxford Science Publication, 51.
[76] Palmenschikov, A. G.; van Santen, R. A.; Jänchen, J.; Meijer, E. *J. Phys. Chem.* **1993**, *97*, 11071.
[77] Wichterlová, B.; Tvarůžková, Z.; Sobalík, Z.; Sarv, P. *Microp. Mesop. Mater.* **1998**, *24*, 223.
[78] Kiricsi, I.; Pazzuconi G.; Parker, W. O. Jr.; Millini, R.; Perego, C.; Bellussi, G. *J. Phys. Chem.* **1994**, *98*, 4627.
[79] Kunzl, V.; *Collect. Czech. Chem. Commun.* **1932**, *4,* 213.
[80] Müller, M.; Harcey, G.; Prins, R. *Microp. Mesop. Mater.* **2000**, *34*, 281.
[81] Vitale, G.; Bull, L. M.; Morris, R. E.; Cheetam, A. K.; Toby, B. H.; Coe, C. G.; MacDougall, J. E. *J. Phys. Chem.* **1995**, *99*, 16087.
[82] Guliants, V. V.; Mullhaupt, J. T.; Newsam, J. M.; Gorman, A. M.; Freeman, C. M. *Catal. Today* **1999**, *50*, 661.
[83] Bozell, J. J.; Hegedus, L. S. *J. Org. Chem.* **1981,** 46, 2561.
[84] Larock, R. C.; Leong, W. W. in Trost; B. M.; Flemming, I. *Compr. Org. Chem.* **1991,** 4, 1.
[85] Borade, R. B.; Clearfield, A. *J. Phys. Chem.* **1992**, *96*, 6729.
[86] Barth, J. O. *Diploma thesis*, **2000,** TU München, Garching.
[87] Gaab, S. *Diploma thesis*, **2000,** TU München, Garching.
[88] Brandmair, M. *Diploma thesis*, **2000,** TU München, Garching.
[89] Jansen, C. J.; Creyghton, Njo, S. L. van Koningsveld, H.; van Bekkum, H. *Catal. Tod* **1997**, 38, 205.
[90] Haouas, M.; Kogelbauer, A.; Prins, R. *Cat. Lett.* **2000**, 70, 61.
[91] Kinger, G.; Lugstein, A.; Swagera, R.; Ebel, M; Jentys, A.; Vinek, H. *Microp. Mesop. Mater.* **2000**, 39, 307.
[92] Zholobenko, V. L.; Makarove, M. A.; Dwyer, J. *J. Phys. Chem.* **1993**, 97, 5962.
[93] Bordiga, S.; Lamberti, C.; Geobaldo, F.; Zecchina, A.; Palomino, G. T.; Krijnen, S.; van Santen, R. A. *Langmuir* **1996**, 11, 527.
[94] Lercher, J. A.; Gründling, C. H.; Eder-Mirth, G.; *Cat. Today* **1996**, 27, 353.
[95] Lugstein, A.; Jentys, A.; Vinek, H.; *Appl. Cat. A* **1999**, 176, 119.
[96] Beyer, Walter; *Lehrbuch der Organischen Chemie,* **1988**, S. Hirzel Verlag Stuttgart.
[97] Kuehl, G. H.; Timken, H., K. C. *Microp. Mesop. Mater.* **2000**, 35-36, 521.
[98] T. E. Müller and A.-K. Pleier *J. Chem. Soc., Dalton Trans.*, **1999**, 583.
[99] Kuijpers, E. G. M.; Breedijk, A. K.; Van der Wal, W. J. J. and Geus, J. W. *J. Catal.*, **1981,** 72, 210.
[100] Cheetham, A. K.; Eddy, M. M.; Thomas, J. M *J. Chem. Soc., Chem Commun.* **1984**, 1337.
[101] Corma, A.; Palomares, A.; Márquez, F. *J. Catal.* **1997**, 170, 132.
[102] Wichterlová, B.; Dedecek, J.; Vondrová, A. *J. Phys. Chem.* **1995**, 99, 1065.

[103] Sárkány, J.; d'Itri, J.; Sachtler, W. M., H. *Catal. Lett.* **1992**, 16, 241.

[104] Kunzl, V.; *Collect. Czech. Chem. Commun.* **1932,** 4, 213.

[105] Huheey, J.; Keiter, E.; Keiter, R.; *Anorganic Chemistry* **1995,** de Gruyter, New York, 2, 400.

[106] Penzien, J; Müller, T. E.; Lercher, J. A. *J. Am. Chem. Soc.* **2002**, manuscript in preparation.

[107] Van Nhu, N.; Müller, T. E.; Lercher, J. A.**,** *AIChE Journal***,** accepted.

[108] for details see R. Q. Su, T. E. Müller, *Topics in Catal.*, **2001**, submitted.

[109] An approximate first order kinetics had been reported before for the cyclization of 6AHI with $[Cu(CH_3CN)_4]PF_6$ [153]. In the study, no intermediate species was observed and the decrease in the concentration of 6AHI was mirrored by a corresponding increase in the concentration of 2MDP. As the reaction was followed *ex situ* by gas chromatography, any enamine present in the reaction mixture was probably converted to 2MDP at the high temperatures in the injector of the gas chromatograph.

[110] D. H. McDaniel, C. R. Smoot , *J. Phys. Chem.,* **1956**, *60*, 966.

[111] K. A. Connors, Chemical Kinetics – The Study of Reaction Rates in Solution, VCH, **1990**, 87.

[112] J. H. Espenson, Chemical Kinetics and Reaction Mechanisms, 2 ed., Mc Graw-Hill Inc., **1995**, *4.3*, p. 77 and 86.

[113] see N. Y. Chen, T. F. Degnan, C. M. Smith, *Molecular Transport and Reaction in Zeolites*, VCH Publishers Inc., New York, **1994**.

[114] Crabtree, R. H.; Hlatky, G. G. *Inorg. Chem.* **1980**, 19, 572.

[115] Macgregor, S. A. *Organometallics,* **2001,** 20, 9, 1860.

[116] Roundhill, D., M. *Chem. Rev. (Washington D.C.)* **1992**, 92, 1.

[117] Steinborn, D.; Taube, R. Z. *Chem.* **1986**, 26, 349.

[118] Johnston, P.; Wells, P. B.; *Radiat. Phys. Chem.* **1995**, 45, 3, 393.

[119] Horsley, J. A. *J. Phys. Chem.* **1982**, 1451.

[120] Jentys, A; unpublished results.

[121] Kau, L., S.; Spira-Solomon, D., J.; Penner-Hahn, J. E.; Hodgson, K., O.; Solomon, E., I *J. Am. Chem. Soc.* **1987**, 109, 6433.

[122] Rao, B. J.; Chetal, A. R. *J. Phys. Chem.* **1982,** 15, 6281.

[123] Smith, T. A.; Berding, M.; Penner-Hahn, J. E.; Doniach, S.; Hodgson, K. O. *J. Am. Chem Soc* **1985**, 107, 5945.

[124] Barbosa, L. A. M. M.; van Santen, R. A. *J. Am. Chem. Soc.* **2001**, 123, 4530.

[125] Elschenbroich,Ch.; Salzer, A. *Organometallchemie* **1990**, third edition, Teubner Studienbücher, Stuttgart.

[126] Konigsberger, D. C.; Prins, R. *X-Ray Absorption: Principles, Applications and Techniques in EXAFS, SEXAFS and XANES* **1988**, Willey, New York.

[127] Ankudinov, A. L.; Ravel, B.; Rehr, J. J.; Conradson, S. D. *Phys. Rev. B.* **2000**, *62*, 2437. Software version: (Version 8.10).

[128] Srivastava, P.; Baberschke, K. *Topics in Catalysis* **2000**, 10, 199.

[129] Collman, J. P.; Hegedus, L. S.; Norton, J. R.; Fink, R. G. *Principles an Applications of Organotransition Metal Chemistry,* **1987**, University Science Book; Mill Valley.

[130] Barbosa, L. A. M. M.; van Santen, R. A. *J. Am. Chem. Soc.*. **2001**, 123, 4530.

[131] T. E. Müller, M. Berger, M. Grosche, E. Herdtweck, F. P. Schmidtchen, *Organometallics*, **2001**, 20(21),4384.

[132] M. Beller, H. Trauthwein, M. Eichberger, C. Breindl, T. E. Müller, Europ. J. Inorg. Chem. (1999) 1121.

[133] M. Beller, H. Trauthwein, M. Eichberger, C. Breindl, J. Herwig, T. E. Müller, O. R. Thiel, *Chem. Eur. J. 5* (1999) 1306.

[134] Su, R. Q.; Penzien, J; Müller, T. E. *J. Mol. Chem.* **2002**, accepted.

[135] B. Akermark, J.-E. Bäckvall, K. Zetterberg, Acta Chem. Scand. B 36 (1982) 577.

[136] J. Ambüehl, P. S. Pregosin, L. M. Venanzi, G. Ughetto, L. Zambonelli, Angew. Chem. Int. Ed. Engl. 44 (1975) 369.

[137] Senn, H. M.; Blöchl, P.E.; Togni, A. *J. Am Chem. Soc.* **2000,** 122, 17, 4101.

[138] Hartung, C. G.; Tillack, A.; Trauthwein, H.; Beller, M. *J. Org. Chem.* **2001,** 66, 6339.

[139] Fleming, I.; *Frontier Orbitals and Organic Chemical Reactions*, John Wiley & Sons, Chichester, **1976**, p. 99.

[140] H. M. Senn, P. E. Blöchl, A. Togni, *J. Am. Chem. Soc.*, **2000**, *122*, 4098.

[141] Hahn, C.; Morvillo, P.; Vitagliano, A. *Eur. J. Inorg. Chem.* **2001,** 419.

[142] Lu, S.-P.; Lewin, A. H.; *Tetrahedron*, **1998**, *54*, 15097.

[143] Stanforth, S. P. *Tetrahedron*, **2001**, *57*, 1833.

[144] Caccamese, S.; Principato, G. *Tetrahedron Asym*., **1998**, *9*, 2939.

[145] Ahlbrecht, H.; Fischer, S. *Tetrahedron*, **1973**, *29*, 659.

[146] Bortnosvsky, O.; Sobalík, Z.; Wichterlová, B.; *Microp. Mesop. Mater*. **2001**, 46, 265.

[147] for details see R. Q. Su, T. E. Müller, *Tetrahedron*, **2001**, *57*, 9431.

[148] Franke, M.E.; Simon, U. *S. S. I.,* **1999**, 118, 311.

[149] B. Delley, *J. Chem. Phys.* **1990,** 92, 508.

[150] Barbosa, L. A. M. M.; van Santen, R. A. *J. Am. Chem. Soc.* **2001**, *123*, 4530.

[151] N. Van Nhu, A. Wanner, H. Tiltscher, J. A. Lercher, *Catalysis today*, **2001**, *66*, 335.

[152] OPUS, 1997-2000, Bruker Optik GmbH, Version 3.1, 9. November **2000**.

[153] T. E. Müller, M. Grosche, E. Herdtweck, A.-K. Pleier, E. Walter, Y.-K. Yan, *Organometallics*, **2000**, *19*, 170.

[154] J. V. Arena, T. M. Leu, *J. Chem. Educ.*, **1999**, 76, 867.

[155] H. E. Gottlieb, v. Kotlyar, A. Nudelman *J. Org. Chem, **1997,*** 62, 7512.

[156] T.E. Müller; Grosche, M.; Herdtweck, E.; Pleier, A.-K.; Walter, E.; Yan Y.-K.; *Organometallics,* **2000,** 19, 170.

[157] Ressler, T.; *J. Synch. Rad.* **1998,** 5, 118.

[158] Ankudinov, A. L.; Ravel, B.; Rehr, J. J.; Conradson, S. D. *Phys. Rev. B.* **2000,** 62, 2437.

# IX Appendix

**Table** Conditions of ion exchange used.

| Sample | $M_nX_m$ | Conc. (mol/l) | Solution/zeolite (ml/g) | Number of exchanges | Total time of exchange (h) | Calcination method |
|---|---|---|---|---|---|---|
| H-BEA | - | - | - | - | - | - |
| Zn/H-BEA | $Zn(CH_3CO_2)_2$ | 0.01 | 5 | 1 | 93 | A |
| Zn/H-BEA | $Zn(CH_3CO_2)_2$ | 0.02 | 5 | 1 | 14 | A |
| Zn/H-BEA | $Zn(CH_3CO_2)_2$ | 0.03 | 5 | 1 | 14 | A |
| Zn/H-BEA | $Zn(CH_3CO_2)_2$ | 0.06 | 5 | 1 | 45 | B |
| Zn/H-BEA | $Zn(CH_3CO_2)_2$ | 0.06 | 5 | 2 | 69 | B |
| Zn/H-BEA | $Zn(CH_3CO_2)_2$ | 0.06 | 5 | 3 | 163 | B |
| Zn/H-BEA | $Zn(CH_3CO_2)_2$ | 0.06 | 5 | 4 | 189 | B |
| Zn/H-BEA | $Zn(CH_3CO_2)_2$ | 0.38 | 5 | 4 | 131 | B |
| Zn/H-BEA | $Zn(CH_3CO_2)_2$ | 0.55 | 7 | 4 | 96 | A |
| Zn/H-Mor | $Zn(CH_3CO_2)_2$ | 0.04 | 34 | 4 | 48 | C |
| Zn/H-MCM-22 | $Zn(CH_3CO_2)_2$ | 0.02 | 46 | 4 | 47 | C |
| Zn/H-Y | $Zn(CH_3CO_2)_2$ | 0.18 | 20 | 4 | 96 | D |
| Zn-$SiO_2$ | $Zn(CH_3CO_2)_2$ | 0.04 | 20 | F | - | E |
| Cu(I)/H-BEA | $[Cu(CH_3CN)_4]PF_6$ | 0.09 | 14.3[b] | 4 | 167 | - |
| Cu(II)/H-BEA | $Cu(CH_3CO_2)_2$ | 0.01 | 70 | 1 | 12 | A |
| Cu(II)/H-BEA | $Cu(CH_3CO_2)_2$ | 0.02 | 70 | 1 | 12 | A |
| Rh(I)/H-BEA | $[Rh(NOR)_2]ClO_4$ | 0.01 | 13[b] | 1 | 60 | - |
| Pd/H-BEA | $PdCl_2$ | 0.06 | 5 | 3 | 63 | A |
| Pt/H-BEA | $[Pt(NH_3)_4](OH)_2$ | 0.004 | 83 | F | 12 | A |
| Ni/H-BEA | $Ni(CH_3CO_2)_2$ | 0.03 | 30 | 4 | 14 | A |
| La/H-BEA | $LaCl_3 \times 7\ H_2O$ | 0.35[a] | - | - | - | - |

Calcination method
A: RT-120°C 0.5°C/min; 120°C 3 h; 120-500°C 1°C/min; 500°C 2 h
B: RT-500°C, 5°C/min; 500°C, 5 h
C: RT-500°C, 10°C/min; 500°C, 1 h
D: RT-120°C, 5°C/min; 120°C, 1 h; 120-450°C, 5°C/min; 450°C, 1 h
E: RT-550°C, 10°C/min; 550°C, 5 h
F. wet impregnation

[a] in mmol/g zeolite
[b] Solvent $CH_3CN$

**Table 2** Chemical composition and surface areas determined by AAS and BET.

| Sample | $M^{n+}$ contents (mmol/g) | $M^{n+}$/Al | Al contents (mmol/g) | Si/Al | $M^{n+}$ per unit cell | BET-Surface Area ($m^2$/g) | Micropore Surface Area ($m^2$/g) | Meso/Macro-pore Area ($m^2$/g) |
|---|---|---|---|---|---|---|---|---|
| H-BEA | - | - | 1.36 | 11.6 | - | 536.5 | 137.8 | 398.8 |
| Zn/H-BEA | 0.03 | 0.02 | 1.37 | 11.4 | 0.1 | 526.9 | 200.8 | 326.1 |
| Zn/H-BEA | 0.06 | 0.04 | 1.27 | 12.6 | 0.2 | 545.3 | 108.4 | 436.9 |
| Zn/H-BEA | 0.11 | 0.08 | 1.47 | 10.7 | 0.4 | 509.9 | 141.3 | 368.7 |
| Zn/H-BEA | 0.20 | 0.15 | 1.37 | 11.3 | 0.8 | 518.1 | 147.6 | 370.5 |
| Zn/H-BEA | 0.31 | 0.26 | 1.18 | 13.4 | 1.2 | 526.2 | 148.5 | 377.7 |
| Zn/H-BEA | 0.49 | 0.40 | 1.21 | 12.7 | 1.9 | 493.9 | - | - |
| Zn/H-BEA | 0.54 | 0.46 | 1.18 | 12.7 | 2.2 | 549.4 | 129.2 | 420.2 |
| Zn/H-BEA | 0.66 | 0.53 | 1.24 | 12.0 | 2.6 | 460.1 | 96.4 | 363.7 |
| Zn/H-BEA | 0.86 | 0.77 | 1.12 | 12.1 | 3.8 | 516.9 | 151.0 | 365.9 |
| Zn/H-Mor | 0.61 | 0.23 | 1.82 | 9.1 | 1.7 | 311.0 | 223.5 | 87.5 |
| Zn/H-MCM-22 | 0.42 | 0.35 | 1.61 | 7.8 | 1.9 | 194.1 | 83.3 | 110.8 |
| Zn/H-Y | 1.62 | 0.41 | 3.99 | 2.2 | 24 | 596.2 | 334.9 | 261.2 |
| Zn-$SiO_2$ | 0.73 | - | - | - | - | 181.1 | - | - |
| Cu(I)/H-BEA | 0.47 | 0.61 | 0.76 | 20 | 1.9 | - | - | - |
| Cu(II)/H-BEA | 0.45 | 0.38 | 1.18 | 12.5[a] | 1.9 | - | - | - |
| Cu(II)/H-BEA | 0.67 | 0.60 | 1.12 | 12.5[a] | 3.2 | - | - | - |
| Rh/H-BEA | 0.15 | 0.12 | 1.26 | 12.5[a] | 0.6 | - | - | - |
| Pd/H-BEA | 0.40 | 0.32 | 1.26 | 12.5 [a] | 1.5 | - | - | - |
| Pt/H-BEA | 0.29 | 0.23 | 1.26 | 12.5 [a] | 1.1 | - | - | - |
| Ni/H-BEA | 0.88 | 0.78 | 0.76 | 13.60 | 3.4 | - | - | - |
| La/H-BEA | 0.27 | 0.21 | 1.26 | 12.5 [a] | 1.0 | - | - | - |
| ZnO | 15.29 | - | - | - | - | 6.50 | - | - |

[a] As specified by producer

**Table 3.1** GC analysis; Temperature program: 120°C 5 min, 120 – 250°C 5°C/min, 250°C 5 min

| Substance | $R_F$ value[a] |
|---|---|
| Phenylacetylene | 1.476 |
| Aniline | 2.153 |
| Acetophenone | 2.901 |
| N-(methyl-benzylidene)-aniline | 8.241 |

[a] Ratio retention time component / retention time toluene

**Table 3.2** GC analysis; Temperature program: 120 – 160°C 1°C/min, 160°C 3 min

| Substance | $R_F$ value |
|---|---|
| 6AHI | 1.214 |
| 2-methyl-1,2-dihydropiperidine | 1.264 |

**Table 3.3** GC analysis; Temperature program: 41 °C 2 min 41 – 200°C 25°C/min, 200°C 2 min

| Substance | $R_F$ value |
|---|---|
| 3-aminopropylvinyether | 1.088 |
| N,O-acetal tetrahydro-2-methyl-1,3-oxazine | 1.055 |

**Table 4:** Reaction conditions employed in the *in situ* NIR experiments described in this study.

| Catalyst | | | 6AHI | | Solvent | | Temp. |
|---|---|---|---|---|---|---|---|
| | [mg] | [µmol] | [µl] | [mmol] | | [$cm^3$] | [°C] |
| $Zn(CF_3SO_3)_2$ | 14.9 | 41 | 458 | 4.10 | Toluene | 70 | 82 |
| $Zn(CF_3SO_3)_2$ | 9.2 | 25 | 282 | 2.52 | Toluene | 60 | 111 |
| $Zn(CF_3SO_3)_2$ (a) | 11.3 | 31 | 349 | 3.11 | Toluene | 66 | 111 |
| $Zn(CF_3SO_3)_2$ | 12.5 | 34 | 383 | 3.43 | Toluene | 70 | 125 |
| Zn-BEA | 65.5 | 32 | 359 | 3.21 | Toluene | 60 | 82 |
| Zn-BEA | 55.6 | 27 | 305 | 2.72 | Toluene | 60 | 95 |
| Zn-BEA | 56.0 | 27 | 307 | 2.74 | Toluene | 70 | 111 |
| Zn-BEA | 58.3 | 29 | 320 | 2.85 | Toluene | 65 | 125 |

(a) 55 µl, $0.62 \times 10^{-3}$ mol $CF_3SO_3H$ added as co-catalyst to the reaction mix

**Table 5:** Reaction conditions employed in the *in situ* EXAFS experiments described in this study.

| Catalyst / reference material | Amount (mmol) | Reactand | Amount (mmol) | Ratio s/c | Solvent | (cm$^3$) | Edge energy (eV) |
|---|---|---|---|---|---|---|---|
| $[Cu(CH_3CN)_4]PF_6$ | 0.07 | - | - | - | $CH_3CN$ | 1.50 | 8980.81 |
| $[Cu(CH_3CN)_4]PF_6$ | 0.07 | 6AHI | 0.75 | 10.3 | $CH_3CN$ | 1.41 | 8980.65 |
| Cu(I)/H-BEA (0.61 Cu/Al) | 0.03 | - | - | - | $CH_3CN$ | 1.00 | 8980.89 |
| Cu(I)/H-BEA (0.61 Cu/Al) | 0.03 | 6AHI | 0.18 | 5.5 | $CH_3CN$ | 0.98 | 8981.09 |
| Cu-foil | - | - | - | - | - | - | 8977.00 |
| $Cu_2O$ | 0.34 | - | - | - | - | - | 8980.85 |
| CuO | 0.39 | - | - | - | - | - | 8984.25 |
| $[Cu(CH_3CN)_4]PF_6$ | 0.26 | - | - | - | PE[a] | - | 8980.88 |
| Cu(I)/H-BEA (0.61 Cu/Al) | 73.6 | - | - | - | - | - | 8980.59 |
| $Zn(CF_3SO_3)_2$ | 0.08 | - | - | - | $CH_3CN$ | 1.76 | 9662.68 |
| $Zn(CF_3SO_3)_2$ | 0.08 | 6AHI | 0.81 | 9.6 | $CH_3CN$ | 1.67 | 9662.17 |
| Zn/H-BEA (0.53 Zn/Al) | 0.07 | - | - | - | $CH_3CN$ | 1.14 | 9662.88 |
| Zn/H-BEA (0.53 Zn/Al) | 0.07 | 6AHI | 0.72 | 10.8 | $CH_3CN$ | 1.05 | 9662.88 |
| Zn/H-BEA (0.08 Zn/Al) | 0.03 | - | - | - | $CH_3CN$ | 0.71 | 9663.98 |
| Zn/H-BEA (0.08 Zn/Al) | 0.03 | 6AHI | 0.33 | 12.6 | $CH_3CN$ | 0.67 | 9662.64 |
| Zn-foil | - | - | - | - | - | - | 9659.00 |
| ZnO | 0.32 | - | - | - | PE | - | 9661.82 |
| Zn/H-BEA (0.08 Zn/Al) | 0.17 | - | - | - | - | - | 9663.00 |
| Zn/H-BEA (0.53 Zn/Al) | 0.12 | - | - | - | - | - | 9663.05 |
| $Zn(CF_3SO_3)_2$ | 0.24 | - | - | - | PE | - | 9663.86 |
| $[Pd(Triphos)](CF_3SO_3)_2$ | 0.21 | - | - | - | $CH_3CN$ | 6.11 | 24359.97 |
| $[Pd(Triphos)](CF_3SO_3)_2$ | 0.21 | 6AHI | 2.57 | 12.1 | $CH_3CN$ | 5.79 | 24360.20 |
| Pd/H-BEA (0.32 Pd/Al) | 0.17 | - | - | - | $CH_3CN$ | 3.92 | 24362.53 |
| Pd/H-BEA (0.32 Pd/Al) | 0.17 | 6AHI | 1.63 | 9.7 | $CH_3CN$ | 3.72 | 24362.36 |
| Pd-foil | - | - | - | - | - | - | 24350.00 |
| PdO | - | - | - | - | - | - | 24362.17 |
| Pd/H-BEA (0.32 Pd/Al) | 0.16 | - | - | - | - | - | 24362.22 |
| $[Pd(Triphos)](CF_3SO_3)_2$ | 0.21 | - | - | - | PE | - | 24364.39 |

(a) PE = Polyethylene